

ABSTRACT

LI, XIAOFU. Dynamics of Adaptive Oscillators. (Under the direction of Dr. Edmon Perkins).

Whereas linear oscillators have static natural frequencies, adaptive oscillators are a type of nonlinear oscillator that can both *learn and store information* in its plastic states. For instance, adaptive frequency oscillators are a subset of adaptive oscillators, which contain a single plastic state that enables it to learn and store a frequency component from an external force.

This dissertation explores several adaptive oscillators from their dynamical perspective, including numerical simulations of their response, analysis of their dynamics with and without noise, and physical experiments. The contributions covered in this dissertation include: 1) Numerical simulations, a Floquet analysis, and an analog circuit experiment studying a four-state adaptive oscillator, 2) The stochastic dynamical response of a three-state adaptive frequency Hopf oscillator, 3) A physical realization of pendulum adaptive frequency oscillator, 4) A demonstration of chaotic behavior in the adaptive frequency pendulum oscillator proposed in (3), via numerical simulations and experimental approaches, and 5) An analog realization of an adaptive oscillator as a musical instrument.

Adaptive oscillators have been relatively under-explored in the literature. In this dissertation, new physical architectures of adaptive oscillators are discussed, such as a four-state adaptive oscillator and a pendulum adaptive frequency oscillator. A comprehensive study of the effects of noise on the Hopf adaptive frequency oscillator, showing that the adaptation works correctly for small amplitudes of noise but does not work for large amplitudes of noise. Preliminary results for new applications of adaptive oscillators, such as energy harvesting and musical applications, are also shown. Adaptive oscillators have very complex, nonlinear behavior, which can be used advantageously to adapt to external stimuli,

but they can also have chaotic responses. By gaining a better understanding of adaptive oscillators, they could be used for many real-world, smart structures.

© Copyright 2022 by XiaoFu Li

All Rights Reserved

Dynamics of Adaptive Oscillators

by
XiaoFu Li

A dissertation submitted to the Graduate Faculty of
North Carolina State University
in partial fulfillment of the
requirements for the Degree of
Doctor of Philosophy

Mechanical Engineering

Raleigh, North Carolina
2022

APPROVED BY:

Dr. Larry Silverberg

Dr. Laura Bottomley

Dr. Fen Wu

Dr. Robert Dean

Dr. Edmon Perkins
Chair of Advisory Committee

ACKNOWLEDGMENTS

The guidance and patience of my advisor, Dr. Edmon Perkins, is most appreciated. Many thanks are also given to my labmates for their thoughtful, useful, and candid advice. My thanks, as well, to my dissertation defense committee for their time, patience, and comments. Partial support for this research from DARPA (Grant Number **W911NF-20-1-0336**) and the Office of Naval Research (Grant Number **N00014-19-1-2413**) is greatly appreciated.

TABLE OF CONTENTS

List of Tables	v
List of Figures	vi
Chapter 1 INTRODUCTION	1
1.1 Problem of Interest & Objectives	1
1.2 Literature Review	3
1.3 Outline	9
Chapter 2 A four state adaptive hopf oscillator	13
2.1 Two-state System	14
2.2 Three-state System	14
2.3 Four-state System	16
2.4 Local Analysis	16
2.5 Experimental Results	18
2.5.1 Circuit Design	18
2.5.2 Range of Operation	20
2.5.3 Verification of Other Waveforms	23
2.6 Conclusion	25
Chapter 3 Stochastic Effects on a Hopf Adaptive Frequency Oscillator	29
3.1 Equations for a Hopf Adaptive Frequency Oscillator	30
3.2 Euler-Maruyama Simulations	31
3.3 Fokker-Planck Equation and Moment Equations	34
3.4 Analog Circuit Experiment	41
3.5 Concluding remarks	47
Chapter 4 The Pendulum Adaptive Frequency Oscillator	49
4.1 Equations of Motion	50
4.2 Numerical Results	52
4.3 Experimental Setup	55
4.3.1 Linear Natural Frequency Approximation	57
4.3.2 Method of Multiple Scales	59
4.3.3 Experimental Parameters	62
4.3.4 Experimental Implementation of Frequency Adaptation	65
4.4 Experimental Results	66
4.5 Conclusions	68
Chapter 5 Chaos in a Pendulum Adaptive Frequency Oscillator	69
5.1 Equation of Motion of Horizontally Forced Pendulum AFO	70

5.2	Simulation Results	72
5.3	Field-Programmable Analog Array Circuit	76
5.4	Experimental Results	78
5.5	Conclusions	79
Chapter 6	A Hopf Adaptive Oscillator Analog Circuit as a Musical Instrument . .	83
6.1	Circuit Implementation	84
6.2	Musical Process	87
6.3	Example: <i>Ave Maria</i>	89
6.4	Conclusion	92
Chapter 7	Conclusions & Future Work	93
7.1	Summary of Results	93
7.2	Future Work	94
References	96

LIST OF TABLES

Table 3.1	List of moments and their respective moment equation.	40
Table 4.1	Parameters for the experiment, which are directly measured.	58
Table 4.2	Curve fit results when $l_1 = 16.5$ cm.	64
Table 5.1	List of parameters and states.	70

LIST OF FIGURES

Figure 2.1	Comparison of original and modified AFOs. For two forcing frequencies, a comparison of the original AFO as proposed by [1] and the simplified system, as given in Eq. 2.2, is shown.	15
Figure 2.2	Printed circuit board. PCB used in experiments. Here, “Ext. Sig.” is given by $V_p(t)$	19
Figure 2.3	Simplified circuit schematic. A simplified schematic for the four-state adaptive system, with states V_x , V_y , V_ω , and V_a	19
Figure 2.4	Time history of the four-state oscillator. Experimental data is plotted as a black solid line, SPICE simulation data is plotted as a blue dashed line, and the sinusoid’s Ω and a are plotted as dotted lines.	21
Figure 2.5	Range of Operation. Comparison of results of PCB experiment and SPICE simulations, with $k = 0.5$, $a = 1.5$ (except (d)), $\omega_0 \approx 15.9$ Hz, and $\mu = 1$ for both the simulations and the experiments. It should be noted that the frequency-amplitude relationship is reported for the x -state, while the percent error is reported for the ω -state. Noting that for the four-state system (bottom-right), the oscillator learns the correct amplitude from approximately 0 to 3; after 3, nonlinear effects in the PCB cause the simulation and experimental results to diverge.	22
Figure 2.6	Square wave results. A generated square wave with a varying fundamental frequency was used as the input to the adaptive oscillator circuit. The circuit was able to learn the fundamental frequency of the square wave. Top: The time history of the x state and the generated square wave are shown. Bottom: The circuit learns the fundamental frequency of the square wave, even though the frequency was varying over time.	24
Figure 2.7	Sawtooth wave results. A generated sawtooth wave was used as the input to the adaptive oscillator circuit. The circuit was able to learn the fundamental frequency of the sawtooth wave. Top: The time history of the x state and the generated sawtooth wave are shown. Bottom: The circuit learns the fundamental frequency of the sawtooth wave.	25
Figure 2.8	Impact test results. Strain gauge data [2] was directly input to the adaptive oscillator circuit. The circuit learned the natural frequency of the nonlinear beam. Top-left: The time history of the strain gauge’s voltage is shown. The impact of the beam happens at approximately 3 seconds. Bottom-left: The circuit learns the first natural frequency of the beam. Right: An FFT of the beam is shown, with the first natural frequency marked by a dashed, vertical line.	26

Figure 2.9	Asphaltophone results. A filtered audio recording of an asphaltophone was input to the adaptive oscillator circuit. Top: The original signal and the filtered signal are plotted. Bottom: The circuit learns the F3 note from the asphaltophone. The data is still quite noisy, so the ω state has fluctuations about the F3 frequency.	27
Figure 2.10	Robotic player trumpet results. A scaled recording of a robotic player trumpet was input to the adaptive oscillator circuit. The circuit learned the natural frequency of the trumpet's note. Top-left: The time history of the trumpet recording is shown. The time was rescaled by a factor of four. Bottom-left: The circuit learns the first natural frequency of the note. Right: An FFT of the note is shown, with the first natural frequency marked by a dashed, vertical line. . .	28
Figure 3.1	Euler-Maruyama simulations: x state. Mean and variance of x obtained from 500 ensemble averages of Euler-Maruyama simulations. As the noise amplitude is increased, $\langle x \rangle$ decreases.	31
Figure 3.2	Euler-Maruyama simulations: y state. Mean and variance of y obtained from 500 ensemble averages of Euler-Maruyama simulations. As the noise amplitude is increased, $\langle y \rangle$ decreases.	32
Figure 3.3	Euler-Maruyama simulations: ω state. Mean and variance of ω obtained from 500 ensemble averages of Euler-Maruyama simulations. For small amount of noise, $\langle \omega \rangle$ quickly approaches Ω without overshoot error. As the noise amplitude is increased, the $\langle \omega \rangle$ value converges to the incorrect value.	32
Figure 3.4	Euler-Maruyama simulations: limit cycles. For the Euler-Maruyama simulations, the limit cycle of $\langle x \rangle$ vs. $\langle y \rangle$ is shown. As the noise level increases, the two dimensional limit cycle begins to collapse into one dimensional oscillations when considering the averaged dynamics. .	33
Figure 3.5	Fokker-Planck results: x state. Mean and variance of x obtained from moment equations. As the noise amplitude is increased, $\langle x \rangle$ decreases.	35
Figure 3.6	Fokker-Planck results: y state. Mean and variance of y obtained from moment equations. As the noise amplitude is increased, $\langle y \rangle$ decreases, eventually collapsing the limit cycle into one dimensional oscillations.	36
Figure 3.7	Fokker-Planck results: ω state. Mean and variance of ω obtained from moment equations. As the noise amplitude is increased, the $\langle \omega \rangle$ value converges to the incorrect value.	36
Figure 3.8	Fokker-Planck results: limit cycles. For the moment equations, the limit cycle of $\langle x \rangle$ vs. $\langle y \rangle$ is shown. As the noise level increases, the two dimensional limit cycle begins to collapse into one dimensional oscillations.	37

Figure 3.9	Circuit experiment. The printed circuit board that was used for the experiments. Here, $f(t) = a \sin(\Omega t) + \sigma \dot{W}(t)$	41
Figure 3.10	Circuit schematic. A simplified schematic for the Hopf AFO circuit, with states V_x , V_y , and V_ω	42
Figure 3.11	Experimental results: x state. Mean and variance of x obtained from the experiments. As the noise amplitude is increased, $\langle x \rangle$ decreases.	43
Figure 3.12	Experimental results: y state. Mean and variance of y obtained from the experiments. As the noise amplitude is increased, $\langle y \rangle$ decreases.	43
Figure 3.13	Experimental results: ω state. Mean and variance of ω obtained from the experiments. It should be noted that V_ω was converted to ω to compare the results to the forcing frequency, Ω . As the noise amplitude is increased, $\langle \omega \rangle$ converges to the incorrect value.	44
Figure 3.14	Experimental results: limit cycles. For the experiment, the limit cycle of $\langle x \rangle$ vs. $\langle y \rangle$ is shown. As the noise level increases, the two dimensional limit cycle begins to collapse into one dimensional oscillations.	44
Figure 3.15	Unaveraged results. For several noise amplitudes, the single-sided amplitude spectrum of the unaveraged x state is shown. Without averaging, it can be seen that the signal content is attenuated, which is a nonlinear effect. The signal-to-noise ratio decreases for larger amplitudes of noise because of both the addition of noise and the attenuation of signal present in the x state.	46
Figure 4.1	Pendulum with horizontal forcing. It should be noted that the cart is kinematically constrained to the forcing function, $f(t)$	50
Figure 4.2	Numerical results of pendulum adaptive frequency oscillator for small oscillations. For small oscillations, the pendulum acts as a linear oscillator. Left: The frequency response of the pendulum adaptive frequency oscillator is compared with the frequency response of the non-adaptive pendulum, for several values of ω_n . For this simulation, $c = 0.45$ and $A = 0.552$. Notice that the pendulum adaptive oscillator has the same amplitude as the non-adaptive pendulum only when the non-adaptive pendulum's amplitude is at a maximum. Right: The ω state learns the external forcing with high accuracy. . .	53

Figure 4.3	<p>Numerical results of pendulum adaptive frequency oscillator for large oscillations. For large oscillations, the pendulum acts as a softening Duffing oscillator. Left: The frequency response of the pendulum adaptive frequency oscillator is compared with the frequency response of the non-adaptive pendulum, for several values of ω_n. For this simulation, $c = 0.45$ and $A = 5.52$, which can be compared with Fig. 4.9. Notice that the pendulum adaptive oscillator has the same amplitude as the non-adaptive pendulum only when the non-adaptive pendulum's amplitude is at a maximum. Right: The ω state has an offset above the external forcing frequency. This is caused by the hysteresis in the frequency amplitude response, as will be discussed in Subsection 4.3.2.</p>	54
Figure 4.4	<p>Experimental pendulum adaptive frequency oscillator. The experimental pendulum adaptive frequency oscillator prototype. a) Side view: The balanced mass offsets the mass of the stepper motor. The masses and lengths can be compared to those labeled in the drawing, which is depicted in Fig. 4.5. b) Top view: The white motor housing is made 3D printed using Formlabs' Rigid resin. The rotary encoder measures the angular displacement of the pendulum. The stepper motor rotates a pinion, which moves the rack, modifies the pendulum's rod length. The rigid rod is connected to the cart.</p>	56
Figure 4.5	<p>Schematic for the experimental pendulum adaptive frequency oscillator prototype. This pendulum setup, similar to a metronome, allows a smaller amount of mass, $m_{rack} + m_4$, to be actuated with the stepper motor. The system rotates about the black dot. m_1 is the mass of an unmovable weight, which is offset by an amount l_{m1} from the rotation point. m_2 is the mass of the lower portion of the rack, which has a length of l_1. m_3 is the mass of the upper portion of the rack, which has a length of l_2. m_4 is the mass at the top of the rack. This pendulum setup, similar to a metronome, allows a smaller mass, m_4 to be actuated with the stepper motor.</p>	57
Figure 4.6	<p>Duffing-like response of pendulum. For a non-adaptive pendulum with rod length set to $l_1 = 16.5$ cm, a frequency up-sweep and down-sweep was performed with the experiment; the green markers are the prototype's amplitude response. This data was then used in a curve fit of eq. 4.29. The resulting frequency response function is plotted as a black curve. It should be noted that eq. 4.29 has multiple roots, and some frequencies have two stable amplitude responses.</p>	63

Figure 4.7	Relationship between rack length and linear natural frequency. The relationship between the lower rack length, l_1 , and the pendulum's linear natural frequency is depicted as a dashed, black curve. A portion of this range is quite linear, which is depicted as a green, solid curve.	65
Figure 4.8	The time history of the pendulum adaptive frequency oscillator. The external forcing frequency was $\Omega = 7.1$ rad/s. The amplitude of the x and y states increase when the ω state has learned the resonance frequency.	67
Figure 4.9	Experimental results of pendulum adaptive frequency oscillator for large oscillations. A forcing frequency sweep ranging from 5.5 rad/s to 8.6 rad/s was performed on the pendulum adaptive frequency oscillator prototype. The average of the ω state's steady state value is plotted for each forcing frequency, Ω . The line $\omega = \Omega$ is plotted for reference. The pendulum adaptive frequency oscillator learns the input frequency with high accuracy. Since the amplitude of the pendulum adaptive frequency oscillator is large, there is a positive offset of the ω state, as was seen in Fig. 4.3.	67
Figure 5.1	Pendulum with horizontal forcing. It should be noted that $f(t)$ kinematically moves the pivot point.	71
Figure 5.2	Periodic stroboscopic sections from numerical simulations. Stroboscopic sections of the states of the horizontally forced pendulum adaptive frequency oscillator for Ω ranging from 1.6 rad/s to 2.2 rad/s. Here, $a = 0.1$, $c = 0.35$, and $k_\omega = 0.707$. The green dashed line represents the line $\omega = \Omega$. For this combination of parameters, the pendulum adaptive frequency oscillator correctly learns the external forcing frequency.	73
Figure 5.3	Chaotic stroboscopic sections from numerical simulations. Bifurcation diagram using the stroboscopic sections of the states of the horizontally forced pendulum adaptive frequency oscillator for Ω ranging from 1.6 rad/s to 2.2 rad/s. Here, $a = 1.8$, $c = 0.35$, and $k_\omega = 0.707$. The green dashed line represents the line $\omega = \Omega$. Instead of learning the external forcing frequency, the bifurcation diagram exhibits chaotic behavior.	74
Figure 5.4	Period-3 implies chaos. For $\Omega = 2.12$ rad/s, the response of the ω state has period-3 motion. Here, $a = 1.8$, $c = 0.35$, and $k_\omega = 0.707$. On the left, the stroboscopic sections are shown for a portion of the time history. The vertical green dashed lines depict the clock's sampling rate for the stroboscope, and the * is the value of the ω state at these times. On the right, the three dimensional trajectory of the system is shown.	75

Figure 5.5	Strange attractor from simulations. For $\Omega = 1.67$, a strange attractor is shown. For this simulation, $a = 1.8$, $c = 0.35$, and $k_\omega = 0.707$	75
Figure 5.6	FPAA circuit schematic of pendulum adaptive frequency oscillator. An external forcing signal was sent to the FPAA via differential input IO3 of FPAA3.	77
Figure 5.7	Non-chaotic stroboscopic sections from experiments. Stroboscopic sections of the states of the FPAA circuit for Ω ranging from 1600 rad/s to 2200 rad/s. Note that the FPAA runs at 1000 times faster than the simulations due to the RC time constant, so the W state should be multiplied by 1000 to calculate the learned frequency. Here, $a = 0.1$, $c = 0.35$, and $k_\omega = 0.707$. The green dashed line represents the line $\frac{\omega}{1000} = \Omega$. For this combination of parameters, the FPAA correctly learns the external forcing frequency.	78
Figure 5.8	Chaotic stroboscopic sections from experiments. Bifurcation diagram using the stroboscopic sections of the states of the FPAA for Ω ranging from 1600 rad/s to 2200 rad/s. Note that the FPAA runs at 1000 times faster than the simulations due to the RC time constant, so the W state should be multiplied by 1000 to calculate the learned frequency. Here, $a = 1.8$, $c = 0.35$, and $k_\omega = 0.707$. The green dashed line represents the line $\frac{\omega}{1000} = \Omega$. Instead of learning the external forcing frequency, the bifurcation diagram exhibits chaotic behavior.	80
Figure 5.9	Strange attractor from experiments. For $\Omega = 1640$, a strange attractor is shown. For this experiment, $a = 1.8$, $c = 0.35$, and $k_\omega = 0.707$	81
Figure 5.10	Period-5 motion from experiment. For $\Omega = 1880$ rad/s, the response of the W state has period-5 motion. Here, $a = 1.8$, $c = 0.35$, and $k_\omega = 0.707$. On the left, the stroboscopic sections are shown for a portion of the time history. The vertical green dashed lines depict the clock's sampling rate for the stroboscope, and the * is the value of the W state at these times. On the right, the three dimensional trajectory of the system is shown.	81

Figure 6.1	<p>Frequency response. Aspects of the frequency learning capability of the breadboard circuit are shown here, where k_x, k_ω, and μ are equal to 1.2 V, 0.8 V, and 1 V, respectively. <u>Left</u>: The grey dashed lines denote the external forcing frequency, Ω. Three cases are shown, which are driving frequencies of 19 Hz, 450 Hz, and 600 Hz. The black solid lines depict the time evolution of the ω state. <u>Right/Top</u>: The frequency-amplitude relationship for the x state of the circuit is plotted with a black solid line. The vertical dashed lines correspond to the frequencies that fall within $\pm 1\%$ error. <u>Right/Bottom</u>: The percent error for the ω state is plotted with a black solid line. The horizontal dashed lines correspond to $\pm 1\%$ error, while the vertical dashed lines correspond to the frequencies that fall within $\pm 1\%$ error. 84</p>
Figure 6.2	<p>Circuit schematic for the Hopf adaptive frequency oscillator. This circuit has states V_x, V_y, V_ω, where TL082 operational amplifiers and AD633 multipliers are powered by a 15 V DC component. 86</p>
Figure 6.3	<p>Comparison of original vocals to response of circuit. A comparison of the original vocals, f_{vocals}, (denoted as grey dash-dotted line) and the vocals with the pedal points, $f_{vocals} + f_{pedal}$ (denoted as black solid line). The inset windows show zoomed portions for visualization purposes. The left inset shows an example when the vocals are not present; in this inset, the vocals are approximately equal to zero, while the pedal points cause small sinusoidal fluctuations. The right inset shows an example when the vocals are present. It should be noted that f_{vocals} and $f_{vocals} + f_{pedal}$ are very similar in the right inset. 88</p>
Figure 6.4	<p>A comparison of the single-sided amplitude spectrum between $f_{vocals} + f_{pedal}$ (top) and the experimental results of the y state (bottom). The pedal points have a large amplitude in the FFT because they are always present in the external forcing, $f(t)$. Both FFTs were normalized for comparison purposes. 90</p>
Figure 6.5	<p>A portion of the response of the x (solid) and y (dashed) states from the circuit. Since the x state has higher frequency components, the y state was chosen for the “voice” of the instrument. 90</p>
Figure 6.6	<p>Time response of the experimentally collected ω state. The pedal points, annotated as D_3, D_4 and D_5, are plotted as dashed black lines for comparison. One of these pedal point frequencies is learned by the circuit when the amplitude of the vocals is too small. 91</p>

CHAPTER

1

INTRODUCTION

1.1 Problem of Interest & Objectives

Whereas linear oscillators have static natural frequencies, adaptive oscillators (AOs) are a type of nonlinear oscillator that can both *learn and store information* in its plastic states. For instance, adaptive frequency oscillators (AFOs) are a subset of adaptive oscillators, which contain a single plastic state that enables it to learn and store a frequency component from an external force. Early studies of adaptive phase oscillators were used as neural models to reproduce sinusoidal inputs [3]. More generally, adaptive oscillators (AOs) can be created by adding additional, plastic states to a nonlinear oscillator [4]. The derivation of

adaptive frequency oscillators (AFOs) was originally based on a dynamic Hebbian learning rule by modifying the Hopf system [1]. The correlation-based Hebbian rule was inspired from the firing rate of neurons, such that the information transmission between different neurons will be increased due to electrical activity, which can synchronize neural networks [5]. Generally, learning characteristics of AOs can be preferable when compared with their counterparts, such as the relaxation oscillator and the phase oscillator [6, 7], which are limited to simple inputs and have smaller basins of attraction. It should be noted that AOs are similar to phase-locked loops, except AOs have an additional, direct injection of the external forcing on the oscillator itself. The most important difference is that AOs explicitly encode information in plastic states. It should be noted that adaptive oscillators are similar to reservoir computers, in that their computational ability and memory storage are not independent [8, 9, 10]

Adaptive oscillators are similar to phase-locked loops, except that they explicitly store information content in plastic states. Compared to non-adaptive oscillators, adaptive oscillators have received relatively little attention. Previously, only two circuit implementations of adaptive oscillators have been reported, both of which were Hopf AFOs: a VLSI implementation, which did not report any experimental results [11], and a field-programmable gate array (FPGA) implementation [12].

The research objectives of this dissertation are 1) to understand the role of adaptation in nonlinear systems, 2) to study the effects of noise on adaptive states, and 3) to explore the uses of adaptive oscillators in real-world applications. This work is expected to bolster research and technology in the areas of hardware signal processing, information processing, medical implants, and energy harvesting. In addition, adaptive oscillators will be explored in the context of music.

1.2 Literature Review

Early studies of adaptive phase oscillators were used as neural models to reproduce sinusoidal inputs [3]. More generally, adaptive oscillators (AOs) can be created by adding additional, plastic states to a nonlinear oscillator [4]. The derivation of adaptive frequency oscillators (AFOs) was originally based on a dynamic Hebbian learning rule implemented in hardware by modifying the Hopf system [1]. The correlation-based Hebbian rule was inspired from the firing rate of neurons, such that the information transmission between different neurons will be increased due to electrical activity, which can synchronize neural networks [5]. Generally, learning characteristics of AOs can be preferable when compared with their counterparts, such as the relaxation oscillator and the phase oscillator [6, 7], which are limited to simple inputs and have smaller basins of attraction.

Several practical applications of AOs have been explored. *Central pattern generators* (CPGs) have been used to control the motion of individual joints of walking robots [13], and adaptive frequency oscillators can work together to create an arbitrary CPG [14, 15, 16]. Various gait patterns for locomotion can be achieved through assigning specific frequency and phase angles to individual oscillators in an array. Applications for locomotion control using Field Programmable Gate Arrays (FPGAs) with the aid of CPGs and coupled nonlinear oscillators have also been proposed [17, 18, 19]. Specifically, the HAFO has been used for robotic locomotion control by employing HAFOs as CPGs to tune walking patterns in a cooperative way [20, 21, 22]. Body dynamics of these robots often vary over time due to obstacles and environmental fluctuations. These oscillators can be used as adaptive controllers that find and match intrinsic frequencies leading to enhanced energy efficiency of the resulting gait [23, 24]. Additionally, AFOs have been proposed to detect gait phase and frequency in robots for assisting people with walking difficulties due to muscle weakness [25] or reducing the metabolic cost of walking [26]. State observer AFOs have been used to create

cross adaptation between users and assistance robots resulting in reduced effort supporting arm muscles' activities [27]. An array of AOs has also been proposed as a biologically-inspired analog signal analyzer [28]. This form of analog signal analyzer subtracts the dynamic response of AOs from an input signal, which causes the array's frequency states to converge to the frequencies present in the input signal [29].

Considering these mentioned uses, an AO that is capable of learning additional states could be useful to many applications. Building on the work of chaotic oscillator circuits [30, 31], a four-state adaptive oscillator analog circuit that links theory discussed by [1] is presented. The resulting system provides the dynamics of 1) A two-state regular Hopf oscillator, 2) A three-state AO that can learn the *frequency* of an input sinusoid, and 3) A four-state AO that can learn the *frequency* and *amplitude* of an input sinusoid and extends the work of [11, 12]. These schemes are similar to AOs that have previously improved phase-locked loop designs through Lyapunov treatments [32]. In this letter, we show a topology that extends the number of adaptive states previously implemented and show direct injection of a forcing signal. This AO is similar to the phase-locked loop Lyapunov design [32]; in the Lyapunov design, the forcing frequency needed to be directly inputted into the system. In the current AO, the forcing signal is injected directly into the x , ω , and α states without knowledge of the frequency. This is an important distinction, since the forcing signal, $a \sin(\Omega t + \phi_0)$, is available, while the forcing frequency, Ω , might not be precisely known at a specific time.

An adaptive oscillator can “learn” information of an external force through its dynamic response, and this information is stored in plastic states. These plastic states can maintain an offset bias, whose value encodes the learned information. Adaptive frequency oscillators (AFOs) are a subset of adaptive oscillators, which contain a single plastic state that enables it to learn an external forcing frequency [1]. An array of coupled AFOs is similar to a system of coupled Kuramoto oscillators [33, 34], or an array of coupled phase-locked loops [35, 36].

Previously, dual populations of stochastic oscillators were studied, where each population was driven by a Kuramoto-type competition; this competition can produce phase locking [37]. Additionally, since the learning process for adaptive oscillators is embedded into the dynamical system, no pre- or post-processing is required for the oscillator to synchronize with the external force. Additional plastic states could be added onto the original system, so that more information concerning the forcing signal could be extracted and stored into states [14]. An array of AFOs can even be used to create complex waveforms, which has been used as a central pattern generator [20, 21]. As nonlinear oscillators occur in quantum systems [38, 39], these quantum limit cycles could be used to enhance quantum computation and communication efficiency [40] or to construct quantum adaptive oscillators for signal processing, phase-locking applications [41], and dynamic information storage.

However, noise is ubiquitous in physical systems. To the author's knowledge, only one study was completed that considered noise in an adaptive oscillator [29]. Stochastic effects are important in many systems, including electrical circuits [42], biological systems [43, 44], chemical reactions [45], magnetic systems [46], quantum systems [38], and mechanical systems [47, 48, 49]. Importantly, noise can introduce new dynamical effects to a nonlinear system, such as the well-known phenomenon of stochastic resonance [50, 51, 52, 53, 54]. Noise can desynchronize intrinsic localized modes [47], but noise can also induce synchronization of spin torque nano-oscillators [55]. Stochastic bifurcations have been studied for many nonlinear oscillators, such as the Duffing-van der Pol oscillator [56], a synthetic genetic oscillator [57], and an array of nonlinear oscillators [58].

The Hopf adaptive frequency oscillator is an adaptive oscillator, which is based on a Hopf oscillator that has been augmented to include an additional plastic state. This additional plastic state can extract and store the forcing frequency. Closely related to the current work, some stochastic dynamics of the Hopf oscillator in its normal form has also been studied. In the vicinity of a Hopf bifurcation, noise can trigger stochastic resonance of

the oscillator in four qualitatively different mechanisms [59] or coherence resonance [60], with some experimental results presented in [61]. For an ensemble of limit cycle oscillators, small amounts of noise cause the oscillators to synchronize, and large amounts of noise cause the oscillators to desynchronize into chaos [62]. In [29], a simplified Fokker-Planck equation of the Hopf AFO was derived, in which only the ω state was considered (i.e., the x and y states were disregarded).

Pendulums have been studied for millennia, and they appear in many different physical contexts. A simple mechanical pendulum can be created from a single mass that is constrained to rotate about a pivot point. More complex pendulums can be created, such as the 3D pendulum [63, 64], n -link pendulums [65], the Kapitza pendulum [66], or the Wilberforce pendulum [67]. Pendulums are crucial in modeling gait in both robotics [68, 69, 70] and biomechanics [71, 72, 73], and dynamical stability has been used to assess injury in athletes [74]. The simple pendulum is easy to fabricate, but it exhibits complex dynamics because of its nonlinear equations of motion. For this reason, the mechanical pendulum is a popular system to benchmark nonlinear controls [75, 76]. Chaos in pendular systems (especially the double pendulum) has been studied extensively [77, 78, 79, 80]. Related to their energy harvesting ability, pendulums have been studied extensively as vibration absorbers [81, 82, 83, 84, 85, 86].

Pendulums can also be used as energy harvesters, and several methods have been proposed. A ratcheting flywheel mechanism [87] and mechanical motion rectifier [88] have been used to harvest rotational oscillations, as well as rotational modes without a gearbox [89]. By incorporating elasticity into the pendulum's rod, a piezoelectric spring pendulum has been studied for both single pendulums [90] and double pendulums [91]. In these implementations, the piezoelectric elements harvest vibrations from the rod. In another configuration, the rotation point of a 3D pendulum was fixed to the end of a cantilever beam, which contains a piezoelectric patch [92]. Resonances between the pendulum and

cantilever are exploited to harvest more vibratory energy.

Unlike other types of vibratory control (e.g., [93, 94, 95]) and phase locked loops [96, 97, 98], adaptive oscillators use plastic dynamic states to *both learn and store information* from an external stimuli. For instance, adaptive frequency oscillators can synchronize their own frequency to that of an external stimuli without the aid of any pre- and post-processing of system response, and the frequency adaptation is embedded directly into the system's dynamics [1]. Adaptive oscillators can use a Hebbian learning rule, which was inspired by neuronal systems' ability to synchronize [5]. There are many viable applications of adaptive frequency oscillators. They have been used as central pattern generators for robotics locomotion control [20, 21]. These oscillators, because of the nature of their frequency adaptation, can also be used as adaptive controllers to find and match the natural frequency for the purpose of increasing energy-efficiency of a resultant gait [23, 24]. Adaptive oscillators have also be proposed as analog frequency analyzers [29]. Related to adaptive oscillators, a frequency self-tracking cantilever beam was studied and achieved by sliding an attached mass without any active control involvement [99]; however, this type of architecture relies on higher order modes. Their capability has been tested experimentally with a Hopf adaptive oscillator circuit [100], and the effects of noise on a Hopf adaptive oscillator was studied experimentally, numerically, and analytically using the full Fokker-Planck equation [101].

Adaptive oscillators were inspired by the synchronization of networks of neurons [5]. Dynamic Hebbian learning has been employed to encode the frequency in a plastic state of adaptive oscillators [1]. Adaptive oscillators have been proposed as analog frequency analyzers [29, 102] and controllers for robotic gait [103]. There are relatively few experimental results for adaptive oscillators, but a 4-state adaptive Hopf oscillator was implemented as an analog circuit [100] and a 3-state adaptive oscillator was implemented as a digital circuit [12]. The effects of noise on adaptive oscillators was studied with the full Fokker-

Planck equation with comparisons to a physical experiment [101] and with a simplified Fokker-Planck equation [29].

Adaptive frequency oscillators are similar to Kuramoto phase oscillators [33, 34, 104] and phase-locked loops (PLLs) [35, 36], since they are capable of learning an external forcing frequency. However, in the literature, adaptive oscillators are usually constructed from a nonlinear oscillator by including the addition of dynamic, plastic states. Although chaos has been exhibited by Kuramoto arrays [105] and PLLs [106, 107, 108, 109, 110, 111] chaos has not been explored in adaptive oscillators to the authors' knowledge.

The forced single pendulum [112, 113, 114] and the unforced double pendulum were two of the prototypical systems that can exhibit chaos [78, 79, 80]. A numerical investigation of an inverted pendulum on varying the base forcing amplitude displays the transition to chaos via an infinite sequence of period-doubling bifurcations [115]. The extensible pendulum, where the pendulum's rod is modeled as an extensible spring, can also exhibit chaos [116]. The bifurcation diagram was found for a mechanical, forced pendulum experiment [117] and a forced torsional pendulum [118]. An array of coupled nonlinear pendulum oscillators was studied to determine the effect of damping, the size of the ensemble, and the local coupling strength on its chaotic response [119]. Since the pendulum is a relatively simple system that exhibits chaos, it has been used to test chaotic controllers [120, 121].

Analog circuits have a history of being used as musical instruments. Electronic oscillators have been used as the building block for musical synthesizers [122]. As another example, the theremin's pitch is modulated by the performer through proximity to a cathode relay [123]. The chaotic Chua's circuit has even been demonstrated as an electronic musical instrument [124]. Virtual analog oscillators have also been used as a means of distortion synthesis [125], and the models for different physical instruments have been used to for music synthesis [126]. As the inverse of this sound synthesis procedure, the current paper explores the physical realization of a nonlinear oscillator as an analog circuit,

which can function as an instrument (similar to those discussed in [127, 128]) or a source of nonlinear distortion pedal for guitars (similar to those discussed in [129, 130]).

Adaptive oscillators are a type of nonlinear oscillator that can store information about an external input in its states [1]. By adding more states that correspond with vibratory features, more complex signals can be reconstructed [20, 21]. As an example, an oscillator with a static natural frequency can be modified to have a frequency state; this effectively changes the natural frequency of the oscillator from a static constant to a dynamic state that is time-dependent. For this reason, adaptive oscillators have been proposed as an analog signal analyzer [28, 29]. Adaptive oscillators could also be used as central pattern generators [22], energy harvesting [99], and robotic gait controllers [131]. Notably, adaptive oscillator networks have also been proposed for automatic music transcription [132, 133, 134] and beat detectors [135].

1.3 Outline

This dissertation is organized as follows:

- In Chapter 2, an analog implementation of a four-state adaptive oscillator, including design, fabrication, and verification through hardware measurement, is presented. The result is an oscillator that can learn the frequency and amplitude of an external stimulus over a large range. Notably, the adaptive oscillator learns parameters of external stimuli through its ability to completely synchronize without using any pre- or post-processing methods. Previously, Hopf oscillators have been built as two-state (a regular Hopf oscillator) and three-state (a Hopf oscillator with adaptive frequency) systems via VLSI and FPGA designs. Building on these important implementations, a continuous-time, analog circuit implementation of a Hopf oscillator with adaptive

frequency and amplitude is achieved. The hardware measurements and SPICE simulation show good agreement. To demonstrate some of its functionality, the circuit's response to several complex waveforms, including the response of a square wave, a sawtooth wave, strain gauge data of an impact of a nonlinear beam, and audio data of a noisy microphone recording, are reported. By learning *both* the frequency and amplitude, this circuit could be used to enhance applications of AOs for robotic gait, clock oscillators, analog frequency analyzers, and energy harvesting. This work is adapted from [100].

- In Chapter 3, the stochastic dynamics of adaptive frequency Hopf oscillators when driven by noise are considered. Previously, it has been shown that simplified analysis of the Fokker-Planck equation results in affecting the plastic frequency state of these oscillators. However, when full Fokker-Planck analysis is considered, we demonstrate new behaviors due to changes in oscillation amplitude in addition to frequency. Here, we show that the plastic frequency state of these oscillators may benefit from enhanced learning due to small amplitudes of noise, converge to incorrect values for medium amplitudes of noise and collapse to zero in the limit for large amplitudes of noise. Interestingly, not all state-variables collapse equally which leads to a limit cycle collapsing into single dimensional oscillations. These behaviors are compared analytically through the Fokker-Planck equation, numerically using the Euler-Maruyama and cumulant neglect methods and finally validated experimentally using an analog, electronic circuit. These results show that noise can enhance, mislead or even reduce the dimensionality of plastic states in adaptive Hopf oscillators. This work is adapted from [101].
- In Chapter 4, a typical mechanical pendulum is modified to have an adjustable rod length to create a pendulum adaptive frequency oscillator. Since the resonance fre-

quency of the pendulum is a function of the rod length, this allows the pendulum to learn and encode frequency information from an external source. An experimental pendulum adaptive frequency oscillator is designed and constructed, and its performance is compared to numerical simulations. This nonlinear pendulum was approximated as a Duffing oscillator through the method of multiple scales to determine the physical constants of the experiment by using a curve fit. Utilizing the pendulum adaptive frequency oscillator's dynamics, this system is able to learn a resonance condition and store this information in the rod length. This causes the system to seek resonance, even with considerable nonlinearity. As pendulums can be used to harvest energy, this type of adaptation could be used to further exploit vibratory energy sources. This work is adapted from [136].

- In Chapter 5, the horizontally forced pendulum adaptive frequency oscillator is constructed as a physical experiment, which seeks a resonance condition by modifying the length of the pendulum's rod. This system stores the external forcing frequency when the external amplitude is small, while it can store the resonance frequency, which is affected by the nonlinearity of the pendulum, when the external amplitude is large. Furthermore, for some frequency ranges, the pendulum adaptive frequency oscillator can exhibit chaotic motion when the amplitudes are large. This adaptive oscillator could be used as a smart vibratory energy harvester device, but this chaotic region could degrade its performance by using supplementary energy to modify the rod length. The pendulum adaptive frequency oscillator's equations of motions are discussed, and a field-programmable analog array is used as an experimental realization of this system. Bifurcation diagrams are shown for both the numerical simulations and experiments, while period-3 motion is shown for the numerical simulations. As little work has been done on the stability of adaptive oscillators,

the authors believe that this work is the first demonstration of chaos in an adaptive oscillator. This work is adapted from [137].

- In Chapter 6, the utilization of a Hopf adaptive frequency oscillator as a musical instrument is explored. Building on previous work in the lab that studied asphaltophones [138], adaptive oscillators are nonlinear oscillators that are capable of learning and storing information in plastic states. The Hopf adaptive frequency oscillator can be constructed by including an additional plastic state, while using the classical Hopf oscillator as a base. An analog circuit is designed and fabricated, whose dynamics closely match the Hopf adaptive frequency oscillator equations. A procedure to use this analog circuit as a musical instrument is described, which includes the addition of pedal points. Although similar to other analog electronics instruments such as the theremin, the authors believe this is the first time that an adaptive oscillator has been implemented as a musical instrument or analog nonlinear distortion technique. Since the adaptive oscillator locks to a particular frequency component of an external signal, the adaptive oscillator produces a unique audio effect. This Hopf adaptive frequency oscillator could be modified to be a free-standing instrument to be played with the human voice or used as a guitar distortion effect pedal. In this paper, the process of using the circuit is detailed, and an example of this technique is shown, using a vocal and piano recording of *Ave Maria*. This work is adapted from [139].
- In Chapter 7, concluding remarks and future directions are discussed. This dissertation provides answers to some fundamental questions about adaptive oscillators, but it also points to the fact that adaptation is a process that adds significant complexity. This adaptation, however, allows systems to learn information, without the need of separate signal processing and data storage capabilities.

CHAPTER

2

A FOUR STATE ADAPTIVE HOPF OSCILLATOR

In the following sections, a standard Hopf oscillator is described. Then, plastic states are progressively added to the Hopf equations by modifying the system dynamics as reported in [1, 14]. This treatment results in 1) the addition of a fourth, plastic state and 2) three systems that inform circuit designs based on state variable networks.

2.1 Two-state System

The Hopf oscillator is a nonlinear oscillator described by the following ordinary differential equations (ODEs) [140]:

$$\begin{aligned}\dot{x} &= (\mu - (x^2 + y^2))x - \omega_0 y + k(a \sin(\Omega t + \phi_0)) \\ \dot{y} &= (\mu - (x^2 + y^2))y + \omega_0 x\end{aligned}\tag{2.1}$$

Here, ω_0 is a resonance constant, μ is a constant that controls the limit cycle radius, and k is a coupling constant. The input signal is $a \sin(\Omega t + \phi_0)$, where a is the amplitude of the sinusoid, Ω is the external forcing frequency, and ϕ_0 is the phase of the input sinusoid. This nonlinear oscillator is used as the building block for the subsequent adaptive oscillator systems. Since this system is not adaptive, the frequency-amplitude relationship has a single peak, as presented in Fig 2.5.

2.2 Three-state System

The Hopf Adaptive Frequency Oscillator (HAFO) may learn the frequency of an external stimuli; this implies that the HAFO is a three-state nonlinear oscillator with *dynamical plasticity*. This synchronization process is appealing, as it does not need any pre- or post-processing. Here, y is used to replace the term $\frac{y}{\sqrt{x^2+y^2}}$ that was proposed in [1]. If the constants in Eq. 2.1 are chosen to create a stable limit cycle, this limit cycle will have a constant radius after the transient response decays. This modification simplifies the circuit implementation in a similar manner shown in [11]. Fig 2.1 compares the originally derived AFO in [1] with the simplifications imposed on Eq. 2.2. After their transient response decays, the outputs of the two systems are qualitatively similar. With this modification, the complexity of the circuit implementation is highly reduced and the learning time of the

ω state is decreased. The frequency information stored in the third state, ω , is achieved by the system's intrinsic dynamics. The first two ODEs are the classical form of the Hopf oscillator, and the third ODE allows for frequency adaptation. Input forcing causes the resulting HAFO output to increase or decrease in frequency based on a frequency difference referenced to the input signal. The three-state system's ODEs are given as follows:

$$\begin{aligned}\dot{x} &= (\mu - (x^2 + y^2))x - \omega y + k(a \sin(\Omega t + \phi_0)) \\ \dot{y} &= (\mu - (x^2 + y^2))y + \omega x \\ \dot{\omega} &= -k(a \sin(\Omega t + \phi_0))y\end{aligned}\tag{2.2}$$

It should be noted that the resonance constant, ω_0 , in eq. 2.1 has been replaced by the state, ω . By allowing the resonance frequency to be a state variable instead of a constant, the Hopf oscillator may now learn the external forcing frequency. It should also be noted that the external input signal is injected into both the x and the ω states.

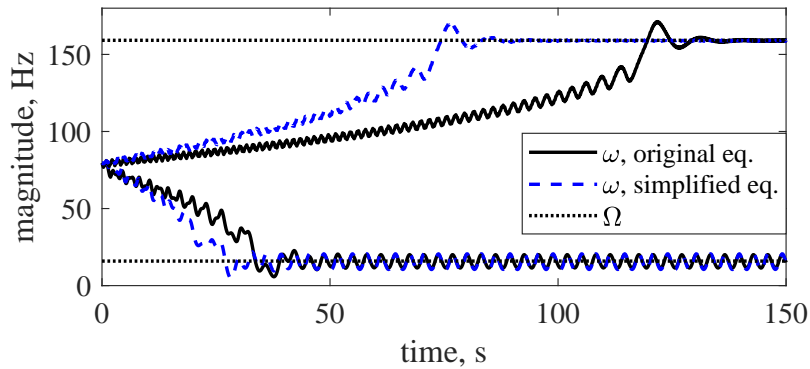


Figure 2.1: **Comparison of original and modified AFOs.** For two forcing frequencies, a comparison of the original AFO as proposed by [1] and the simplified system, as given in Eq. 2.2, is shown.

2.3 Four-state System

By adding another state and modifying the equation for \dot{x} to include $x\alpha$ in Eq. 2.2, a four-state oscillator [14] can be created that learns the amplitude of the external signal in addition to frequency. It should be noted that the magnitude of α at steady state will deviate from the input amplitude when $\mu \neq 1$. Detailed information concerning the derivation of these equations was reported in [1, 103]; however, few circuit designs have been reported and little hardware verification exists in the literature. The four-state system's ODEs are given as follows:

$$\begin{aligned}\dot{x} &= (\mu - (x^2 + y^2))x - \omega y + k(a \sin(\Omega t + \phi_0) - x\alpha) \\ \dot{y} &= (\mu - (x^2 + y^2))y + \omega x \\ \dot{\omega} &= -k(a \sin(\Omega t + \phi_0) - x\alpha)y \\ \dot{\alpha} &= \eta(a \sin(\Omega t + \phi_0) - x\alpha)x\end{aligned}\tag{2.3}$$

Here, η is a coupling constant. It should also be noted that the external input signal is injected into the x , ω , and α states. In the four-state system, Hebbian learning (i.e., subtracting $x\alpha$ from the external input signal) is used to enforce that ω and α converge to the external input signal.

2.4 Local Analysis

To gain a better understanding of adaptive oscillators, a local analysis is performed on the Hopf adaptive frequency oscillator (eq. 2.2). For comparison, this local analysis will first be used on the classical Hopf oscillator (the two-state system represented by eq. 2.1). Removing the forcing term from this equation, the Jacobian may be written as:

$$J_1 = \begin{bmatrix} -3x^2 - y^2 + \mu & -2xy - \omega_0 \\ -2xy + \omega_0 & -x^2 - 3y^2 + \mu \end{bmatrix} \quad (2.4)$$

For the fixed point $(x, y) = \vec{0}$, Mathematica was used to find the eigenvalues of this system. The eigenvalues of J_1 are the conjugate pair, $\mu \pm \omega_0 i$. This is because the unforced Hopf oscillator given by eq. 2.1 with $\mu > 0$ possesses a limit cycle with frequency ω_0 [140].

To perform this analysis for the three-state system, the forcing term, $\sin(\Omega t + \phi_0)$, is replaced by an additional oscillator in order for the system of equations to be autonomous, as in [49]:

$$\begin{aligned} \dot{u} &= u + \Omega v - u(u^2 + v^2) \\ \dot{v} &= v - \Omega u - v(u^2 + v^2) \end{aligned} \quad (2.5)$$

The system represented by eq. 2.5 has a supercritical Andronov-Hopf bifurcation [141]. Replacing the forcing term in eq. 2.2, the following system of equations obtained:

$$\begin{aligned} \dot{x} &= (\mu - (x^2 + y^2))x - \omega y + k(au) \\ \dot{y} &= (\mu - (x^2 + y^2))y + \omega x \\ \dot{\omega} &= -k(au)y \\ \dot{u} &= u + \Omega v - u(u^2 + v^2) \\ \dot{v} &= v - \Omega u - v(u^2 + v^2) \end{aligned} \quad (2.6)$$

These equations are autonomous, and their Jacobian may be written as:

$$J_2 = \begin{bmatrix} j_1 & j_2 & j_3 & j_4 & 0 \\ j_5 & j_6 & j_7 & 0 & 0 \\ 0 & j_8 & 0 & j_9 & 0 \\ 0 & 0 & 0 & j_{10} & j_{11} \\ 0 & 0 & 0 & j_{12} & j_{13} \end{bmatrix}$$

where $j_1 = -3x^2 - y^2 + \mu$, $j_2 = -2xy - \omega$, $j_3 = -y$, $j_4 = ak$, $j_5 = -2xy + \omega$, $j_6 = -x^2 - 3y^2 + \mu$, $j_7 = x$, $j_8 = -aku$, $j_9 = -aky$, $j_{10} = 1 - 3u^2 - v^2$, $j_{11} = -2uv + \Omega$, $j_{12} = -2uv - \Omega$, $j_{13} = 1 - u^2 - 3v^2$. For the fixed point $(x, y, u, v) = \vec{0}$, the eigenvalues for the J_2 are $1 \pm \Omega i$, $\mu \pm \omega i$, and 0. The conjugate pair $1 \pm \Omega i$ corresponds to the forcing oscillator, with forcing frequency Ω . The conjugate pair $\mu \pm \omega i$ corresponds to the Hopf adaptive frequency oscillator; thus, the Hopf adaptive frequency oscillator oscillates with frequency equal to the third state, ω . The eigenvalue of 0 corresponds to the ω state. It is not stable or unstable, which allows this state to plastically deform to the forcing frequency.

2.5 Experimental Results

2.5.1 Circuit Design

A circuit implementation of the system described by Eq. 2.3 was designed, fabricated, and tested. For clarification, a simplified schematic is shown in Fig 2.3. Three potentiometers, annotated as RV1, RV2 and RV3, are set to 10k Ω , 12.5k Ω , 200k Ω , respectively. Additionally, the tunable resistance ranges of RV1, RV2 and RV3 are from 0 Ω to 500k Ω . All unlabeled resistors are 1k Ω . The capacitors, labeled C1, C2, C3, and C4, have a capacitance of 0.1 μ F. The experimental PCB is shown in Fig 2.2.

This implementation was realized using TL082 opamps and AD633 multipliers in stan-

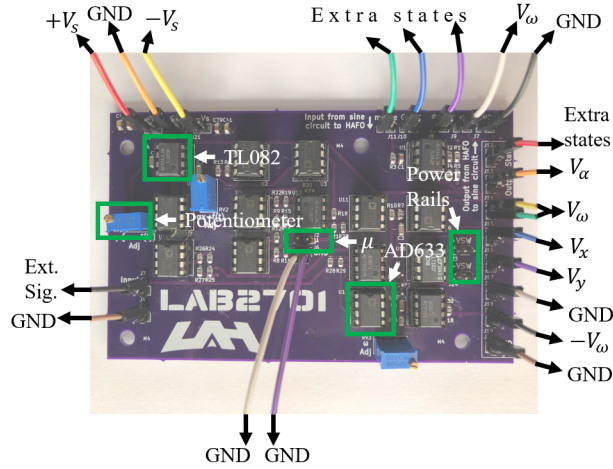


Figure 2.2: **Printed circuit board.** PBC used in experiments. Here, “Ext. Sig.” is given by $V_P(t)$.

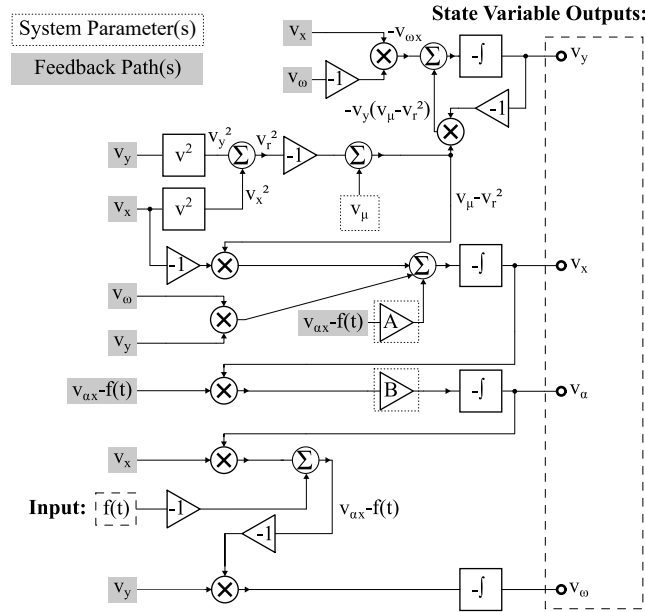


Figure 2.3: **Simplified circuit schematic.** A simplified schematic for the four-state adaptive system, with states V_x , V_y , V_omega , and V_alpha .

dard configurations with 0805 SMD passive components with 1% error tolerance for resistors and 2% error tolerance for capacitors. Three potentiometers were included to tune the coupling strengths associated with the first, third, and fourth states.

The dynamical system in Eq. 2.3 was then mapped to Eq. 2.7. This was done in a

manner similar to that discussed in [142], where Kirchhoff's laws may be used to create a standard, voltage-mode opamp integrator configuration paired with voltage multipliers. This also resembles the analog circuit implementations shown in [143]. where $V_P(t) = [a \sin(\Omega t + \phi_0)] - x\alpha$ is an external stimulus.

$$\begin{aligned}
\dot{V}_x &= -\frac{1}{R1C1}(V_\mu - (V_x^2 + V_y^2))V_x + \frac{1}{R2C1}V_\omega V_y - \frac{1}{RV2C1}V_P(t) \\
\dot{V}_y &= -\frac{1}{R3C2}(V_\mu - (V_x^2 + V_y^2))V_y - \frac{1}{R4C2}V_\omega V_x \\
\dot{V}_\omega &= \frac{1}{RV3C3}V_P(t)V_y \\
\dot{V}_\alpha &= -\frac{1}{RV1C4}V_\eta V_P(t)V_x
\end{aligned} \tag{2.7}$$

Here, the states V_x , V_y , V_ω , and V_α correspond to the voltage outputs of opamp integrators. This methodology is similar to the realization of integrator-based state variable networks.

By connecting the output pin headers of the α state to the ground, the four-state system can be transformed into the three-state system. This effectively sets the αx term in the \dot{x} , $\dot{\omega}$, and $\dot{\alpha}$ equations to zero. By connecting the output pin headers of both the α state to the ground and the ω state to a constant, the four-state system can be transformed into a regular two-state Hopf oscillator. Therefore, the PCB can switch its functionality between a two-state, three-state, and four-state system. The PCB, whose dynamics is represented by Eq. 2.7 was fabricated, and the experimental results from this PCB are depicted in Figs 2.4 and 2.5.

2.5.2 Range of Operation

The results shown in Fig 2.4 are the time response of the x , ω , and α states. The results display qualitatively similar characteristics.

The simulation results shown in Fig 2.5 are a comparison of SPICE simulations and the experimental results of the PCB. It should be noted that no filters were used on any

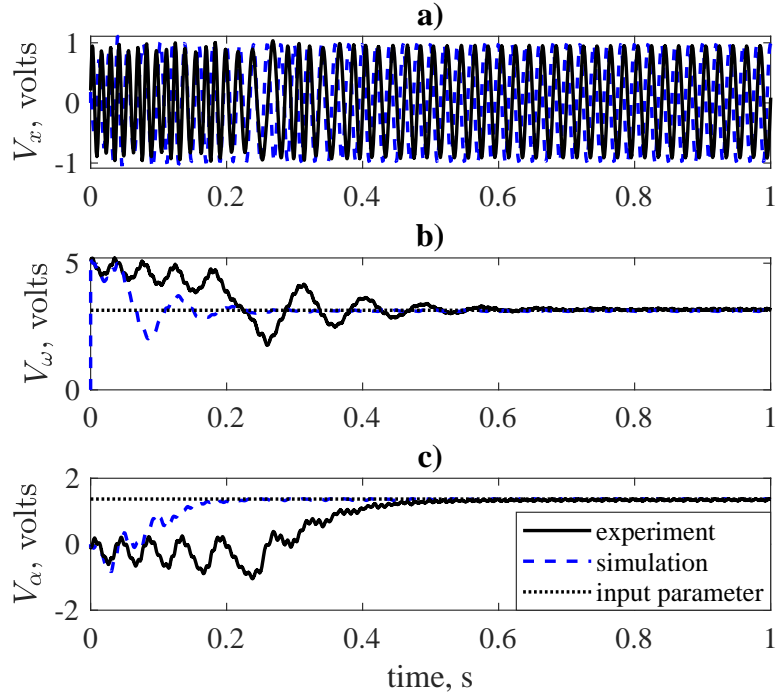


Figure 2.4: **Time history of the four-state oscillator.** Experimental data is plotted as a black solid line, SPICE simulation data is plotted as a blue dashed line, and the sinusoid's Ω and a are plotted as dotted lines.

of the results collected from the experiments. In Fig 2.5, the black solid lines represent experimental data, while the blue dashed lines represent simulation results. The black dash-dotted and blue dotted lines show the percent error of the learned input of the experiment and simulation, respectively.

All the external stimuli for the experimental results were generated with MATLAB and input to the PCB with a National Instruments (NI) cDAQ-9174. In Fig 2.5(a), the frequency-amplitude response of the two-state Hopf oscillator is shown. A frequency sweep was performed from 5 Hz to 210 Hz. The frequency-amplitude response from the SPICE simulations show qualitatively similar results with slightly different resonance frequency and corresponding magnitude. There is only one resonance peak near ω_0 (which is marked as a vertical dashed line) in the tested frequency range, since it is not an AO. In Fig 2.5(b),

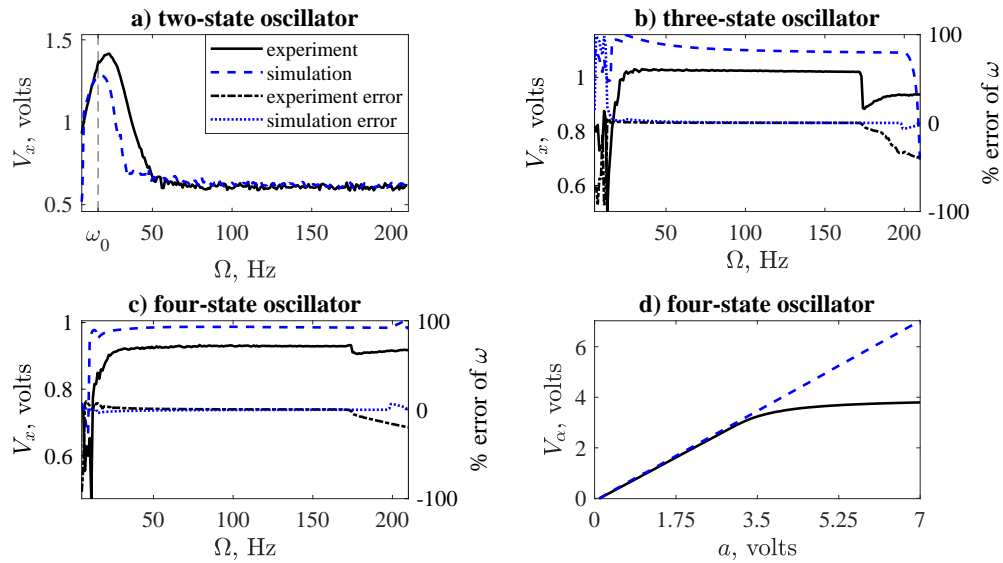


Figure 2.5: **Range of Operation.** Comparison of results of PCB experiment and SPICE simulations, with $k = 0.5$, $a = 1.5$ (except (d)), $\omega_0 \approx 15.9$ Hz, and $\mu = 1$ for both the simulations and the experiments. It should be noted that the frequency-amplitude relationship is reported for the x -state, while the percent error is reported for the ω -state. Noting that for the four-state system (bottom-right), the oscillator learns the correct amplitude from approximately 0 to 3; after 3, nonlinear effects in the PCB cause the simulation and experimental results to diverge.

the frequency-amplitude response of the three-state system is shown. Instead of a single resonance, the three-state system maintains a large value over a wide range of frequencies. The percent error is calculated as $\frac{\Omega - \langle \omega \rangle}{\Omega} \times 100$, where $\langle \omega \rangle$ is the mean of the ω state at steady state. For the experiment, the error is less than 2% when the forcing frequency is between 19 Hz and 173 Hz. For the simulations, the percent error is less than 3% when the forcing frequency is between 20 Hz and 198 Hz. The frequency-amplitude relationship of the three-state oscillator matches closely with the percent error relationship (i.e., when the amplitude is high, the percent error is small).

In Fig 2.5(c), the frequency-amplitude response of the four-state system is shown. For the experiment, the percent error is less than 2.5% if the forcing frequency is between 25 Hz

and 174 Hz. For the simulations, the percent error displays qualitatively similar behavior. In Fig 2.5(d), the resulting α when sweeping the input amplitude from 0 to 7 for both the simulations and the experiment are shown. The experimental results show that the linear relationships between a and α is maintained until $a > 3$. A linear curve-fit was performed in MATLAB (for $a < 3$), and the slope of the line was 0.986 for the experiment. For the simulation, the linear relationship was maintained even outside this region, and the slope of the curve-fit was 1.018. Both the experiments and simulations have less than 2% error. It should be noted that the scalar parameter, μ , controls the amplitude of x at steady state, and a slight deviation of μ generated by the power supply from its expected value will cause an error between the experiment and the desired result. Additionally, the nonlinearity of the electrical components used in the simulations are not perfectly modeled, so the resulting differences inevitably occur in Fig 2.5.

2.5.3 Verification of Other Waveforms

After the initial testing to determine the range of operation of the experimental four-state adaptive oscillator system, the circuit was then tested using several complex waveforms. A signal generator was used to create a square wave and a sawtooth wave; the square wave was constructed so that the fundamental frequency changes over time. These signals are more complex than a simple sinusoidal wave, as they are composed of an infinite series of sinusoids. The results are shown in Figs 2.6 and 2.7.

Further, the voltage data from a strain gauge that was mounted to a nonlinear beam was used as an input to the adaptive oscillator circuit. By impacting the beam with a hammer, a vibratory system identification was performed to find the first natural frequency of the beam [2]. The results are shown in Fig 2.8.

A vehicle's response to an asphaltophone was recorded with a microphone [138]. This

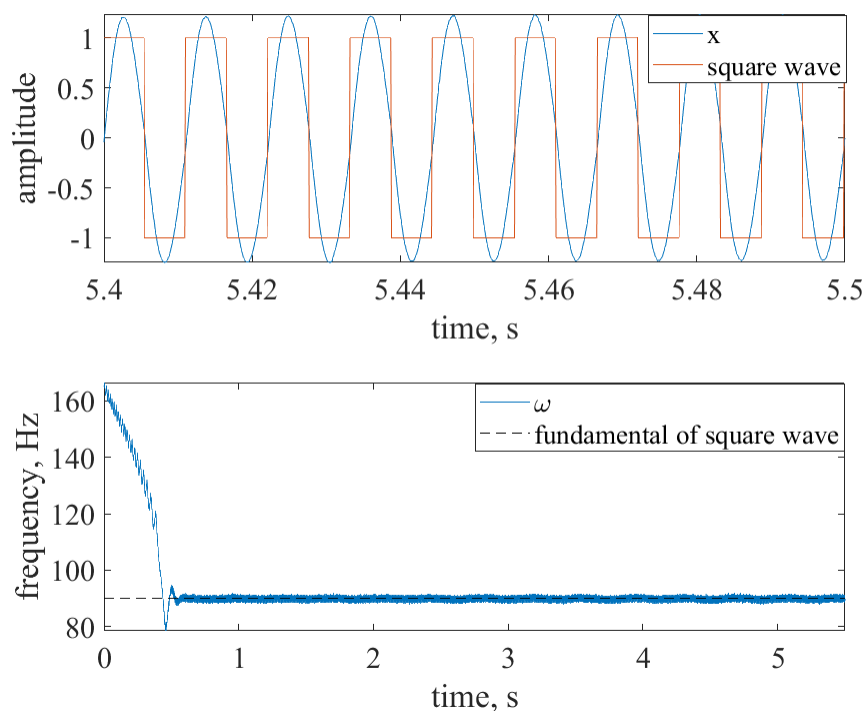


Figure 2.6: **Square wave results.** A generated square wave with a varying fundamental frequency was used as the input to the adaptive oscillator circuit. The circuit was able to learn the fundamental frequency of the square wave. Top: The time history of the x state and the generated square wave are shown. Bottom: The circuit learns the fundamental frequency of the square wave, even though the frequency was varying over time.

recording had high amplitude low-frequency noise; the amplitudes of this noise were larger than the signal. In this recording, the asphaltophone was designed to reproduce a note of F3 (174.6141 Hz) when the vehicle is traveling 35 miles per hour. As the note is rather short, it was concatenated to create a longer signal. The low-frequency noise was filtered from the recording, and the filtered recording was input to the circuit. It should be noted that this example is the only time that filtering was used in this paper. The results are shown in Fig 2.9.

Last, a robotic player trumpet playing an A—440 note (440 Hz) was recorded. This note was then rescaled in time to produce a 110 Hz note. Even though the trumpet’s timbre has

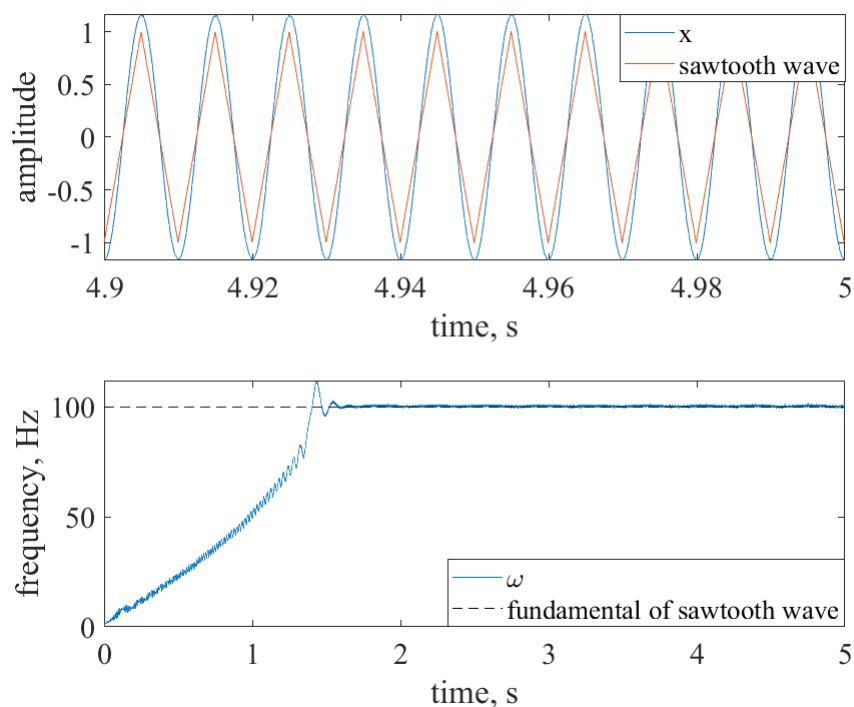


Figure 2.7: **Sawtooth wave results.** A generated sawtooth wave was used as the input to the adaptive oscillator circuit. The circuit was able to learn the fundamental frequency of the sawtooth wave. Top: The time history of the x state and the generated sawtooth wave are shown. Bottom: The circuit learns the fundamental frequency of the sawtooth wave.

higher harmonics, the adaptive oscillator is still able to learn the fundamental frequency. The results are shown in Fig 2.10.

2.6 Conclusion

In this chapter, an adaptive oscillator was designed, fabricated, and tested. SPICE simulations were compared to the experimental results. The results collected from the PCB show qualitatively similar behavior to the adaptive oscillator's simulated equations. The four-state oscillator was shown to learn the forcing frequency successfully from approximately 25 Hz to 175 Hz within 3% error and input amplitudes from approximately 0 to 3 within

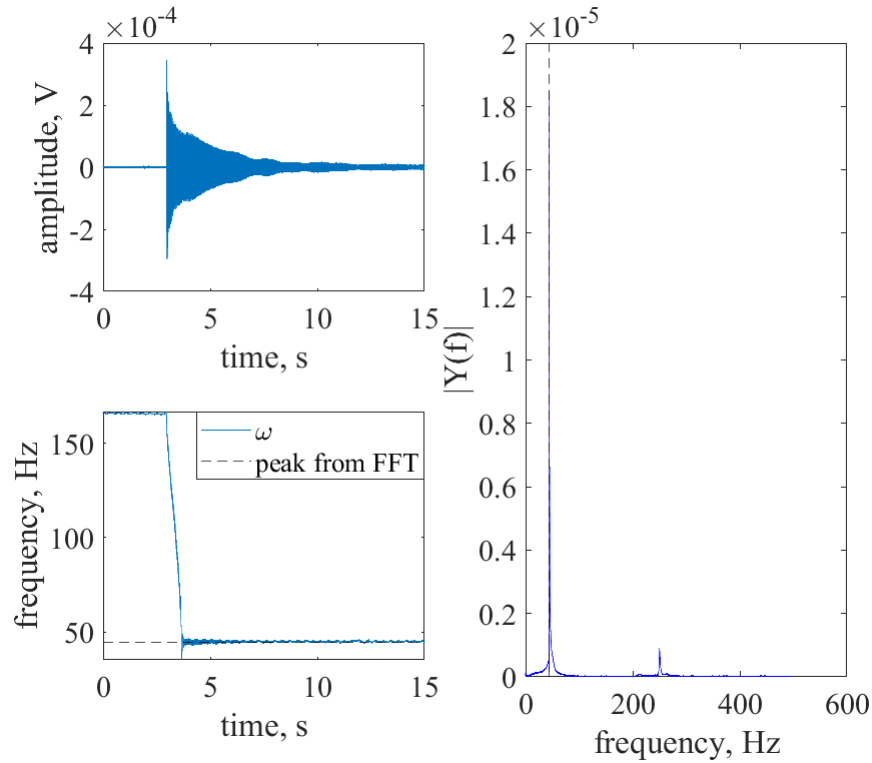


Figure 2.8: **Impact test results.** Strain gauge data [2] was directly input to the adaptive oscillator circuit. The circuit learned the natural frequency of the nonlinear beam. Top-left: The time history of the strain gauge's voltage is shown. The impact of the beam happens at approximately 3 seconds. Bottom-left: The circuit learns the first natural frequency of the beam. Right: An FFT of the beam is shown, with the first natural frequency marked by a dashed, vertical line.

2% error. These experimental results were in close agreement with the SPICE simulation results. There are two types of nonlinearity in this paper. The nonlinearities of the ODEs are desired, and they cause the learning to happen. The circuit nonlinearities (e.g., parasitic elements, etc.) are not modeled, and these nonlinearities cause errors in the experimental results.

As demonstrated in Figs 2.6, 2.7, 2.8, 2.9, and 2.10, this adaptive frequency oscillator is capable of learning more complex waveforms, in addition to simple sinusoids. As demonstrated in Fig 2.8, this oscillator is capable of reporting the first natural frequency of a

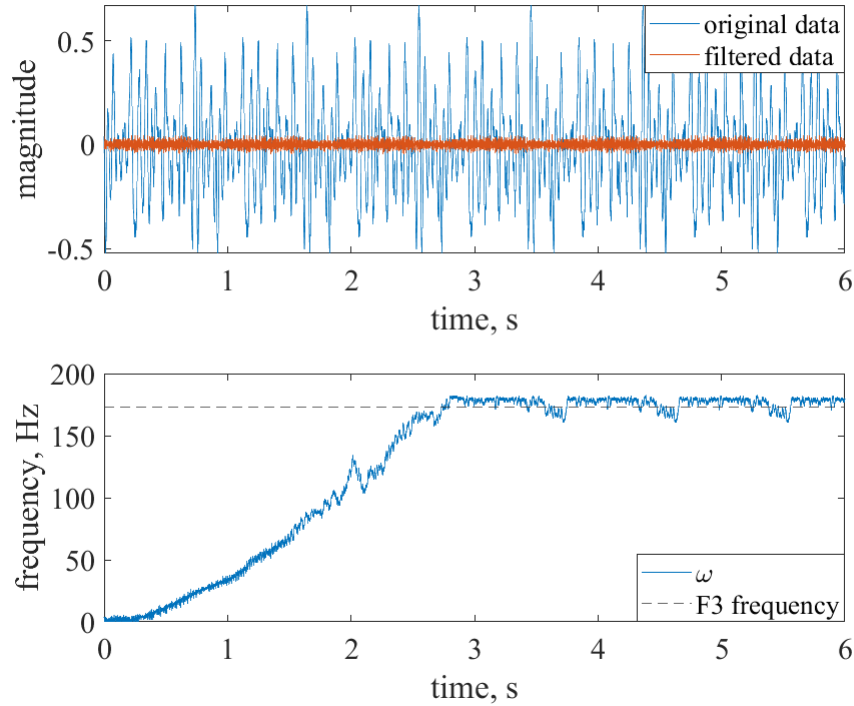


Figure 2.9: **Asphaltophone results.** A filtered audio recording of an asphaltophone was input to the adaptive oscillator circuit. Top: The original signal and the filtered signal are plotted. Bottom: The circuit learns the F3 note from the asphaltophone. The data is still quite noisy, so the ω state has fluctuations about the F3 frequency.

mechanical system, without the need of a fast Fourier transform or other post-processing techniques. The implementation presented here could be used as an analog controller for walking robots, a circuit component of clock oscillators, an analog signal analyzer, or a component of a electromechanical energy harvester (such as that presented in [144]).

It should also be mentioned that other types of implementations of adaptive oscillators could be achieved. For example, adaptive oscillators could likely be implemented in a field programmable analog array, such as the implementation of a chaotic oscillator in [145]. The circuit presented in this paper is a prototype system that is a physical embodiment of eq. 2.3, which could be further refined for specific, practical applications.

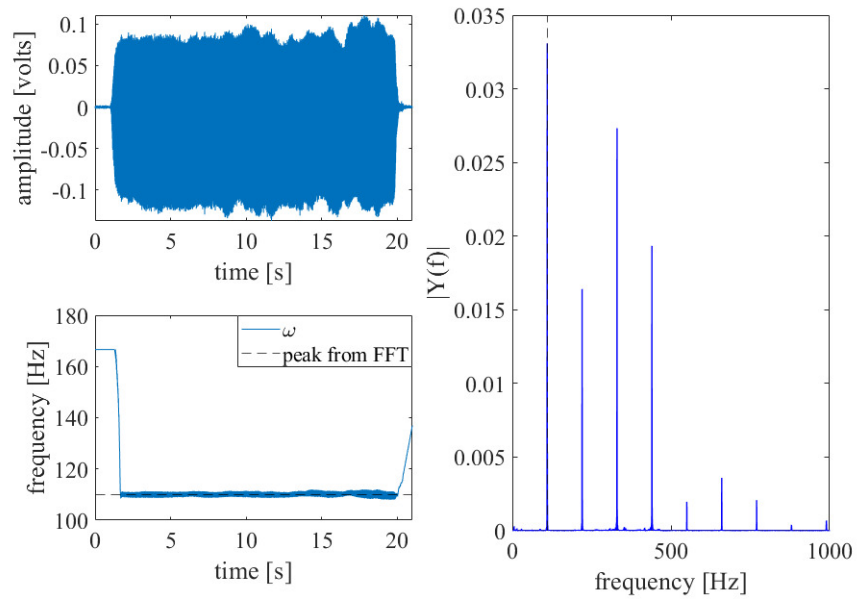


Figure 2.10: **Robotic player trumpet results.** A scaled recording of a robotic player trumpet was input to the adaptive oscillator circuit. The circuit learned the natural frequency of the trumpet’s note. Top-left: The time history of the trumpet recording is shown. The time was rescaled by a factor of four. Bottom-left: The circuit learns the first natural frequency of the note. Right: An FFT of the note is shown, with the first natural frequency marked by a dashed, vertical line.

CHAPTER

3

STOCHASTIC EFFECTS ON A HOPF ADAPTIVE FREQUENCY OSCILLATOR

In this study, numerical, analytical, and experimental results are presented for the Hopf AFO in the presence of stochastic forcing. In Section 3.1, the ordinary differential equations for the adaptive oscillator are presented. In Section 3.2, the stochastic differential equations for the adaptive oscillator are presented, and direct numerical simulations using the Euler-Maruyama method [146] are implemented to compare with the semi-analytical formulation and experimental results. In Section 3.3, the full Fokker-Planck equation is derived, and the results are found to be significantly different than the approximation found in [29]. The

cumulant neglect method [147] is utilized to solve the Fokker-Planck equation to obtain a semi-analytical solution to the adaptive oscillator. In Section 3.4, a Hopf AFO was fabricated as an electronic circuit to serve as a physical embodiment of an adaptive oscillator. Each of these methods showed qualitatively similar behavior. Namely, for small amounts of noise, the mean of the frequency state quickly converges to the correct frequency. For medium amounts of noise, the mean of the frequency state converges to an incorrect frequency. In the limit of large noise, the mean of the frequency state and the mean amplitude of the limit cycle both converge to zero.

3.1 Equations for a Hopf Adaptive Frequency Oscillator

The equation of motion of the three state Hopf AFO is written below:

$$\begin{aligned}
 \dot{x} &= (\mu - (x^2 + y^2))x - \omega y + k_x(a \sin(\Omega t)) \\
 \dot{y} &= (\mu - (x^2 + y^2))y + \omega x \\
 \dot{\omega} &= -k_\omega(a \sin(\Omega t))y
 \end{aligned} \tag{3.1}$$

The first and second states correspond to a forced Hopf oscillator [140], except that the ω term is not a constant. The third state is a plastic state, which may learn the forcing frequency without any pre- and post-processing procedures. Eq. 3.1 is a modified version of the equations proposed in [1], except that y is used to replace the term $\frac{y}{\sqrt{x^2+y^2}}$ to simplify the equations. The constants in Eq. 3.1 are selected to create a stable limit cycle, which will generate a constant radius after the transient response decays.

3.2 Euler-Maruyama Simulations

To consider the stochastic effects on this system, noise is injected into Eq. 3.1 by replacing $a \sin(\Omega t)$ with $a \sin(\Omega t) + \dot{W}(t)$. The term, $\dot{W}(t)$, denotes white Gaussian noise. It is the derivative of Brownian motion. Eq. 3.1 can thus be re-written as:

$$\begin{aligned}\dot{x} &= (\mu - (x^2 + y^2))x - \omega y + k_x(a \sin(\Omega t) + \sigma \dot{W}(t)) \\ \dot{y} &= (\mu - (x^2 + y^2))y + \omega x \\ \dot{\omega} &= -k_\omega(a \sin(\Omega t) + \sigma \dot{W}(t))y\end{aligned}\tag{3.2}$$

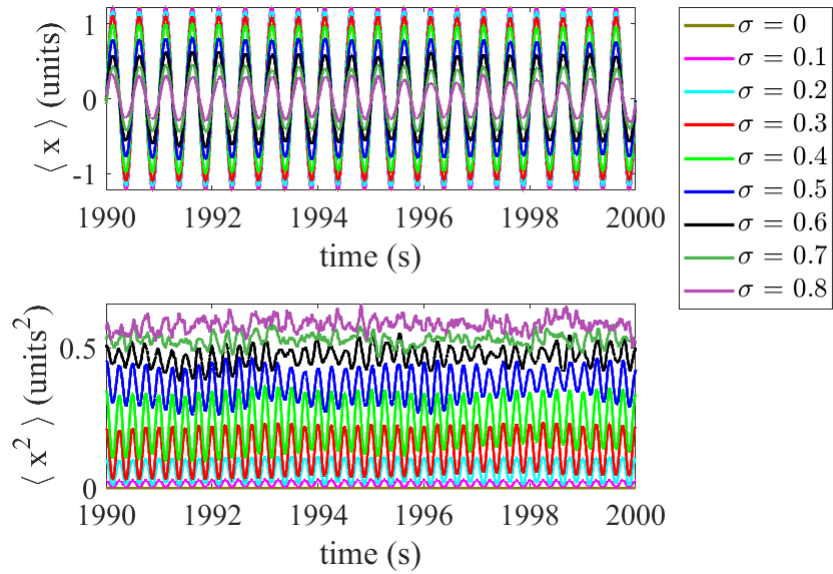


Figure 3.1: **Euler-Maruyama simulations: x state.** Mean and variance of x obtained from 500 ensemble averages of Euler-Maruyama simulations. As the noise amplitude is increased, $\langle x \rangle$ decreases.

Since the increments of Brownian motion are independent, its derivative does not exist with probability one [148]. For this reason, $\dot{W}(t)$ is a “mnemonic” derivative. While the derivative of Brownian motion does not exist, its differential form dW does exist. Thus, Eq.

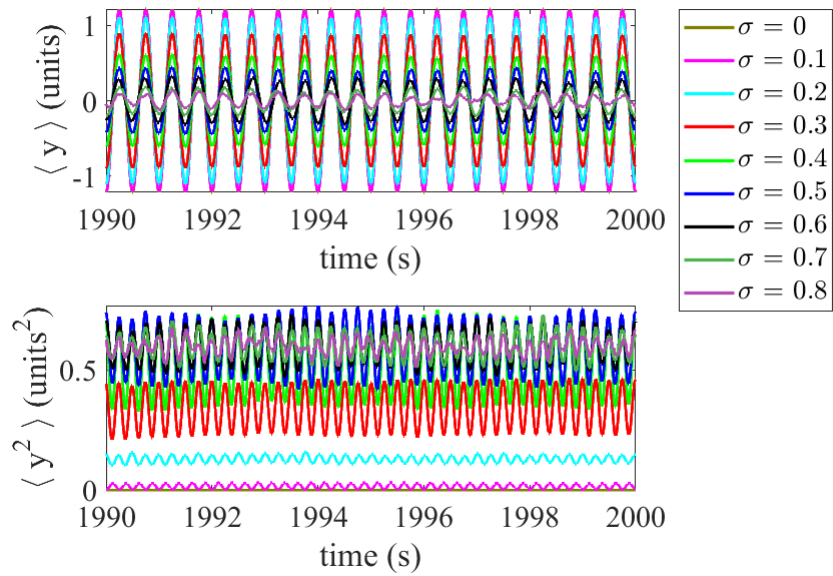


Figure 3.2: **Euler-Maruyama simulations: y state.** Mean and variance of y obtained from 500 ensemble averages of Euler-Maruyama simulations. As the noise amplitude is increased, $\langle y \rangle$ decreases.

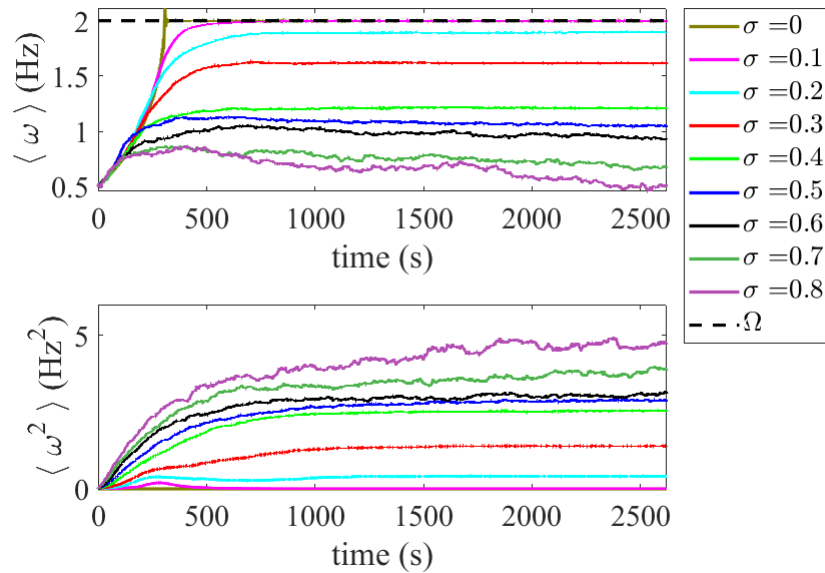


Figure 3.3: **Euler-Maruyama simulations: ω state.** Mean and variance of ω obtained from 500 ensemble averages of Euler-Maruyama simulations. For small amount of noise, $\langle \omega \rangle$ quickly approaches Ω without overshoot error. As the noise amplitude is increased, the $\langle \omega \rangle$ value converges to the incorrect value.

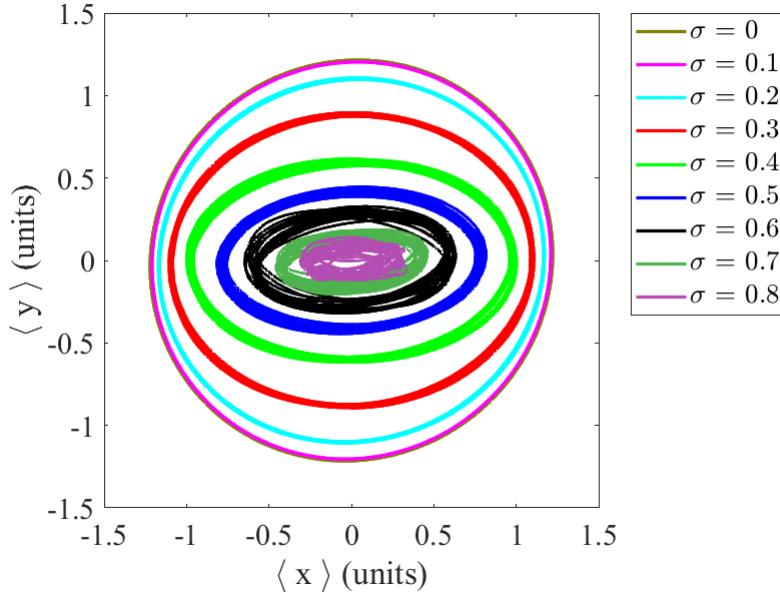


Figure 3.4: **Euler-Maruyama simulations: limit cycles.** For the Euler-Maruyama simulations, the limit cycle of $\langle x \rangle$ vs. $\langle y \rangle$ is shown. As the noise level increases, the two dimensional limit cycle begins to collapse into one dimensional oscillations when considering the averaged dynamics.

3.2 can be written in a differential form as following:

$$\begin{aligned}
 dx &= ((\mu - (x^2 + y^2))x - \omega y + k_x a \sin(\Omega t))dt + k_x \sigma dW \\
 dy &= ((\mu - (x^2 + y^2))y + \omega x)dt \\
 d\omega &= (-k_\omega a \sin(\Omega t)y)dt - k_\omega \sigma y dW
 \end{aligned} \tag{3.3}$$

This system of Langevin equations[149, 150] is then integrated as an Itô integral. The Euler-Maruyama (EM) method is an extension of Euler's method to stochastic differential equations [146]; here, the EM method is implemented to obtain the numerical solutions for Eq. 3.3. This routine was written in MATLAB, and 500 simulations for each noise amplitudes were performed. For each batch of simulations, the ensemble average for each of the three variables was calculated for each time step. For the numerical simulations, the constants are set such that $k_x = 1$, $k_\omega = 1$, $a = 1$, $\mu = 1$, and $\Omega = 4\pi$. The incremental noise, dW , is

random with a mean equal to zero and a standard deviation equal to \sqrt{dt} , where dt is the incremental time step. For these simulations, the dt was 0.001 s. The initial conditions for the simulations were $x = 1.00$, $y = -1.00$, and $\omega = \pi$.

The results of these 500 Euler-Maruyama simulations are shown in Figs. 3.1, 3.2, and 3.3. In the top portion of Figs. 3.1 and 3.2, it may be seen that the average amplitude of the limit cycle is decreasing as the noise amplitude is increasing. The average amplitude of x , $\langle x \rangle$, decreases less quickly than the average amplitude of $\langle y \rangle$. This behavior may be seen in the limit cycle, which is presented in Fig. 3.4. In the top portion of Fig. 3.3, it may be seen that the average frequency, $\langle \omega \rangle$, is enhanced by a small amount of noise: the average frequency quickly learns the forcing frequency without overshoot. However, as the amplitude of the noise increases, $\langle \omega \rangle$ starts to converge to a value that is not equal to the forcing frequency. For large amplitudes of noise, $\langle \omega \rangle$ tends to zero. Additionally, the variance for ω starts to increase as the noise amplitude is increased.

3.3 Fokker-Planck Equation and Moment Equations

In this section, the full Fokker-Planck equation for the Hopf AFO is derived. The Fokker-Planck equation is a partial differential equation (PDE), which is a function of the states and of time. The solution of the Fokker-Planck equation is a probability density distribution. The Fokker-Planck equation can be written as [151, 152]:

$$\partial_t P = -\partial_j [A_j(\vec{v}, t)P] + \frac{1}{2} \sum_{j,k} \partial_j \partial_k [B(\vec{v}, t)B^T(\vec{v}, t)]_{j,k} P \quad (3.4)$$

Here, \vec{v} is a vector containing all state variables, x , y , and ω . $P = P(\vec{v}, t)$ is the time evolution of the probability density, $A_j(\vec{v}, t)$ is a vector that includes the deterministic parts of Eq. 3.4, and $B_j(\vec{v}, t)$ is a vector that contains the stochastic parts of Eq. 3.4. The Fokker-Planck

equation of the Hopf AFO can be written as:

$$\begin{aligned}
\partial_t P = & -\partial_x((\mu x - x^3 - x y^2 - \omega y + k_x f(t))P) \\
& -\partial_y((\mu y - x^2 y - y^3 + \omega x)P) \\
& +\partial_\omega((k_\omega f(t))P) \\
& +\frac{\sigma^2}{2}(\partial_x^2(P k_x^2) - 2\partial_x \partial_\omega(y P k_x k_\omega) \\
& +\partial_\omega^2(y^2 P k_\omega^2))
\end{aligned} \tag{3.5}$$

Here, $f(t) = a \sin(\Omega t)$. The Fokker-Planck equation may be solved with several different methods, such as the stochastic averaging method [153, 154], the finite element method [155, 156], and Gaussian closure methods [157, 158, 159]. It should also be noted that the Fokker-Planck equation, in general, does not have an analytical solution.

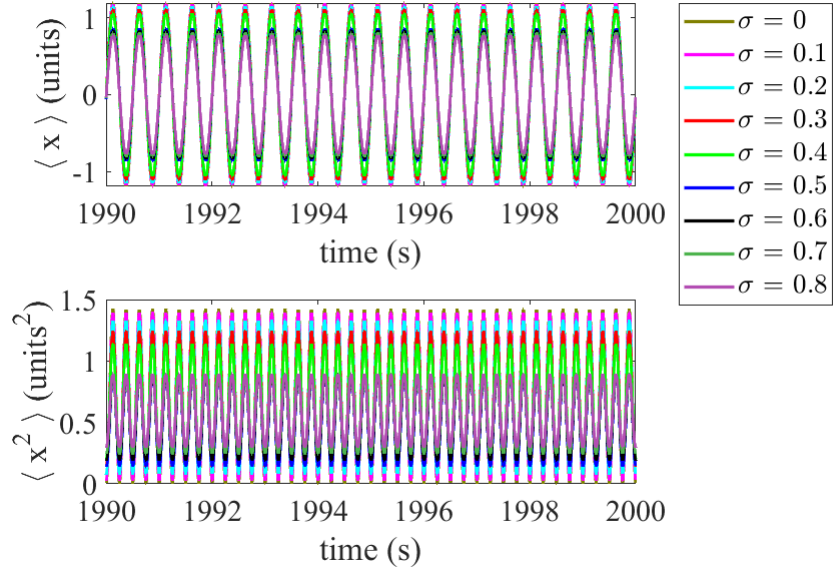


Figure 3.5: **Fokker-Planck results: x state.** Mean and variance of x obtained from moment equations. As the noise amplitude is increased, $\langle x \rangle$ decreases.

To find a semi-analytical solution of the Fokker-Planck equation, the cumulant neglect

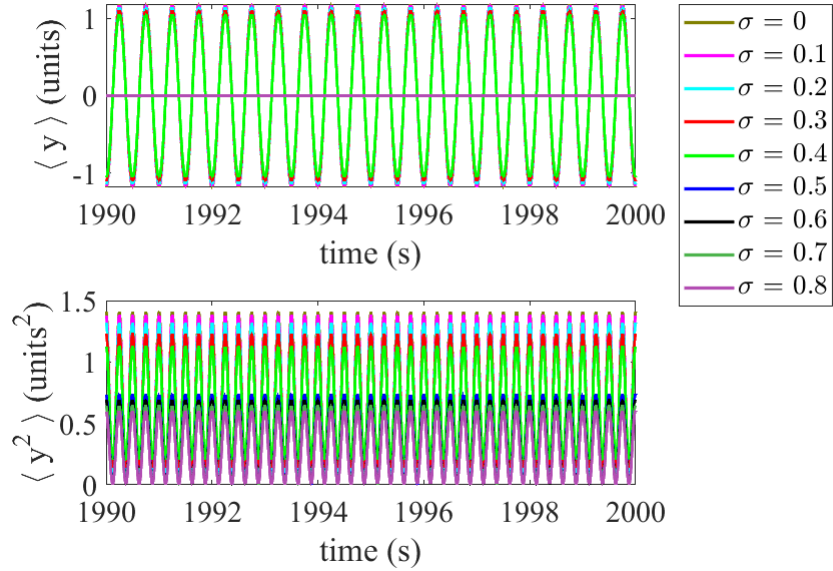


Figure 3.6: **Fokker-Planck results: y state.** Mean and variance of y obtained from moment equations. As the noise amplitude is increased, $\langle y \rangle$ decreases, eventually collapsing the limit cycle into one dimensional oscillations.

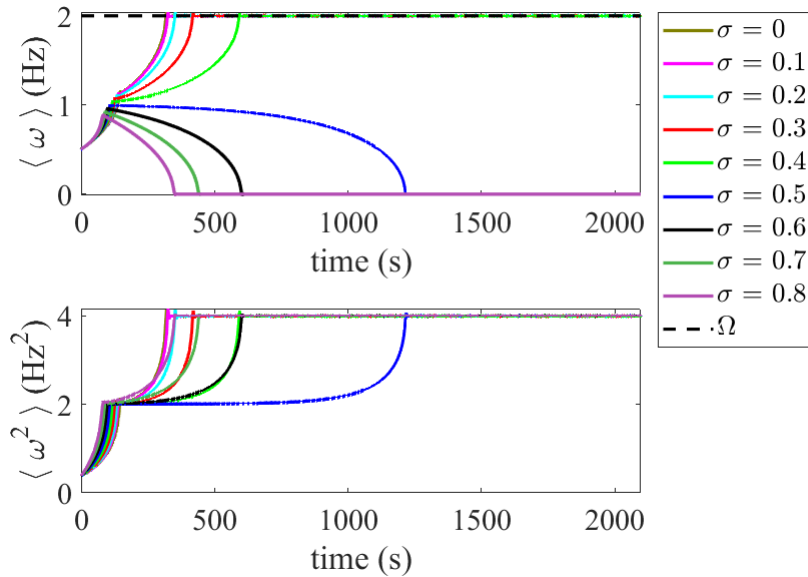


Figure 3.7: **Fokker-Planck results: ω state.** Mean and variance of ω obtained from moment equations. As the noise amplitude is increased, the $\langle \omega \rangle$ value converges to the incorrect value.

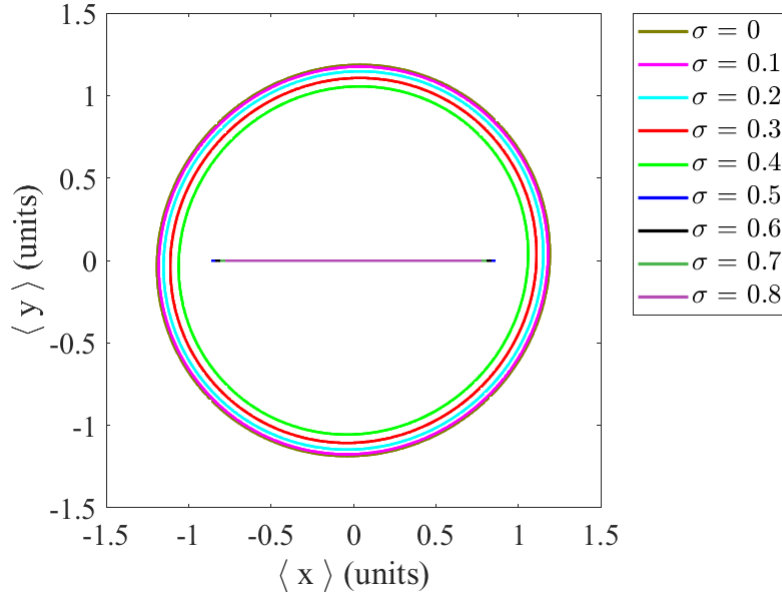


Figure 3.8: **Fokker-Planck results: limit cycles.** For the moment equations, the limit cycle of $\langle x \rangle$ vs. $\langle y \rangle$ is shown. As the noise level increases, the two dimensional limit cycle begins to collapse into one dimensional oscillations.

method [147] will be used to approximate the probability density function that is the time-varying solution of Eq. 3.5. This truncation method works well in practice [160]. To find the moment equations, the moment evolution equation is first constructed. To this end, the moment is defined as: $\langle g \rangle = \iiint g P dx dy d\omega$. Next, the time derivative of each side of the equation may be written as: $\frac{d\langle g \rangle}{dt} = \iiint g \frac{dP}{dt} dx dy d\omega$. Now, g may be replaced with the i^{th} moment of x , the j^{th} moment of y , and the k^{th} moment of ω . This produces: $\frac{d\langle x^i y^j \omega^k \rangle}{dt} = \iiint x^i y^j \omega^k \frac{dP}{dt} dx dy d\omega$. After substitution and rearrangements, the moment evolution equation for the Hopf AFO can now be written as:

$$\begin{aligned}
\frac{d\langle x^i y^j \omega^k \rangle}{dt} = & \mu i \langle x^i y^j \omega^k \rangle - i \langle x^{i+2} y^j \omega^k \rangle - i \langle x^i y^{j+2} \omega^k \rangle \\
& - i \langle x^{i-1} y^{j+1} \omega^{k+1} \rangle + i f(t) k_x \langle x^{i-1} y^j \omega^k \rangle \\
& + \mu j \langle x^i y^j \omega^k \rangle - j \langle x^{i+2} y^j \omega^k \rangle - j \langle x^i y^{j+2} \omega^k \rangle \\
& + j \langle x^{i+1} y^{j-1} \omega^{k+1} \rangle - k_\omega f(t) k \langle x^i y^{j+1} \omega^{k-1} \rangle \\
& + k_x \frac{\sigma_x^2}{2} i(i-1) \langle x^{i-2} y^j \omega^k \rangle + \\
& \frac{\sigma_\omega^2}{2} k_\omega^2 k(k-1) \langle x^i y^{j+2} \omega^{k-2} \rangle \\
& - \sigma^2 k_\omega k_x k i \langle x^{i-1} y^{j+1} \omega^{k-1} \rangle
\end{aligned} \tag{3.6}$$

By substituting different values of i , j , and k , this moment evolution equation will lead to an infinite set of ordinary differential equations (ODEs). In order to truncate this infinite set of ODEs, the cumulants of order 3 and higher are set equal to zero [147].

Noting that states are not considered to be independent (i.e., $\langle x^r y^s \omega^k \rangle \neq \langle x^r \rangle \langle y^s \rangle \langle \omega^k \rangle$), the cumulant neglect method yields the following set of 9 ODEs:

$$\begin{aligned}
\dot{z}_1 &= k_x f(t) + 2z_1^3 - 2z_2 z_5 + z_1(\mu + 2z_2^2) \\
&\quad + z_1(-3z_4 - z_7) - z_8 \\
\dot{z}_2 &= 2z_2^3 - 2z_1 z_5 + z_6 + z_2(\mu + 2z_1^2 - z_4 - 3z_7) \\
\dot{z}_3 &= -k_\omega f(t) z_2 \\
\dot{z}_4 &= k_x^2 \sigma^2 + 4z_1^4 + 4z_1^2 z_2^2 - 2z_5(z_3 + 2z_5) \\
&\quad - 2z_2 z_6 - 2z_4(-\mu + 3z_4 + z_7) \\
&\quad + 2z_1(k_x f(t) + 2z_2 z_3 - z_8) \\
\dot{z}_5 &= 4z_1 z_2^3 + 2z_2^2 z_3 + 2z_1 z_6 + z_3(-2z_1^2 + z_4 - z_7) \\
&\quad + 2z_5(\mu - 3(z_4 + z_7)) + z_2(k_x f(t) + 4z_1^3 - 2z_8) \\
\dot{z}_6 &= 2z_2 z_3^2 + z_6(\mu - 3z_4 - z_7) \\
&\quad + z_3(k_x f(t) + 2z_1(z_1^2 + z_2^2) - 2z_8) \\
&\quad - z_5(k_\omega f(t) + 2z_8) - z_2(k_\omega k_x \sigma^2 + z_9) \\
\dot{z}_7 &= 2(2z_1^2 z_2^2 + 2z_2^4 + (z_3 - 2z_5)z_5 + z_2 z_6) \\
&\quad + (\mu - z_4 - 3z_7)z_7 + z_1(-2z_2 z_3 + z_8) \\
\dot{z}_8 &= -2z_1 z_3^2 - 2z_5 z_6 + 2z_3(z_1^2 z_2 + z_2^3 + z_6) \\
&\quad - k_\omega f(t) z_7 + (\mu - z_4 - 3z_7)z_8 + z_1 z_9 \\
\dot{z}_9 &= k_\omega^2 \sigma^2 z_7 - 2k_\omega f(t) z_8
\end{aligned} \tag{3.7}$$

These nine ordinary differential equations are used to approximate the solution of the Fokker-Planck equation. Each of these equations corresponds to a particular time-dependent moment, where $z_n = z_n(t)$. Table 3.1 lists the moments and their corresponding equation of motion.

In [147], it was noted that the cumulant neglect method typically outperforms the moment neglect method. This is likely because the cumulant neglect method preserves relationships between the moments. However, unlike other expansions (e.g., Taylor expansion, etc.), there is no guarantee that including additional higher order terms will decrease

Table 3.1: List of moments and their respective moment equation.

Description	Moment	State
Mean of x	$\langle x \rangle$	z_1
Mean of y	$\langle y \rangle$	z_2
Mean of ω	$\langle \omega \rangle$	z_3
Variance of x	$\langle x^2 \rangle$	z_4
Covariance of x & y	$\langle xy \rangle$	z_5
Covariance of x & ω	$\langle x\omega \rangle$	z_6
Variance of y	$\langle y^2 \rangle$	z_7
Covariance of y & ω	$\langle y\omega \rangle$	z_8
Variance of ω	$\langle \omega^2 \rangle$	z_9

the error of the solution [160]. This is an intrinsic difficulty with the Fokker-Planck equation, which, to the authors' knowledge, has not been solved. Instead, the qualitatively similar results of the cumulant neglect equations, the Euler-Maruyama simulations, and the experimental results suggest that the cumulant neglect method as applied here is valid.

Numerically solving Eq. 3.7 generates the results shown in Figs. 3.5, 3.6, and 3.7. Here, k_x , k_ω , μ , and Ω are set to the same values that were used in Section 3.2. The initial conditions are set as: $z_1(0) = 1$, $z_2(0) = -1$, $z_3(0) = \pi$, $z_4(0) = 15$, $z_5(0) = 0$, $z_6(0) = 0$, $z_7(0) = 15$, $z_8(0) = 0$, $z_9(0) = 15$.

The mean of x shown in Fig. 3.5 and the mean of y shown in Fig. 3.6 both show similar behavior as found in the simulations and experiments. As the amplitude of the noise increases, the limit cycle amplitude decreases. As in the simulations and experiments, the decrease in the amplitude of $\langle y \rangle$ is much faster than the decrease of $\langle x \rangle$. For large amounts of noise, the two dimensional limit cycle of the averaged dynamics collapses into one dimensional oscillations, which may be seen in Fig. 3.8. The variances of x and y

behave somewhat differently for large amplitudes of noises, as compared to the simulations and experiments. In general, the variances found from the moment equations have more oscillatory motion than the variances found from the simulations and experiments. In Fig. 3.7, $\langle \omega \rangle$ shows qualitatively similar behavior as found in the Euler-Maruyama simulations and the experiments. For small amplitudes of noise, $\langle \omega \rangle$ converges to the correct frequency value; for medium and large noise levels, $\langle \omega \rangle$ converges to the incorrect forcing frequency. These results, however, do not show the behavior of $\langle \omega \rangle$ converging to an incorrect, non-zero quantity at medium noise amplitudes that is seen in the simulations and experiments. The variance of ω shares the some tendency as that of other two methods: as the noise amplitudes increase, the variance is also increased.

3.4 Analog Circuit Experiment

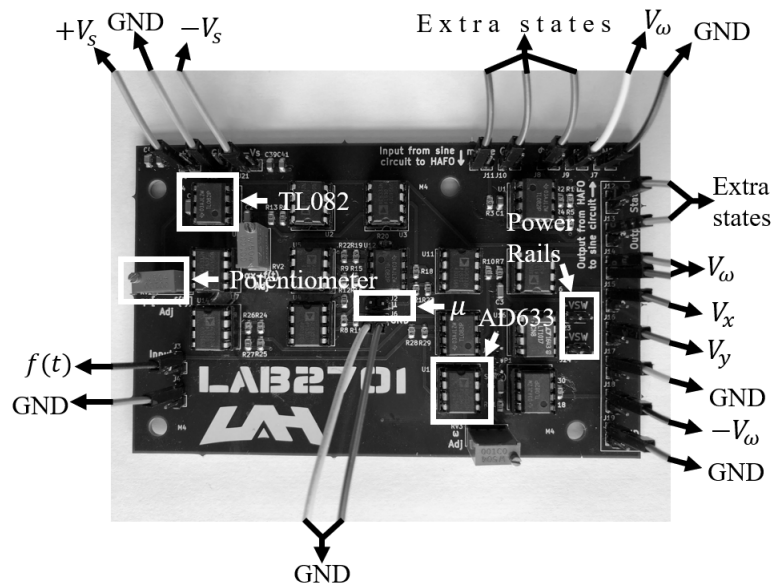


Figure 3.9: **Circuit experiment.** The printed circuit board that was used for the experiments. Here, $f(t) = a \sin(\Omega t) + \sigma \dot{W}(t)$.

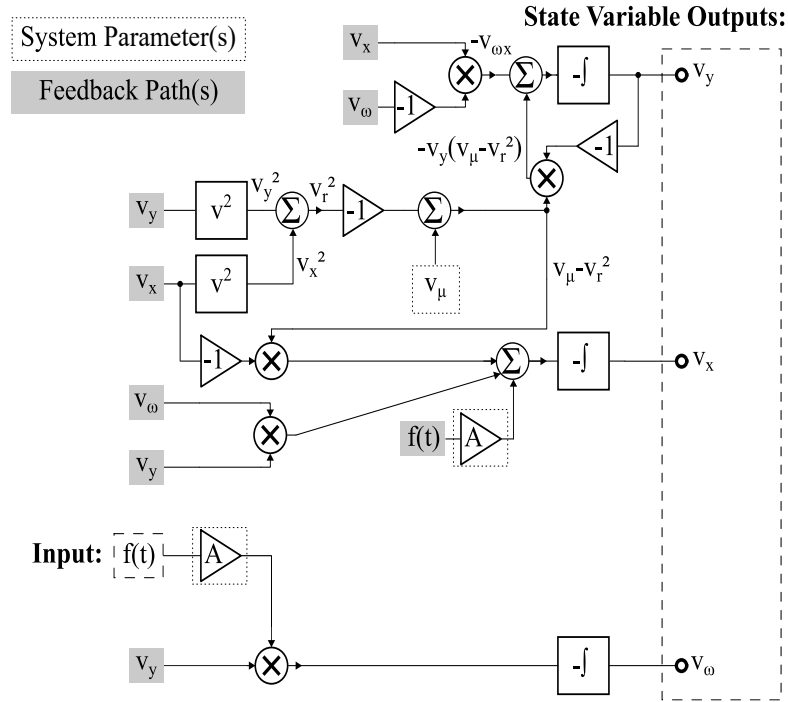


Figure 3.10: **Circuit schematic.** A simplified schematic for the Hopf AFO circuit, with states V_x , V_y , and V_ω .

A physical analog circuit implementation of Eq. 3.2 was designed, fabricated, and tested. The experimental printed circuit board (PCB) is shown in Fig. 3.9. Here, two potentiometers are used to vary the coupling strength of the external stimuli in both x and ω . This circuit implementation is accomplished by using AD633 multipliers, TL082 operational amplifiers, and 0805 SMD resistors; resistors have an error tolerance of 1%, and capacitors have an error tolerance of 2%. For the experiments reported here, $V_\mu = 10$ volts, and the external excitation (e.g., $a \sin(\Omega t) + \sigma \dot{W}(t)$) was created in MATLAB and sent to the circuit using a National Instrument (NI) cDAQ-9174, which also collected the x , y , and ω states' data. A sampling rate of 20000 samples/sec was used for all experiments.

A simplified schematic for the circuit depicted in Fig. 3.9 is shown in Fig. 3.10.

By applying Kirchhoff's laws to the voltage-mode operational amplifier integrator config-

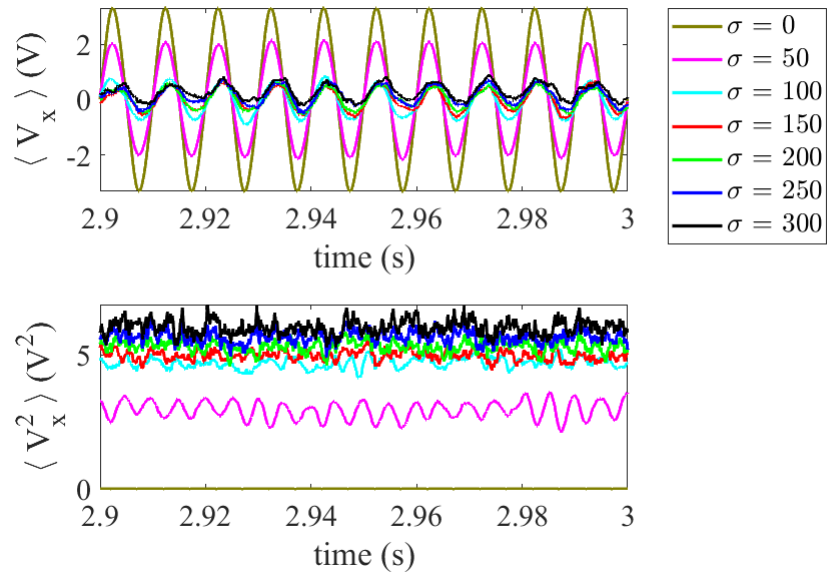


Figure 3.11: **Experimental results: x state.** Mean and variance of x obtained from the experiments. As the noise amplitude is increased, $\langle x \rangle$ decreases.

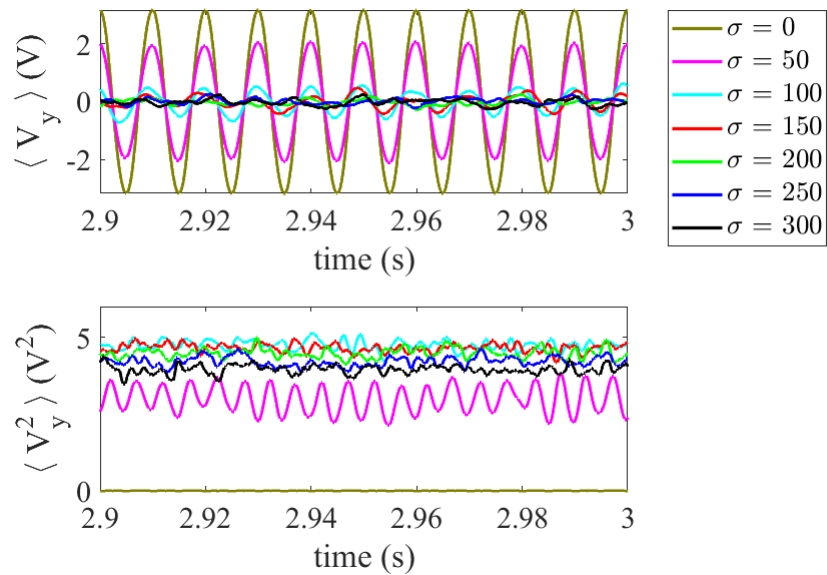


Figure 3.12: **Experimental results: y state.** Mean and variance of y obtained from the experiments. As the noise amplitude is increased, $\langle y \rangle$ decreases.

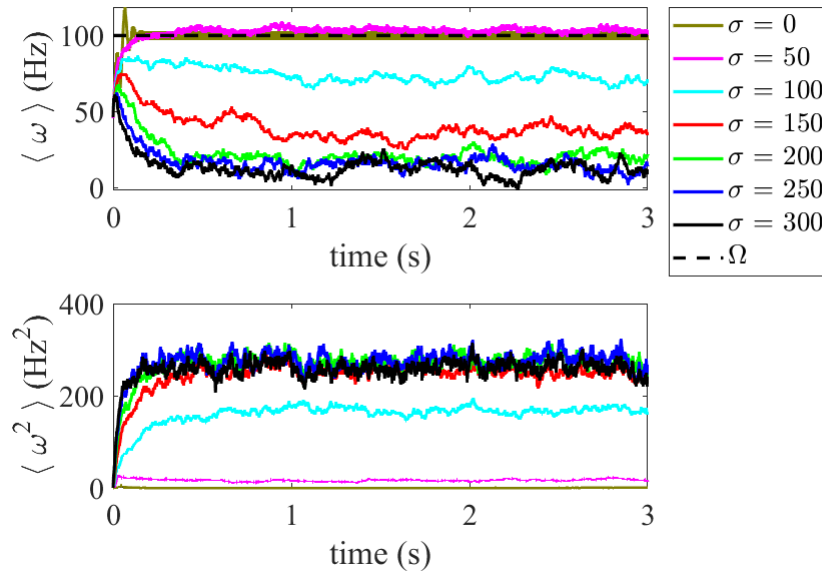


Figure 3.13: **Experimental results: ω state.** Mean and variance of ω obtained from the experiments. It should be noted that V_ω was converted to ω to compare the results to the forcing frequency, Ω . As the noise amplitude is increased, $\langle \omega \rangle$ converges to the incorrect value.

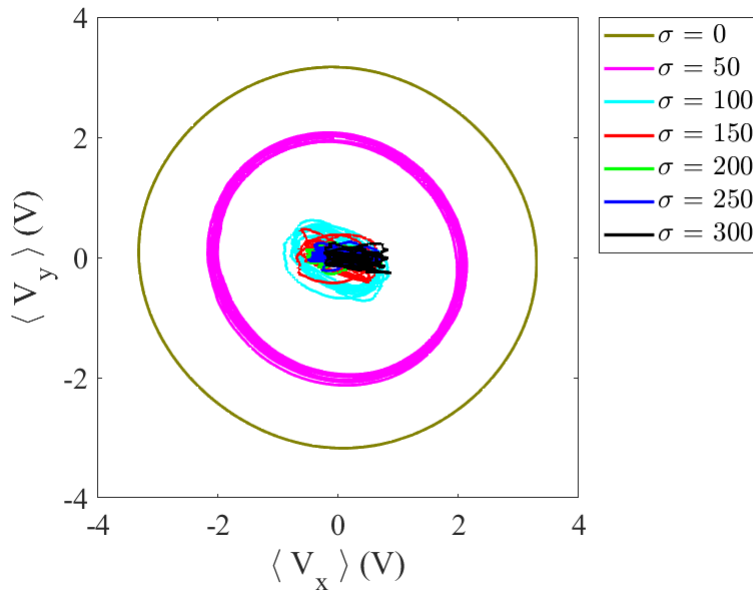


Figure 3.14: **Experimental results: limit cycles.** For the experiment, the limit cycle of $\langle x \rangle$ vs. $\langle y \rangle$ is shown. As the noise level increases, the two dimensional limit cycle begins to collapse into one dimensional oscillations.

urations equipped with voltage multipliers, this circuit is able to reconstruct the dynamical system represented by Eq. 3.2. Here, $V_f(t) = a \sin(\Omega t) + \sigma \dot{W}(t)$. It should be noted that this circuit has a modular design, which enables it to be used as a two-state Hopf oscillator, a three-state Hopf AFO, and a four-state adaptive Hopf oscillator. The extra states shown on Fig. 3.9 refer to this additional functionality. By connecting V_α to ground, the four-state adaptive Hopf oscillator becomes a three-state Hopf AFO as described by Eq. 3.1. This equations that describe this circuit are written as follows:

$$\begin{aligned}
\dot{V}_x &= -\frac{1}{R_1 C_1} (V_\mu - (V_x^2 + V_y^2)) V_x + \frac{1}{R_2 C_1} V_\omega V_y \\
&\quad - \frac{1}{P_1 C_1} V_f(t) \\
\dot{V}_y &= -\frac{1}{R_3 C_2} (V_\mu - (V_x^2 + V_y^2)) V_y - \frac{1}{R_4 C_2} V_\omega V_x \\
\dot{V}_\omega &= \frac{1}{P_2 C_3} V_f(t) V_y
\end{aligned} \tag{3.8}$$

Here, the three states, V_x , V_y , V_ω , correspond to the voltage outputs of the operational amplifier integrators. R_1 through R_4 are resistors (each with a value of $10\text{k}\Omega$), C_1 through C_3 are capacitors (each with a value of $0.1\mu\text{F}$), and P_1 and P_2 are potentiometers (with $P_1 = 1.78\text{k}\Omega$ and $P_2 = 0.88\text{k}\Omega$).

Experiments were performed with the same method as followed for the numerical simulations: 500 experiments were performed for each different noise amplitude. For each of these batches of experiments, the time-varying mean and variance were calculated. The results of these experiments are shown in Figs. 3.11, 3.12, and 3.13. Each of these shows good qualitative agreement with the numerical and analytical results. Similar to the numerical and analytical results, the amplitude of the oscillations of the mean of x and y both decrease, as the noise amplitude is increased. For large amplitudes of noise, the amplitude of $\langle y \rangle$ becomes smaller than $\langle x \rangle$, and the two dimensional limit cycle collapses to one dimensional oscillations, which may be seen in the limit cycles that are plotted in Fig. 3.14. In Fig. 3.13, the mean of ω converges to the correct value more quickly with

small amounts of noise. For medium amplitudes of noise, the mean of ω converges to an incorrect, non-zero value. As the amplitude of the noise increases further, the mean of ω begins to converge to zero.

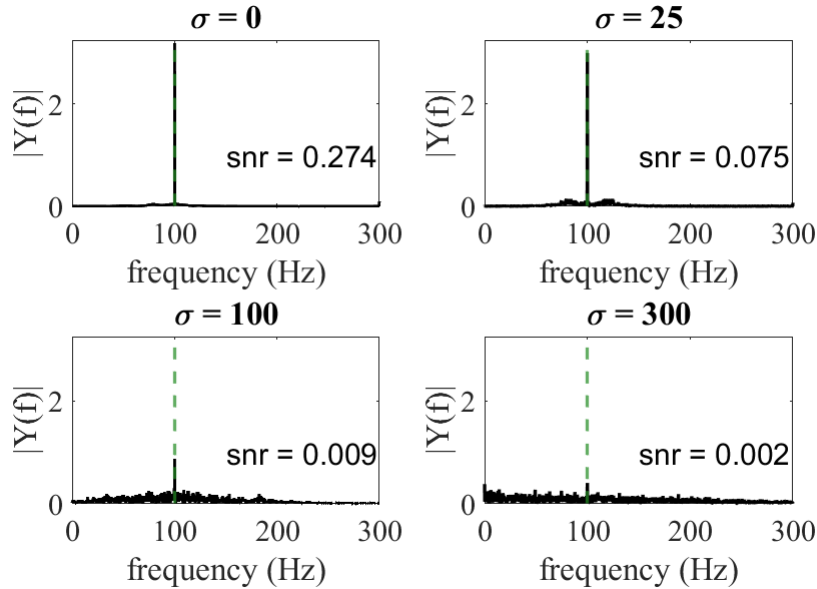


Figure 3.15: **Unaveraged results.** For several noise amplitudes, the single-sided amplitude spectrum of the unaveraged x state is shown. Without averaging, it can be seen that the signal content is attenuated, which is a nonlinear effect. The signal-to-noise ratio decreases for larger amplitudes of noise because of both the addition of noise and the attenuation of signal present in the x state.

A comment should also be made concerning the unaveraged system. For the unaveraged x state, noise has the effect of attenuating the oscillator's signal content, which may be seen in Fig. 3.15. Even though the same amplitude of the deterministic component was used, the x state does not properly lock onto the sinusoidal signal in the presence of noise. This causes the signal-to-noise ratio to decrease, while the addition of noise causes the signal-to-noise ratio to decrease even further.

3.5 Concluding remarks

Adaptive oscillators may be used for many physical applications, including phase-locked loops in electronic systems, synchronous lasers, information storage and signal processing in quantum systems, and energy harvesting in mechanical systems. Since all real-world systems have sources of noise, it is important to quantify the stochastic effects of adaptive oscillators. In this chapter, the stochastic dynamics of a Hopf AFO are studied through numerical, analytical, and experimental methods, in order to gain a better understanding of how noise affects adaptive oscillators. Batches of Euler-Maruyama simulations were used to find ensemble averages that capture the dynamics of the stochastic Hopf AFO. Next, the full Fokker-Planck equation was derived for this system, and the cumulant neglect method was used to find a truncated set of ordinary differential equations that approximate the solution for the full Fokker-Planck equation. An analog circuit was designed that behaves as a Hopf AFO, and this circuit was fabricated as a PCB. Experiments using this PCB showed qualitatively similar results to both the numerical and analytical approaches.

Several general observations may be made from these studies. 1) Small amplitudes of noise enhance the learning of the Hopf AFO; the $\langle \omega \rangle$ state converges to the forcing frequency with less overshoot. 2) For medium amplitudes of noise, the $\langle \omega \rangle$ state converges to an incorrect, non-zero value. (It should be noted that this behavior was seen for the numerical and experimental results, but it was not observed in the analytical results.) 3) For large amplitudes of noise, the $\langle \omega \rangle$ state tends to zero. 4) The limit cycle's amplitude (i.e., $\sqrt{\langle x \rangle^2 + \langle y \rangle^2}$) decreases as the noise amplitude increases. 5) Moreover, $\langle y \rangle$ decreases at a faster rate than $\langle x \rangle$, as the noise amplitude increases. Considering the averaged dynamics, this causes the two dimensional limit cycle to collapse into one dimensional oscillations for large amplitudes of noise.

It should also be noted that the results found in this chapter differ from the results

reported in [29]. In [29], an assumption was made to simplify the Fokker-Planck equation to be a function of only ω . However, the x and y states affect the dynamics of the full Fokker-Planck equation. Namely, the limit cycle's shape changes, which also affects the learned frequency. Since the equation for $\dot{\omega}$ is a frequency mixer using state y , $\langle y \rangle$ converging to zero prevents the Hopf AFO from adapting to the correct frequency. The methods used in this chapter could be used to construct adaptive oscillators that have enhanced dynamics in the presence of noise.

CHAPTER

4

THE PENDULUM ADAPTIVE FREQUENCY OSCILLATOR

Limit cycle oscillators, such as the Hopf oscillator or the van der Pol oscillator, have been often used as the base for adaptive oscillators. To the author's knowledge, a pendulum has not been previously used as the base of an adaptive oscillator. Here, a mechanical pendulum adaptive oscillator is described and experimentally tested. The length of the pendulum's rod is used to store the frequency of the external force. This system could be used as a smart energy harvesting system. In Section 4.1, the equations of motion of the pendulum adaptive frequency oscillator are described. Numerical results are presented

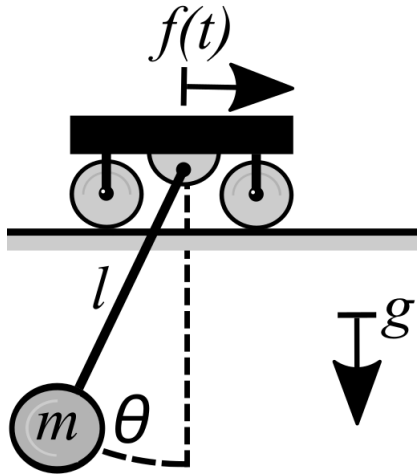


Figure 4.1: **Pendulum with horizontal forcing.** It should be noted that the cart is kinematically constrained to the forcing function, $f(t)$.

in Section 4.2. Next, the experimental pendulum adaptive frequency oscillator setup is discussed in Section 4.3. The experimental results are shown in Section 4.4.

4.1 Equations of Motion

The horizontally forced pendulum is depicted in Fig. 4.1. The kinetic energy (eq. 4.1) and potential energy (eq. 4.2) for this system may be written as:

$$T = \frac{1}{2} m (l \dot{\theta})^2 = \frac{1}{2} m l^2 \dot{\theta}^2 \quad (4.1)$$

$$V = mgh = mg(l - l \cos(\theta)) \quad (4.2)$$

The massless cart is kinematically constrained to move with a particular forcing function, $f(t)$. This force and its location may be written as:

$$\vec{f}(t) = f(t)\vec{i} \quad (4.3)$$

$$\vec{r} = l \sin(\theta)\vec{i} + l \cos(\theta)\vec{j} \quad (4.4)$$

The generalized force may thus be written as:

$$Q_\theta(t) = \vec{f}(t) \cdot \frac{\partial \vec{r}}{\partial \theta} = l \cos(\theta) f(t) \quad (4.5)$$

Assuming a Rayleigh dissipation function, $D = \frac{1}{2} c m l^2 \dot{\theta}^2$, Lagrange's equation can be used to find the equation of motion for the system as:

$$m l^2 \ddot{\theta} + c m l^2 \dot{\theta} + m g l \sin(\theta) = l \cos(\theta) f(t) \quad (4.6)$$

By dividing by $m l^2$, the equation of motion can be written as:

$$\ddot{\theta} + c \dot{\theta} + \omega_n^2 \sin(\theta) = \frac{1}{m l} \cos(\theta) (\hat{a} \cos(\Omega t)) \quad (4.7)$$

Here, \hat{a} is the forcing amplitude. Using $x = \theta$ and $y = \dot{\theta}$, eq. 4.7 may be written in state space as follows:

$$\begin{aligned} \dot{x}(t) &= y(t) \\ \dot{y}(t) &= -c y(t) - \omega_n^2 \sin(x(t)) + A \cos(x(t)) \cos(\Omega t) \end{aligned} \quad (4.8)$$

In eq. 4.8, $A = \frac{\hat{a}}{m l}$. Now, an additional dynamic state, which adapts the natural frequency of the system to the forcing frequency, may be added:

$$\begin{aligned}
\dot{x}(t) &= y(t) \\
\dot{y}(t) &= -c y(t) - \omega^2(t) \sin(x(t)) + A \cos(x(t)) \cos(\Omega t) \\
\dot{\omega}(t) &= \frac{-A \cos(\Omega t) x(t)}{\sqrt{x^2(t) + y^2(t)}}
\end{aligned} \tag{4.9}$$

As the linear natural frequency of the pendulum in Fig. 4.1 is given by $\omega_n = \sqrt{\frac{g}{l}}$, the $\omega(t)$ state may be realized in an experiment by controlling the length of the pendulum, l . The $\dot{\omega}$ equation is similar to the frequency adaption state used for the Hopf adaptive frequency oscillator used in [1, 100, 101], although the y state in the numerator must be substituted for the x state.

4.2 Numerical Results

The set of eqs. 4.8 and the set of eqs. 4.9 were both simulated in MATLAB using *ode45*. The frequency response of several non-adaptive pendulums (eq. 4.8) with various static natural frequencies are shown in Figs. 4.2 and 4.3, along with the frequency learned and stored by the ω state.

In Fig. 4.2, the forcing amplitude was a small value ($A = 0.552$). In this case, the pendulum responds as a linear oscillator. For this reason, the ω state learns the forcing frequency, Ω , with high accuracy, as can be seen in the right portion of Fig. 4.2. The dashed line is the “perfect” case, in which $\omega = \Omega$.

In Fig. 4.3, the forcing amplitude was a larger value ($A = 5.52$). In this case, the pendulum responds as a softening Duffing oscillator. The pendulum’s frequency response has a discontinuity, which is caused by multiple solutions of the analytical frequency response function given by eq. 4.29. Even though the pendulum’s oscillations are nonlinear, the pendulum adaptive frequency oscillator still finds the maximal value of each of the non-adaptive pendulum’s frequency amplitude response. However, for the non-adaptive

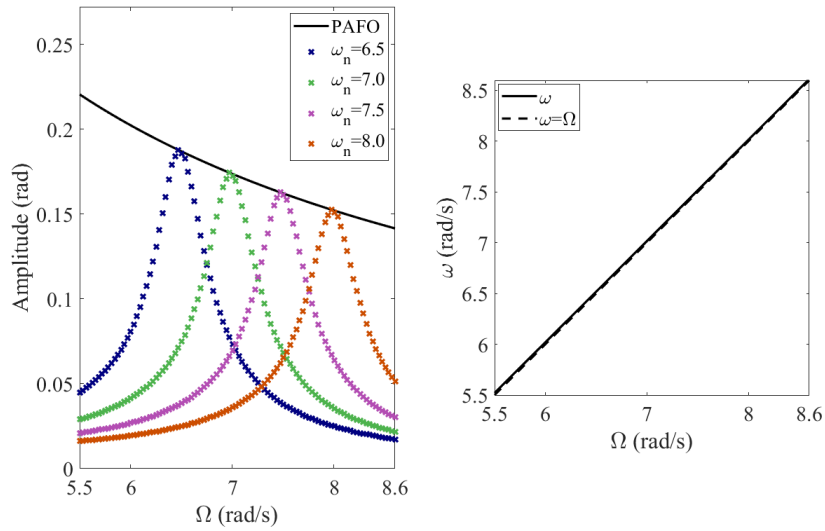


Figure 4.2: **Numerical results of pendulum adaptive frequency oscillator for small oscillations.** For small oscillations, the pendulum acts as a linear oscillator. Left: The frequency response of the pendulum adaptive frequency oscillator is compared with the frequency response of the non-adaptive pendulum, for several values of ω_n . For this simulation, $c = 0.45$ and $A = 0.552$. Notice that the pendulum adaptive oscillator has the same amplitude as the non-adaptive pendulum only when the non-adaptive pendulum's amplitude is at a maximum. Right: The ω state learns the external forcing with high accuracy.

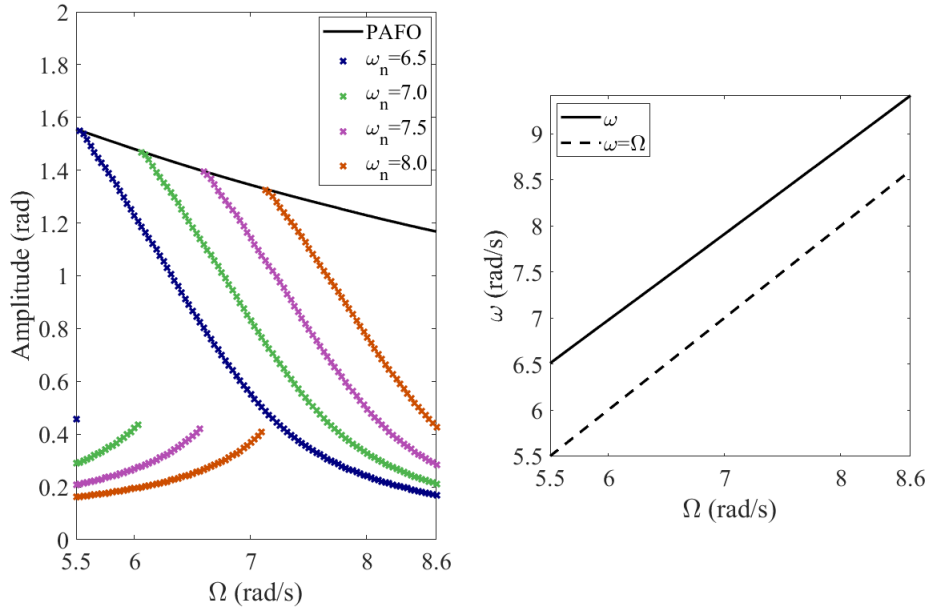


Figure 4.3: **Numerical results of pendulum adaptive frequency oscillator for large oscillations.** For large oscillations, the pendulum acts as a softening Duffing oscillator. Left: The frequency response of the pendulum adaptive frequency oscillator is compared with the frequency response of the non-adaptive pendulum, for several values of ω_n . For this simulation, $c = 0.45$ and $A = 5.52$, which can be compared with Fig. 4.9. Notice that the pendulum adaptive oscillator has the same amplitude as the non-adaptive pendulum only when the non-adaptive pendulum's amplitude is at a maximum. Right: The ω state has an offset above the external forcing frequency. This is caused by the hysteresis in the frequency amplitude response, as will be discussed in Subsection 4.3.2.

pendulum, the peak no longer occurs at the natural frequency, but it instead occurs at a value below the natural frequency, which is discussed in Subsection 4.3.2. This causes the ω state to learn a value that is higher than the forcing frequency; this offset causes the pendulum adaptive frequency oscillator to respond with an amplitude that is the maximum of the non-adaptive pendulum's frequency amplitude response.

4.3 Experimental Setup

In this section, the experimental prototype of the pendulum adaptive frequency oscillator is described. This mechanical prototype is described by the set of eqs. (4.9), with the third equation describing the dynamics of the frequency adaptation. This third equation is realized in the mechanical prototype by first approximating the linear natural frequency of the pendulum, which is discussed in Subsection 4.3.1; the pendulum's rod length dynamically responds to learn the linear natural frequency. However, the pendulum has a nonlinear response at large forcing amplitudes. To account for this, the method of multiple scales is used to find the analytical solution of the pendulum in Subsection 4.3.2, and it is shown that the pendulum responds as a Duffing oscillator. The hysteresis associated with the Duffing oscillator explains the offset present in the learning process when the forcing amplitude is large. This analytical response is also used to find the experimental parameters in Subsection 4.3.3. Next, the experimental results of the mechanical pendulum adaptive frequency oscillator are shown in Subsection 4.3.4.

The experimental setup is shown in Fig. 4.4. For this prototype, a stepper motor is used to modify the length of the pendulum. To reduce the weight actuated by the stepper motor and to increase the range of frequencies that can be learned for the experimental pendulum, a metronome-inspired pendulum setup was designed. The angular displacement is measured by an encoder. The stepper motor rotates a pinion, which linearly moves the

rack; the rack's weight changes the effective rod length of the pendulum. The pendulum's cart is attached to a linear bearing, and this cart is kinematically oscillated with a linkage that is driven by a motor (unpictured). The forcing signal from this linkage is collected via a laser displacement sensor.

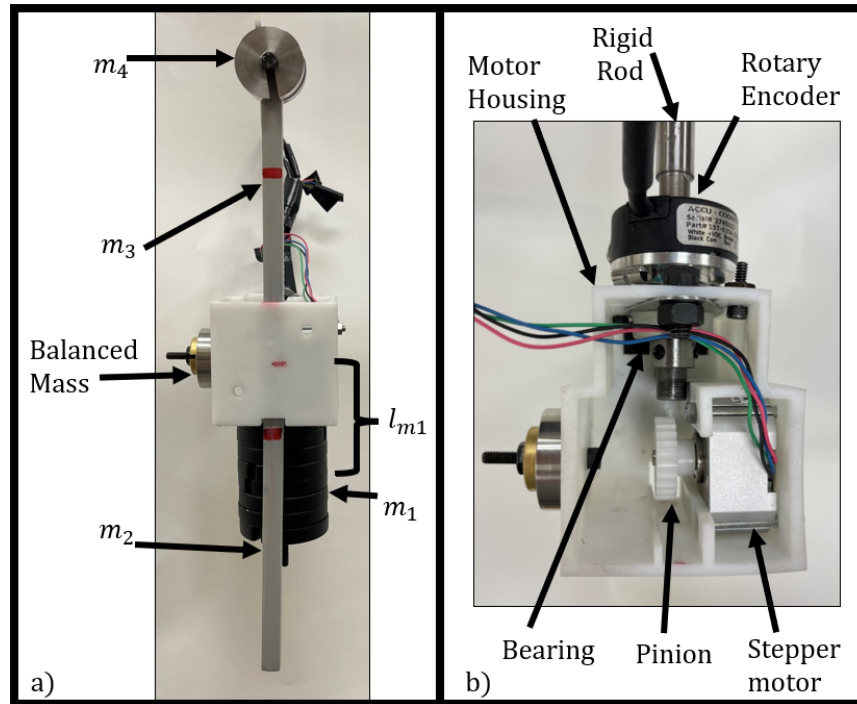


Figure 4.4: **Experimental pendulum adaptive frequency oscillator.** The experimental pendulum adaptive frequency oscillator prototype. a) Side view: The balanced mass offsets the mass of the stepper motor. The masses and lengths can be compared to those labeled in the drawing, which is depicted in Fig. 4.5. b) Top view: The white motor housing is made 3D printed using Formlabs' Rigid resin. The rotary encoder measures the angular displacement of the pendulum. The stepper motor rotates a pinion, which moves the rack, modifies the pendulum's rod length. The rigid rod is connected to the cart.

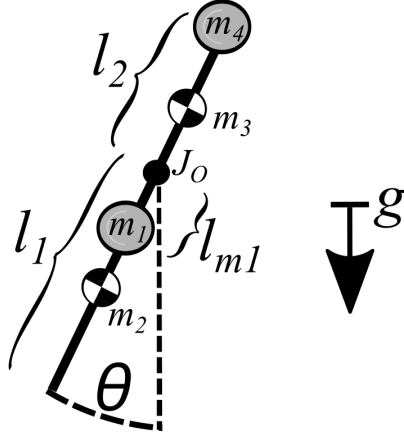


Figure 4.5: **Schematic for the experimental pendulum adaptive frequency oscillator prototype.** This pendulum setup, similar to a metronome, allows a smaller amount of mass, $m_{rack} + m_4$, to be actuated with the stepper motor. The system rotates about the black dot. m_1 is the mass of an unmovable weight, which is offset by an amount l_{m1} from the rotation point. m_2 is the mass of the lower portion of the rack, which has a length of l_1 . m_3 is the mass of the upper portion of the rack, which has a length of l_2 . m_4 is the mass at the top of the rack. This pendulum setup, similar to a metronome, allows a smaller mass, m_4 to be actuated with the stepper motor.

4.3.1 Linear Natural Frequency Approximation

In this subsection, the linear natural frequency is derived for the experimental setup, when it is undergoing small oscillations. Some of the parameters for the experiment are measured directly, while some are calculated with a curve fit in the next subsection. Using the schematic shown in Fig. 4.5, the kinetic and potential energy of the experimental system can be found. All of these quantities are measured and provided in Table 4.1, except for the quantity J_0 .

The kinetic energy for the pendulum adaptive frequency oscillator is:

$$T = \frac{1}{2} \left(m_1 l_{m1}^2 + m_2 \frac{l_1^2}{4} + m_3 \frac{l_2^2}{4} + m_4 l_2^2 + J_0 \right) \dot{\theta}^2 \quad (4.10)$$

The potential energy for the pendulum adaptive frequency oscillator is:

Table 4.1: Parameters for the experiment, which are directly measured.

Parameter	Value	Units
l	0.3175	m
l_1	$l - l_2$	m
l_2	$l - l_1$	m
l_{m1}	0.075	m
m_{rack}	0.036	kg
m_1	0.8	kg
m_2	$\frac{l_1}{l} m_{rack}$	kg
m_3	$\frac{l_2}{l} m_{rack}$	kg
m_4	0.11	kg

$$\begin{aligned}
 V = & m_1 g (l_{m1} - l_{m1} \cos(\theta)) + m_2 g \left(\frac{l_1}{2} - \frac{l_1}{2} \cos(\theta) \right) \\
 & + m_3 g \left(\frac{l_2}{2} - \frac{l_2}{2} \cos(\theta + \pi) \right) + m_4 g (l_2 - l_2 \cos(\theta + \pi))
 \end{aligned} \tag{4.11}$$

Using a Taylor expansion, eq. 4.11 simplifies to:

$$\begin{aligned}
 V \approx & \frac{1}{2} (m_1 g l_{m1} + m_2 g \frac{l_1}{2} - m_3 g \frac{l_2}{2} - m_4 g l_2) \theta^2 \\
 & + m_3 g l_2 + 2m_4 g l_2
 \end{aligned} \tag{4.12}$$

Using the Lagrange's equation, the experimental setup's equivalent mass, equivalent stiffness, and linear natural frequency are:

$$\begin{aligned}
 m_{eq} &= m_1 l_{m1}^2 + m_2 \frac{l_1^2}{4} + m_3 \frac{l_2^2}{4} + m_4 l_2^2 + J_O \\
 k_{eq} &= m_1 g l_{m1} + m_2 g \frac{l_1}{2} - m_3 g \frac{l_2}{2} - m_4 g l_2 \\
 \omega_n &= \sqrt{\frac{m_1 g l_{m1} + m_2 g \frac{l_1}{2} - m_3 g \frac{l_2}{2} - m_4 g l_2}{m_1 l_{m1}^2 + m_2 \frac{l_1^2}{4} + m_3 \frac{l_2^2}{4} + m_4 l_2^2 + J_O}}
 \end{aligned} \tag{4.13}$$

This last equation provides the relationship between the rod length and the natural

frequency, which will be utilized in Subsection 4.3.4. All of these quantities in eq. 4.13 are known, except for the J_0 . This term is affected by the rotational inertia of the bearing, motor housing, and encoder. It will be approximated in Subsection 4.3.3.

4.3.2 Method of Multiple Scales

In this subsection, the method of multiple scales is used to find the nonlinear frequency response of the pendulum undergoing large oscillations, such as that used in [140]. Using this nonlinear frequency response to curve fit the experimental data, the remaining experimental parameters will be found in Subsection 4.3.3.

Expanding $\sin(\theta)$ and $\cos(\theta)$ in a Taylor series and discarding the higher-order (≥ 2) terms while defining $\frac{\hat{a}}{ml} = A$, then eq. 4.7 now becomes:

$$\ddot{\theta} + c\dot{\theta} + \omega_n^2\theta - \frac{\omega_n^2\theta^3}{6} = A\left(1 - \frac{\theta^2}{2}\right)\cos(\Omega t) \quad (4.14)$$

It should be noted that, when written in the form shown in eq. 4.14, the nonlinear pendulum is a Duffing equation, with a softening nonlinear stiffness term. Introducing a book keeping term, ϵ , into eq. 4.14, similar to the one used in [161], such that $\theta = \sqrt{\epsilon}\hat{\theta}$, $A = \epsilon\sqrt{\epsilon}\hat{A}$ and $c = \epsilon\hat{c}$. Making these substitutions into eq. (4.14):

$$\sqrt{\epsilon}\ddot{\hat{\theta}} + \epsilon\hat{c}\sqrt{\epsilon}\dot{\hat{\theta}} + \omega_n^2\sqrt{\epsilon}\hat{\theta} - \frac{\omega_n^2\epsilon\sqrt{\epsilon}\hat{\theta}^3}{6} = \epsilon\sqrt{\epsilon}\hat{A}\left(1 - \frac{\epsilon\hat{\theta}^2}{2}\right)\cos(\Omega t) \quad (4.15)$$

Dividing this equation by $\sqrt{\epsilon}$, the following expression is obtained:

$$\ddot{\hat{\theta}} + \epsilon\hat{c}\hat{\theta} + \omega_n^2\hat{\theta} - \frac{\epsilon\omega_n^2\hat{\theta}^3}{6} = \hat{A}\cos(\Omega t)\left(\epsilon - \frac{\epsilon^2\hat{\theta}^2}{2}\right) \quad (4.16)$$

The general solution is assumed to be of the following form:

$$\hat{\theta} = \theta_0 + \epsilon \theta_1 \quad (4.17)$$

Several time scales, T_0, T_1, T_2, \dots are introduced, where $T_0 = t, T_1 = \epsilon t, T_2 = \epsilon^2 t, \dots$. Thus, $\hat{\theta}$ is a function of the slow and fast time scales, and $\hat{\theta}(t, \epsilon) = \theta_0(T_0, T_1, T_2, \dots) + \epsilon \theta_1(T_0, T_1, T_2, \dots) + \epsilon^2 \theta_2(T_0, T_1, T_2, \dots) + \dots$. Using the chain rule, the time derivatives become $\frac{d}{dt} = D_0 + \epsilon D_1 + \epsilon^2 D_2$, $\frac{d^2}{dt^2} = D_0^2 + 2\epsilon D_0 D_1 + \epsilon^2 (D_1^2 + 2D_0 D_2) + \dots$. The general solution and the time derivatives are substituted back into eq. 4.16, and, by gathering together the terms with the same powers of ϵ and equating to zero, the following set of differential equations is obtained:

$$\epsilon^0: D_0^2 \theta_0 + \omega_n^2 \theta_0 = 0 \quad (4.18)$$

$$\epsilon^1: D_0^2 \theta_1 + \omega_n^2 \theta_1 = -\hat{c} D_0 \theta_0 - 2D_0 D_1 \theta_0 + \hat{A} \cos(\Omega t) + \frac{\omega_n^2 \theta_0^3}{6} \quad (4.19)$$

The solution of eq. 4.18 can be written as:

$$\theta_0 = \alpha \cos(\beta + T_0) \quad (4.20)$$

or in complex form as:

$$\theta_0 = B e^{iT_0} + \bar{B} e^{-iT_0} \quad (4.21)$$

where $\alpha = \alpha(T_1), \beta = \beta(T_1), B = B(T_1), \bar{B} = \bar{B}(T_1)$, and \bar{B} is the complex conjugate of B . B and \bar{B} can be expressed in their polar forms, shown as following:

$$B = \frac{1}{2} \alpha e^{i\beta} \quad (4.22)$$

$$\bar{B} = \frac{1}{2} \alpha e^{-i\beta}$$

Substitute eq. 4.22 into eq. 4.19 results in the following expressions:

$$\begin{aligned}
D_0^2 \theta_1 + \omega_n^2 \theta_1 = & 2i\omega_n \left(-\frac{1}{2} \hat{c} B e^{iT_0 \omega_n} + \frac{1}{2} \hat{c} \bar{B} e^{-iT_0 \omega_n} - e^{iT_0 \omega_n} D_1 B + e^{-iT_0 \omega_n} D_1 \bar{B} \right) \\
& + \frac{1}{2} \left(B^2 \omega_n^2 \bar{B} e^{iT_0 \omega_n} + \bar{B}^2 \omega_n^2 B e^{-iT_0 \omega_n} + \hat{A} e^{-iT_0 \Omega} + \hat{A} e^{iT_0 \Omega} \right) \\
& + \frac{\omega_n^2}{6} \left(B^3 e^{3iT_0 \omega_n} + \bar{B}^3 e^{-3iT_0 \omega_n} \right)
\end{aligned} \tag{4.23}$$

where $\frac{1}{2}(\hat{A}e^{-iT_0\Omega} + \hat{A}e^{iT_0\Omega})$ in the above equation is the complex form of the external forcing.

Assuming that $\Omega = \omega_n + \epsilon\sigma$ and $T_1 = T_0\epsilon$, the resulting equation is given by:

$$\begin{aligned}
D_0^2 \theta_1 + \omega_n^2 \theta_1 = & 2i\omega_n \left(-\frac{1}{2} \hat{c} B e^{iT_0 \omega_n} + \frac{1}{2} \hat{c} \bar{B} e^{-iT_0 \omega_n} - e^{iT_0 \omega_n} D_1 B + e^{-iT_0 \omega_n} D_1 \bar{B} \right) \\
& + \frac{1}{2} \left(B^2 \omega_n^2 \bar{B} e^{iT_0 \omega_n} + \bar{B}^2 \omega_n^2 B e^{-iT_0 \omega_n} \right) \\
& + \frac{1}{2} \left(\hat{A} e^{-iT_0 \omega_n + iT_1 \sigma} + \hat{A} e^{iT_0 \omega_n + iT_1 \sigma} \right) \\
& + \frac{1}{6} \left(\omega_n^2 B^3 e^{i3T_0 \omega_n} - \omega_n^2 \bar{B}^3 e^{-i3T_0 \omega_n} \right)
\end{aligned} \tag{4.24}$$

Equating the secular terms to zero, the following equation is obtained:

$$-i\hat{c}\omega_n B - 2i\omega_n D_1 B + \frac{1}{2} \left(B^2 \bar{B} \omega_n^2 + \hat{A} e^{iT_1 \sigma} \right) = 0 \tag{4.25}$$

Substituting the polar form of B and $e^{i\beta} = \cos(\beta) + i \sin(\beta)$ into eq. 4.25, the solvability condition can be expressed as:

$$\begin{aligned}
0 = & \frac{i}{2} \hat{c} \omega_n \alpha - i\omega_n D_1 \alpha + \omega_n \alpha D_1 \beta + \frac{\alpha^3 \omega_n^2}{16} \\
& + \frac{1}{2} \left(\hat{A} \cos(T_1 \sigma - \beta) + i \hat{A} \sin(T_1 \sigma - \beta) \right)
\end{aligned} \tag{4.26}$$

Eq. 4.26 can be separated into two different equations, which represent the real and imaginary parts, respectively. This can then be rearranged to obtain the following expressions for $D_1 \alpha$ and $D_1 \beta$:

$$D_1\alpha = \frac{1}{2}c\alpha + \frac{\hat{A}\sin(T_1\sigma - \beta)}{2\omega_n} \quad (4.27)$$

$$D_1\beta = -\frac{\alpha^2\omega_n}{16} - \frac{\hat{A}\cos(T_1\sigma - \beta)}{2\omega_n\alpha}$$

For $\gamma = T_1\sigma - \beta$, $D_1\gamma = \sigma - D_1\beta$. Thus, eq. 4.27 becomes:

$$D_1\alpha = \frac{1}{2}c\alpha + \frac{\hat{A}\sin(\gamma)}{2\omega_n} \quad (4.28)$$

$$D_1\gamma = \frac{\alpha^2\omega_n}{16} + \frac{\hat{A}\cos(\gamma)}{2\omega_n\alpha} + \sigma$$

The system represented by eq. 4.28 is a planar autonomous dynamical system. Setting $\epsilon = 1$, solving the fixed point (α_0, γ_0) solution, and rearranging the equation by using $\sin^2\gamma + \cos^2\gamma = 1$ provides the frequency response function:

$$(c\omega_n)^2 + \left(\frac{\alpha_0^3\omega_n^2}{8} + 2\sigma\alpha_0\omega_n\right)^2 = A^2 \quad (4.29)$$

The frequency response function in eq. 4.29 is plotted in Fig. 4.6. In the next subsection, this frequency response function will be used to approximate several of the remaining experimental parameters. Eq. 4.29 has multiple roots; in Fig. 4.6, the stable roots are plotted for different values of Ω . A hysteresis region may be seen, in which there are two stable roots for a single value of Ω . There is an unstable root between these two stable roots, which is not shown.

4.3.3 Experimental Parameters

Since this system is nonlinear, a curve fitting procedure was necessary to calculate the values of c and J_0 , as these values cannot be directly measured in the experiment. By using the analytical frequency response curve found in eq. (4.29), the rotational inertia, J_0 ,

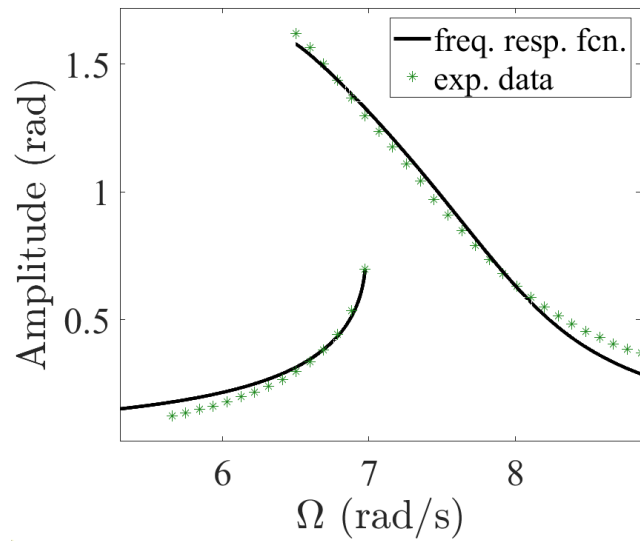


Figure 4.6: **Duffing-like response of pendulum.** For a non-adaptive pendulum with rod length set to $l_1 = 16.5$ cm, a frequency upsweep and downsweep was performed with the experiment; the green markers are the prototype's amplitude response. This data was then used in a curve fit of eq. 4.29. The resulting frequency response function is plotted as a black curve. It should be noted that eq. 4.29 has multiple roots, and some frequencies have two stable amplitude responses.

Table 4.2: Curve fit results when $l_1 = 16.5$ cm.

Parameter	Value	Units
c	0.45	s^{-1}
A	5.52	cm
ω_n	7.67	rad/s
J_0	1.47×10^{-4}	$kg\ m^2$

damping parameter, c , horizontal forcing amplitude, A , and a static linear natural frequency, ω_n , are calculated from a curve fit. It should be noted that the forcing amplitude is also included in this curve fit because the laser displacement data is noisy. For comparison, the amplitude from the laser sensor of the forcing amplitude is approximately 5.69 cm, which is 3% different than the curve fitted result. A forcing frequency upsweep and downsweep, ranging from 5.5 (rad/s) to 9 (rad/s), was performed on the non-adaptive pendulum with a fixed rod length, such that $l_1 = 16.5$ cm. This data is plotted as green asterisks in Fig. 4.6. This data was then used to curve fit the frequency response function given by the roots of eq. 4.29 using MATLAB's *lsqcurvefit*. The resulting analytical frequency response curve is shown in Fig. 4.6. The parameters obtained from the curve fit are listed in Table 4.2. The natural frequency of this non-adaptive pendulum is calculated as $\omega_n = 7.67$ (rad/s) from the curve fit. This value can then be substituted into eq. 4.13 to find the J_0 value, which is calculated as $J_0 = 1.47 \times 10^{-4}$ ($kg\ m^2$).

Using the value of J_0 that is found from the curve fit, the relationship between the system's natural frequency and the hanging length, l_1 , can be derived using eq. 4.13. This relationship between is depicted in Fig. 4.7. A portion of this curve has a linear relationship, for lengths ranging from approximately $6 < l_1 < 24$. This linear relationship (as found from a curve fit), $\omega_n(l_1) = 0.28l_1 + 3.003$, is used to control the stepper motor. This line is plotted

as a green curve in Fig. 4.7.

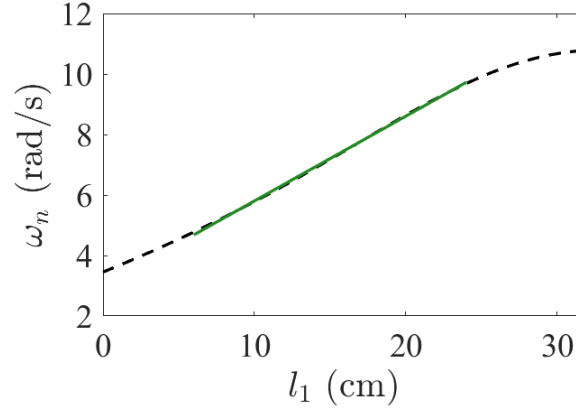


Figure 4.7: **Relationship between rack length and linear natural frequency.** The relationship between the lower rack length, l_1 , and the pendulum's linear natural frequency is depicted as a dashed, black curve. A portion of this range is quite linear, which is depicted as a green, solid curve.

4.3.4 Experimental Implementation of Frequency Adaptation

The ω state given by eq. 4.9 is implemented as follows. The laser displacement sensor measures the position of the periodic forcing of the experiment, while the encoder measures the angular position of the pendulum. The angular velocity is calculated by taking the numerical derivative (e.g., $y(i) = \frac{x(i)-x(i-1)}{\Delta t}$, for a sampling rate of $\frac{1}{\Delta t}$). By using Euler's method, the ω state described in eq. 4.9 can be re-written as:

$$\omega(i+1) = \omega(i) - \frac{k f(i) x(i)}{\sqrt{x^2(i) + y^2(i)}} \Delta t \quad (4.30)$$

In eq. 4.30, i is an integer that corresponds to the i^{th} sample in time. It should be noted that the time series does not need to be recorded, except for the previous angular displacement that is needed to calculate $y(i)$. k is an arbitrary coupling constant that is

set to 0.6 in the experimental results of the next section, $f(i)$ is the sensor measurement at time step i , $x(i)$ is the angular displacement at time step i , and $y(i)$ is the angular velocity at time step i . This ω state is used to calculate an incremental change in the rod length, Δl_1 , by using the linear relationship shown in Fig. 4.7 ($l_1 = 3.57\omega_n - 10.71$):

$$\Delta l_1 = (3.57\omega(i+1) - 10.71) - (3.57\omega(i) - 10.71) \quad (4.31)$$

The stepper motor controls the length of the rod. The experimental sensor data collection, the calculation of eqs. 4.30 and 4.31, and the control signal sent to the stepper motor are performed with an Arduino. It is worth noting that no filtering was used for any of the experimentally collected data.

4.4 Experimental Results

The pendulum adaptive frequency oscillator prototype was fabricated and tested. For a particular forcing frequency ($\Omega = 7.1$ rad/s), an example of a particular time history is shown in Fig. 4.8. In this time history, the ω state starts far away from the forcing frequency, so the amplitudes of the x and y states are small. As the ω nears the forcing frequency, the amplitudes of the x and y states becomes large.

A forcing frequency sweep ranging from 5.5 rad/s to 8.6 rad/s was used to measure the performance of the pendulum adaptive frequency oscillator prototype. The results are depicted in Fig. 4.9. In this range, the ω state learns the forcing frequency with a percent error that is less than 5%, where the percent error is calculated as $\frac{(\omega) - \Omega}{\Omega} \times 100\%$ after the experiment has settled to a steady state response. Since the pendulum's oscillations were fairly large, the prototype has a Duffing-like response. This causes the ω state to have a positive offset as compared to the Ω value, which is similar to that seen in Fig. 4.3.

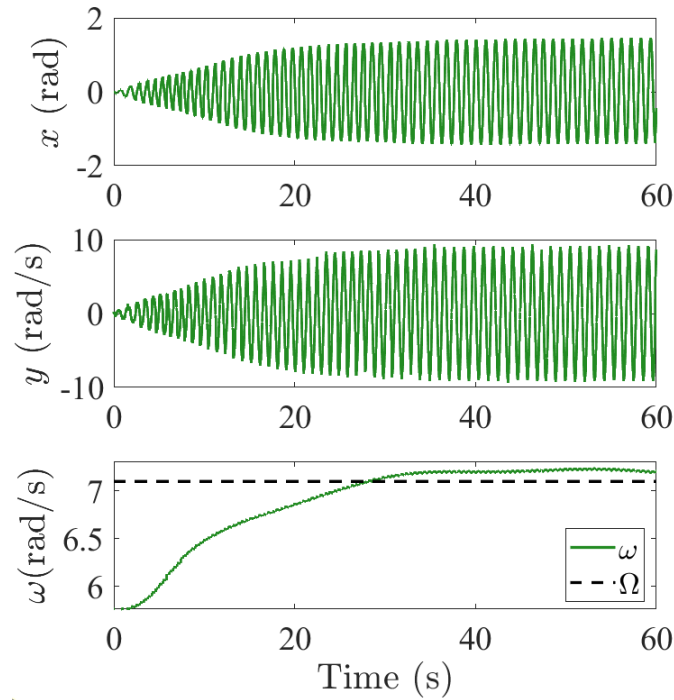


Figure 4.8: **The time history of the pendulum adaptive frequency oscillator.** The external forcing frequency was $\Omega = 7.1$ rad/s. The amplitude of the x and y states increase when the ω state has learned the resonance frequency.

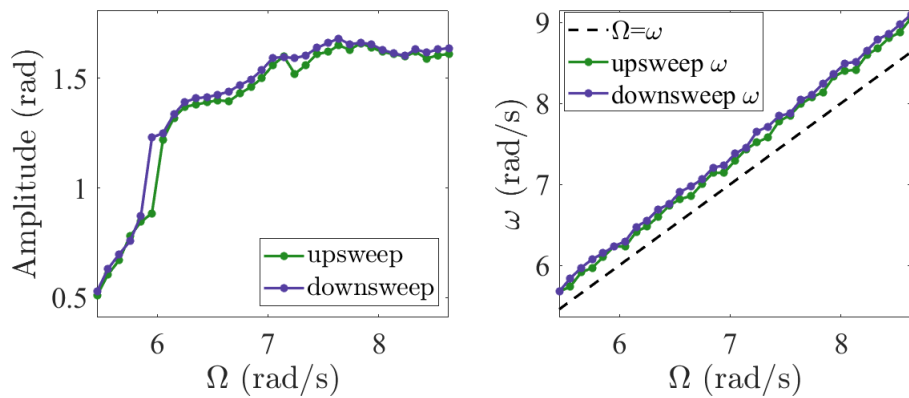


Figure 4.9: **Experimental results of pendulum adaptive frequency oscillator for large oscillations.** A forcing frequency sweep ranging from 5.5 rad/s to 8.6 rad/s was performed on the pendulum adaptive frequency oscillator prototype. The average of the ω state's steady state value is plotted for each forcing frequency, Ω . The line $\omega = \Omega$ is plotted for reference. The pendulum adaptive frequency oscillator learns the input frequency with high accuracy. Since the amplitude of the pendulum adaptive frequency oscillator is large, there is a positive offset of the ω state, as was seen in Fig. 4.3.

Comparing the frequency response obtained from the simulation (Figs. 4.2 and 4.3) and the experiment (Fig. 4.9), it can be seen that the ω state responds in a qualitatively similar way in both the simulations and the experiments. However, the experiment of the pendulum adaptive frequency oscillator's amplitude falls considerably at approximately 6 rad/s, which is robust in the frequency sweep in the up and down directions. The authors believe that this effect is caused by a combination of the Duffing oscillator's hysteresis phenomenon and nonlinear damping in the experiment (e.g., wire effects, damping associated with the encoder, etc.).

4.5 Conclusions

To the author's knowledge, this is the first time that a pendulum adaptive frequency oscillator has been proposed, fabricated, and tested. This system not only works in the linear regime, but it also has increased amplitudes for the nonlinear regime. At large amplitudes, the plastic frequency state converges to a value above the forcing frequency; this causes the pendulum to respond with the maximal amplitude of the non-adaptive pendulum. In this setup, no filtering was used for any of the experimental data collection. Other than the controller for the stepper motor, no control algorithms or signal processing techniques (such as fast Fourier transforms) are involved; the learning process is accomplished solely with the dynamical system itself. This pendulum adaptive frequency oscillator prototype can respond over a relatively large range of frequencies. Since vibratory energy harvesters are most efficient when the external vibrations aligns with a resonance, this pendulum adaptive frequency oscillator could be a viable architecture for a smart energy harvester.

CHAPTER

5

CHAOS IN A PENDULUM ADAPTIVE FREQUENCY OSCILLATOR

Building on presented in the previous chapter in which a mechanical pendulum adaptive frequency oscillator was studied, the current paper studies a pendulum adaptive frequency oscillator circuit experiment that can exhibit chaotic motion. Both the bifurcation diagrams from numerical simulations and from the experiments are compared. Although most papers report either simulated or experimental bifurcation diagrams, some work has compared simulated bifurcation diagrams with experimental bifurcation diagrams directly, such as a circuit implementation of the Rössler system [162], an analog system realization of

Table 5.1: List of parameters and states.

Symbol	Description
a	Forcing amplitude
k_ω	Coupling in ω state
c	Damping
l	Pendulum length
m	Mass
g	Acceleration due to gravity
Ω	External sinusoidal forcing frequency
θ	Angular position of pendulum
$\dot{\theta}$	Angular velocity of pendulum
$x(t)$	Angular position in state space
$y(t)$	Angular velocity in state space
$\omega(t)$	Adaptive frequency

a time-delay chaotic oscillator [163], a Chua's circuit [164], and a physical circuit realization of a four-dimensional chaotic system [165]. This paper is organized as follows. In Section 5.1, the derivation of the equation of motion of the 2-state pendulum and 3-state pendulum adaptive frequency oscillator is discussed. In Section 5.2, results from numerical simulations are shown, including the behavior of the system for low amplitude forcing and the numerical bifurcation diagram. In Section 5.3, the pendulum adaptive frequency oscillator circuit implementation for a field-programmable analog array is described. In Section 5.4, results from the experiment are shown. In Section 5.5, some concluding remarks are summarized.

5.1 Equation of Motion of Horizontally Forced Pendulum AFO

In Fig. 5.1, the horizontally forced pendulum is depicted. In this pendulum, it is assumed that the rod is inelastic, and the horizontal forcing kinematically moves the pivot point. For

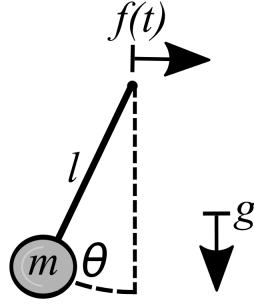


Figure 5.1: **Pendulum with horizontal forcing.** It should be noted that $f(t)$ kinematically moves the pivot point.

reference, the constants and states are listed in Table 5.1. By using Lagrange's equations and assuming a Rayleigh dissipation of the form $\frac{1}{2} c m l^2 \dot{\theta}^2$, the governing equation can be written as follows:

$$m l^2 \ddot{\theta} + c m l^2 \dot{\theta} + m g l \sin(\theta) = l \cos(\theta) f(t) \quad (5.1)$$

After dividing both sides of the equation by $m l^2$, eq. 5.1 becomes:

$$\ddot{\theta} + c \dot{\theta} + \omega_n^2 \sin(\theta) = \frac{1}{m l} \cos(\theta) f(t) \quad (5.2)$$

Converting eq. 5.2 into state space with $x = \theta$ and $y = \dot{\theta}$, the following set of ordinary differential equations may be written:

$$\begin{aligned} \dot{x}(t) &= y(t) \\ \dot{y}(t) &= -c y(t) - \omega_n^2 \sin(x(t)) + \frac{1}{m l} \cos(x(t)) f(t) \end{aligned} \quad (5.3)$$

Setting $f(t) = \hat{a} \sin(\Omega t)$ with $\hat{a} = a m l$, eq. 5.3 can be written as:

$$\begin{aligned} \dot{x}(t) &= y(t) \\ \dot{y}(t) &= -c y(t) - \omega_n^2 \sin(x(t)) + a \cos(x(t)) \sin(\Omega t) \end{aligned} \quad (5.4)$$

Here, a is the amplitude of the sinusoidal forcing. Using these pendulum equations as a base oscillator, a pendulum adaptive frequency oscillator can be constructed by adding a plastic, dynamic state that can learn the external forcing frequency:

$$\begin{aligned}
 \dot{x}(t) &= y(t) \\
 \dot{y}(t) &= -c y(t) - \omega^2(t) \sin(x(t)) + a \cos(x(t)) \sin(\Omega t) \\
 \dot{\omega}(t) &= \frac{-k_\omega x(t) a \sin(\Omega t)}{\sqrt{x^2(t) + y^2(t)}}
 \end{aligned} \tag{5.5}$$

Here, k_ω is the coupling strength in the third state.

5.2 Simulation Results

For most values of the forcing frequency, Ω , the pendulum adaptive frequency oscillator behaves as expected: the frequency state converges to the forcing frequency. This behavior is depicted in Fig. 5.2. For this figure and for the subsequent bifurcation diagrams, a quasi-static frequency sweep was performed, for both the numerical simulations and the experiments. In Figs. 5.2 and 5.3, *ode45* in MATLAB was used to simulate eq. 5.5 for 400 periods of the forcing function, $\sin(\Omega t)$. Only the last 100 cycles were used to create Figs. 5.2 and 5.3, to avoid any transient behavior. Stroboscopic sections were taken of the pendulum's dynamics, using the external sinusoid as the clock with frequency Ω .

In Fig. 5.2, the pendulum adaptive frequency oscillator's stroboscopic sections show that the ω state has properly learned the external forcing frequency, Ω . Since the x and y states are periodic with the same frequency as the external sinusoid, their stroboscopic sections appear stationary with respect to this clock.

Repeating this same procedure that was used for Fig. 5.2, the bifurcation diagram is constructed, which is depicted in Fig. 5.3. For this set of parameters, the pendulum adaptive frequency oscillator does not properly learn the external forcing frequency. Instead, the

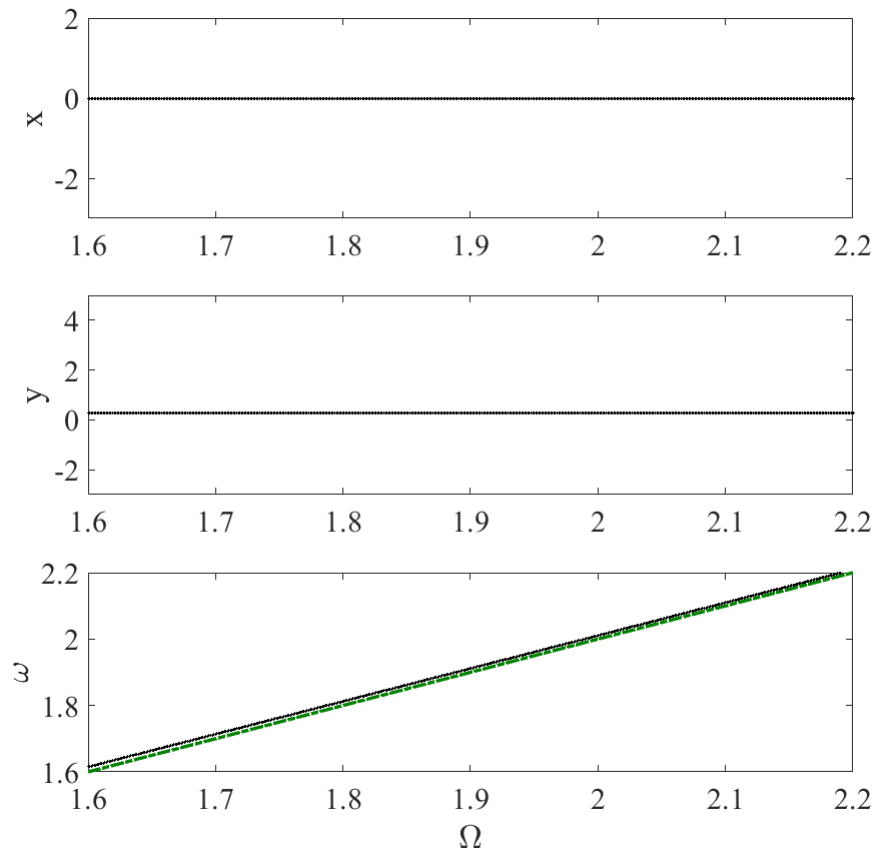


Figure 5.2: **Periodic stroboscopic sections from numerical simulations.** Stroboscopic sections of the states of the horizontally forced pendulum adaptive frequency oscillator for Ω ranging from 1.6 rad/s to 2.2 rad/s. Here, $a = 0.1$, $c = 0.35$, and $k_\omega = 0.707$. The green dashed line represents the line $\omega = \Omega$. For this combination of parameters, the pendulum adaptive frequency oscillator correctly learns the external forcing frequency.

system has a chaotic response.

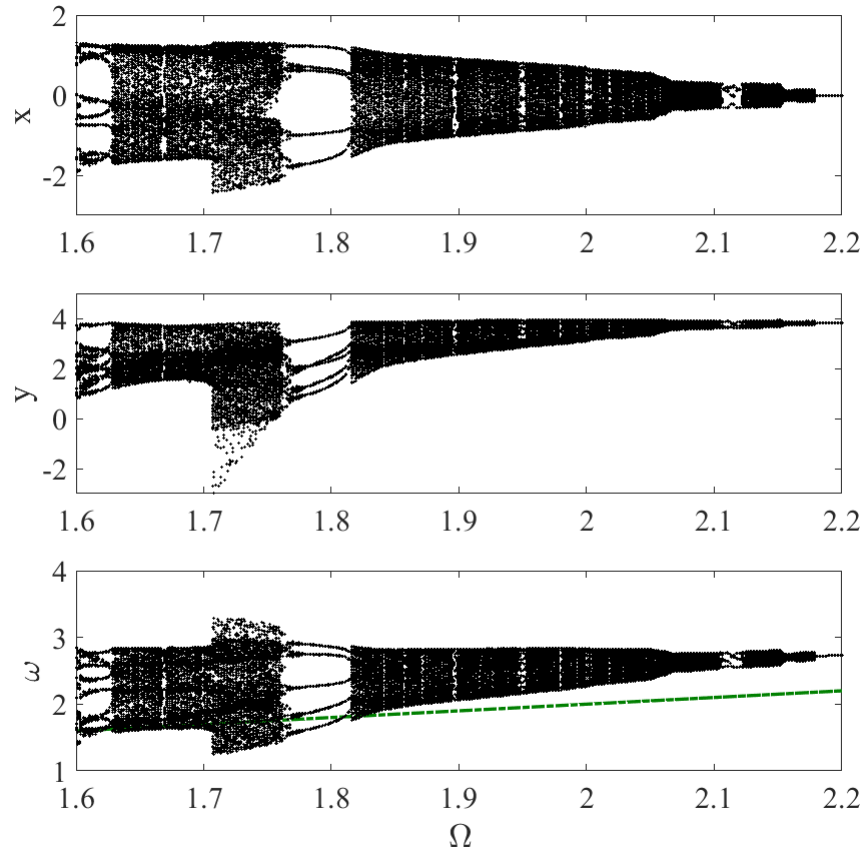


Figure 5.3: **Chaotic stroboscopic sections from numerical simulations.** Bifurcation diagram using the stroboscopic sections of the states of the horizontally forced pendulum adaptive frequency oscillator for Ω ranging from 1.6 rad/s to 2.2 rad/s. Here, $a = 1.8$, $c = 0.35$, and $k_\omega = 0.707$. The green dashed line represents the line $\omega = \Omega$. Instead of learning the external forcing frequency, the bifurcation diagram exhibits chaotic behavior.

For some parameter combinations, period-3 motion may be observed, which shows that this system is indeed chaotic [166]. In Fig. 5.4, period-3 motion may be seen in the time history. The three dimensional trajectory of the system is shown for comparison.

For other parameters, strange attractors may be observed. One of these strange attractors is depicted in Fig. 5.5.

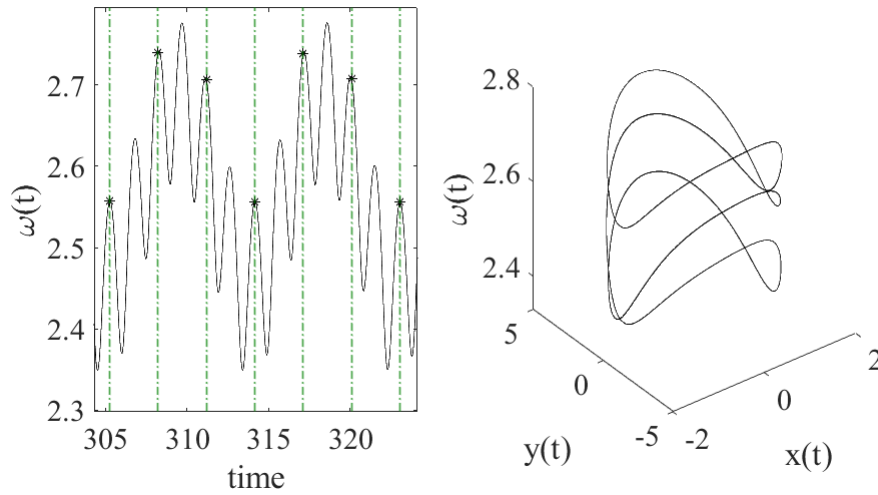


Figure 5.4: **Period-3 implies chaos.** For $\Omega = 2.12$ rad/s, the response of the ω state has period-3 motion. Here, $a = 1.8$, $c = 0.35$, and $k_\omega = 0.707$. On the left, the stroboscopic sections are shown for a portion of the time history. The vertical green dashed lines depict the clock's sampling rate for the stroboscope, and the * is the value of the ω state at these times. On the right, the three dimensional trajectory of the system is shown.

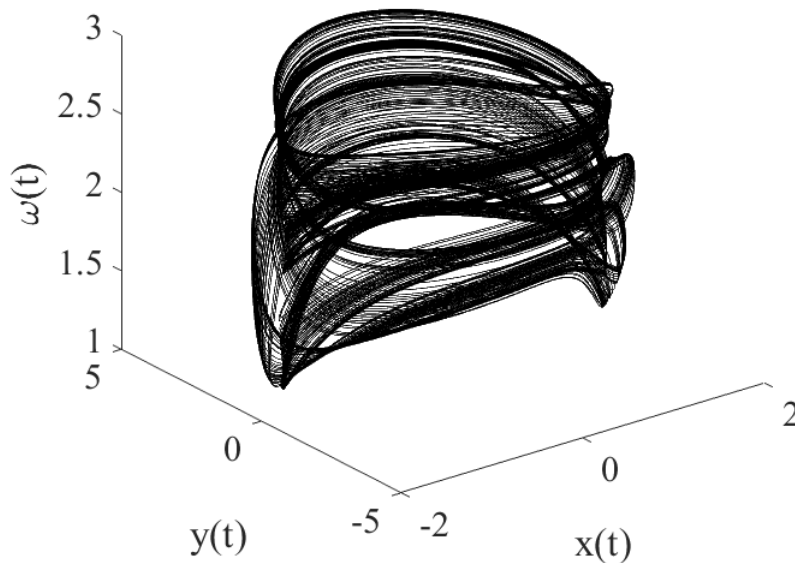


Figure 5.5: **Strange attractor from simulations.** For $\Omega = 1.67$, a strange attractor is shown. For this simulation, $a = 1.8$, $c = 0.35$, and $k_\omega = 0.707$.

5.3 Field-Programmable Analog Array Circuit

Circuit implementations of chaotic systems are widely used, such as realizations of a three-state chaotic flow [167], a jerk oscillator [31], a novel autonomous four-dimensional hyperjerk system with hyperbolic sine nonlinearity [168], a fractional-order-based chaos system [169], a three-state chaotic system with applications to robotic navigation [170], and a snap system with adjustable symmetry and nonlinearity [171]. Field-programmable analog arrays (FPAAs) are dynamically programmable analog signal processing devices that use switched-capacitor technology [172]. FPAAs contains configurable analog blocks (CABs), which create analog operations. Each math operation is further achieved by configurable analog modules (CAMs). By using FPAAs, the design of nonlinear systems are significantly reduced, as the technology is highly reconfigurable [173]. Several FPAA implementations of nonlinear dynamical system have been widely studied, which include the implementation of the Lorenz system [174], a cellular network-based Lorenz-like system [175], the Sprott N chaotic oscillator [176, 177], the Nahrain chaotic map [178], a fractional-order chaotic system [145], a chaotic oscillator [179], and the Hindmarsh–Rose Neuron model [180]. As compared with printed circuit boards, FPAAs can accomplish faster prototyping, without using large amounts of operational amplifiers and analog multipliers. The nonlinear functions, such as the sinusoids and square root operation in eq. 5.5, can be approximated as a user-defined voltage transfer function with CAMs. Utilizing the modular design of FPAAs, this pendulum frequency adaptive oscillator is implemented as a physical experiment.

However, the FPAA's input and output must be in a range between ± 3 volts. This necessitates that the response amplitude must be rescaled. Based on the numerical time response results shown in Fig. 5.3, only the y state significantly exceeds the maximum voltage range of the FPAA. It should also be noted that the FPAA experiment runs at 1000 times faster than the numerical simulations, due to the RC time constant of the FPAA. Thus, new states

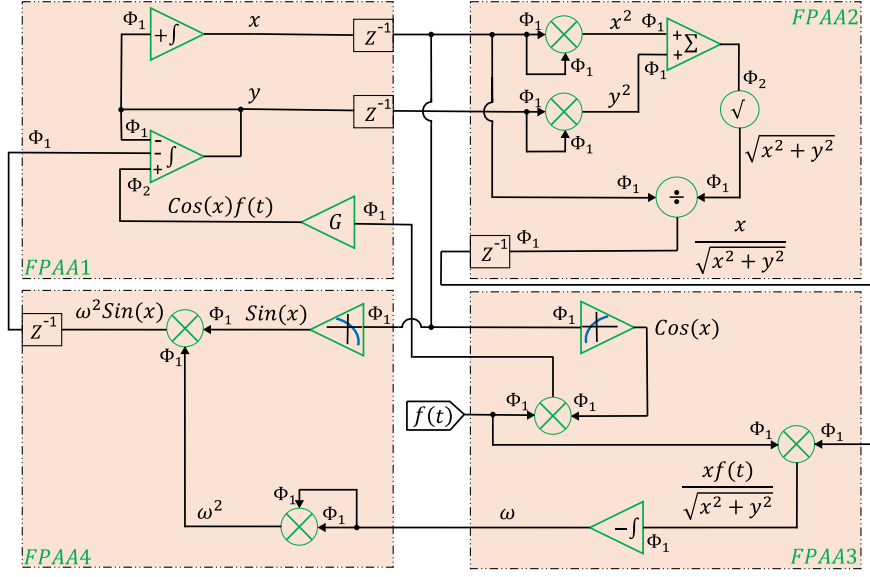


Figure 5.6: **FPAAs circuit schematic of pendulum adaptive frequency oscillator.** An external forcing signal was sent to the FPAAs via differential input IO3 of FPAA3.

are introduced such that $x = X$, $y = 2Y$, and $\omega = 1000W$. Using these relationships, eq. 5.5 is modified for use on the FPAAs as follows:

$$\begin{aligned}
 \dot{X}(t) &= 2Y(t) \\
 \dot{Y}(t) &= -cY(t) - \frac{1}{2} \left(W^2(t) \sin X(t) - a \cos(X(t)) \sin(\Omega t) \right) \\
 \dot{W}(t) &= \frac{-k_\omega X(t) a \sin(\Omega t)}{1000 \sqrt{X^2(t) + 4Y^2(t)}}
 \end{aligned} \tag{5.6}$$

An Anadigm Quad Apex v2.0 FPAAs development board with 4 AN231E04 chips was used. The *AnadigmDesigner2* simulator developed by Anadigm was used for FPAAs hardware routing and design. All the external stimuli for the experimental results were generated in MATLAB, and they were then input to the FPAAs through the differential IO cell using a National Instruments (NI) cDAQ-9174. Similarly, all the outputs of the FPAAs are collected by the NI unit.

5.4 Experimental Results

In this section, results from the FPAA pendulum adaptive frequency oscillator prototype are shown. For Figs. 5.7 and 5.8, the same procedure was used that was described for Figs. 5.2 and 5.3. A frequency sweep was performed on the FPAA analog circuit, and only the last 100 cycles were used for the stroboscopic section plots in Figs. 5.7 and 5.8 to avoid any transient behavior.

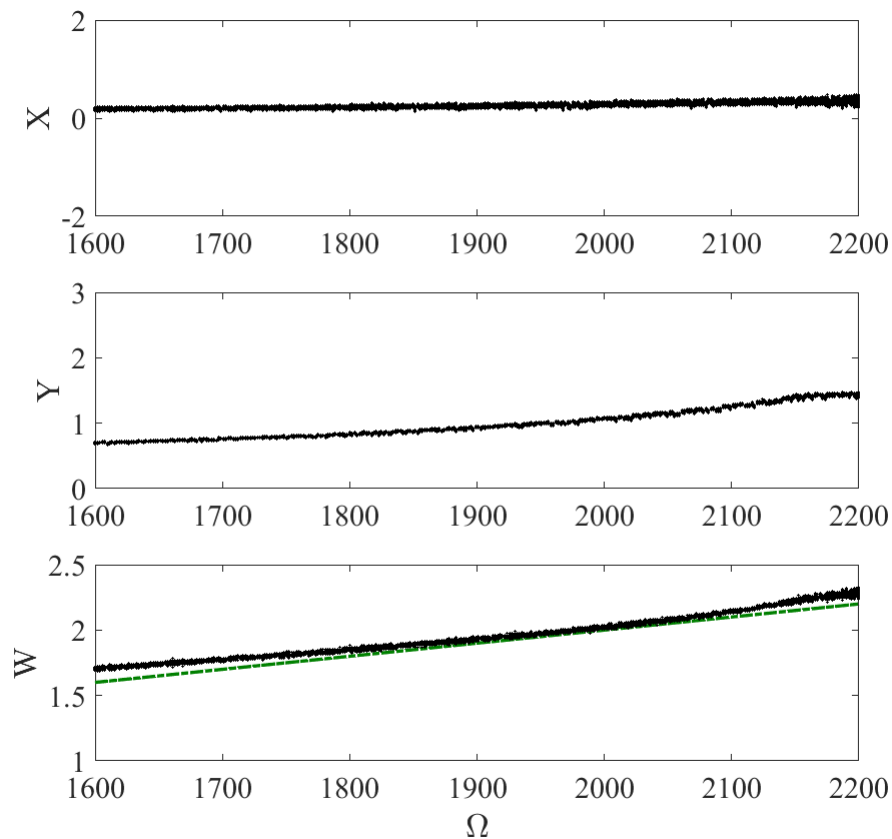


Figure 5.7: **Non-chaotic stroboscopic sections from experiments.** Stroboscopic sections of the states of the FPAA circuit for Ω ranging from 1600 rad/s to 2200 rad/s. Note that the FPAA runs at 1000 times faster than the simulations due to the RC time constant, so the W state should be multiplied by 1000 to calculate the learned frequency. Here, $a = 0.1$, $c = 0.35$, and $k_\omega = 0.707$. The green dashed line represents the line $\frac{\omega}{1000} = \Omega$. For this combination of parameters, the FPAA correctly learns the external forcing frequency.

In Fig. 5.7, the FPAA's stroboscopic sections show that the ω state (where $1000 * W = \omega$) closely learned the external forcing frequency, Ω . However, nonlinear features of the FPAA cause some errors that were not seen in the numerical simulations. Since the x and y states are periodic with the same frequency as the external sinusoid, their stroboscopic sections appear stationary with respect to this clock.

Repeating this same procedure that was used for Fig. 5.7, the bifurcation diagram is also constructed for the FPAA, which is depicted in Fig. 5.8. For this set of parameters, the FPAA has a chaotic response.

In the experimental FPAA prototype, strange attractors are also present. One of these strange attractors is depicted in Fig. 5.9.

Since the FPAA's frequency is scaled by 1000 from the simulations, the frequency for the strange attractor in Fig. 5.9 is comparable to the attractor shown in Fig. 5.5. Period-5 motion is depicted in Fig. 5.10 for the FPAA's response.

5.5 Conclusions

Adaptive oscillators are a potentially useful subset of nonlinear oscillators. However, they have not been thoroughly explored. In this paper, the pendulum adaptive frequency oscillator was studied. To the authors' knowledge, this is the first circuit prototype of a pendulum adaptive frequency oscillator, and this is the first time that chaos has been observed for an adaptive oscillator. This pendulum adaptive frequency oscillator was studied through numerical simulations and a field-programmable analog array prototype. As there is interest in using a mechanical pendulum as the base oscillator, this FPAA prototype provides a method of experimentally interrogating the dynamics of this system without building multiple costly mechanical prototypes.

It was found that for some parameter combinations, the pendulum adaptive frequency

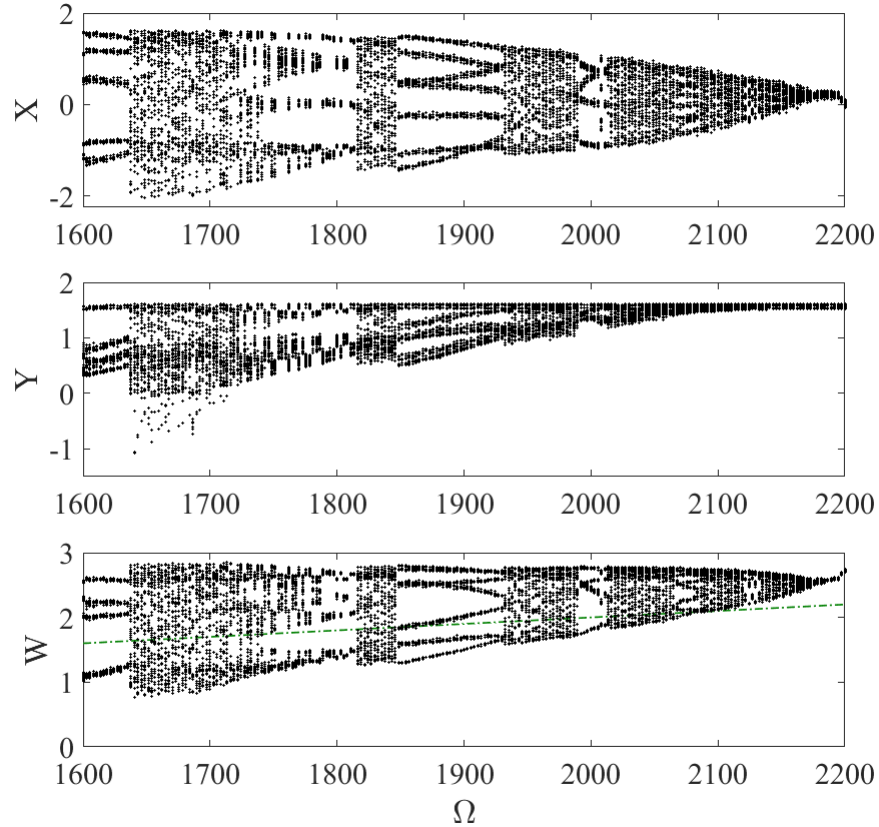


Figure 5.8: **Chaotic stroboscopic sections from experiments.** Bifurcation diagram using the stroboscopic sections of the states of the FPAA for Ω ranging from 1600 rad/s to 2200 rad/s. Note that the FPAA runs at 1000 times faster than the simulations due to the RC time constant, so the W state should be multiplied by 1000 to calculate the learned frequency. Here, $a = 1.8$, $c = 0.35$, and $k_\omega = 0.707$. The green dashed line represents the line $\frac{\omega}{1000} = \Omega$. Instead of learning the external forcing frequency, the bifurcation diagram exhibits chaotic behavior.

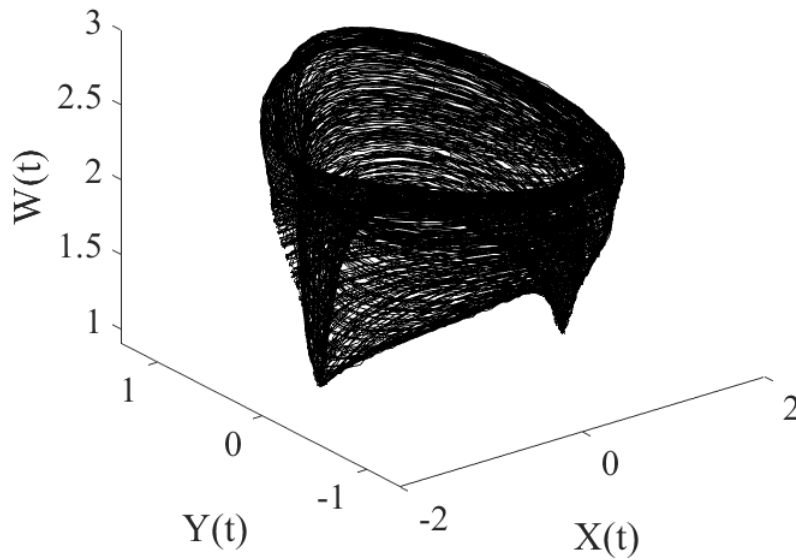


Figure 5.9: **Strange attractor from experiments.** For $\Omega = 1640$, a strange attractor is shown. For this experiment, $a = 1.8$, $c = 0.35$, and $k_\omega = 0.707$.

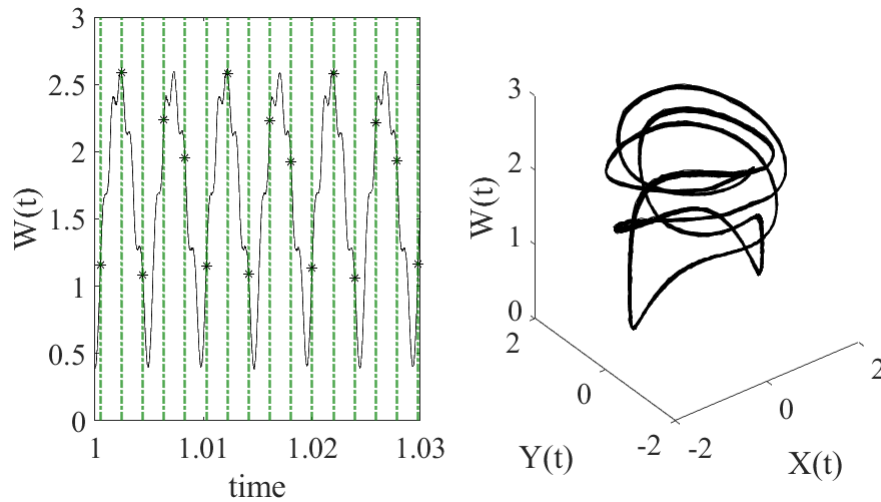


Figure 5.10: **Period-5 motion from experiment.** For $\Omega = 1880$ rad/s, the response of the W state has period-5 motion. Here, $a = 1.8$, $c = 0.35$, and $k_\omega = 0.707$. On the left, the stroboscopic sections are shown for a portion of the time history. The vertical green dashed lines depict the clock's sampling rate for the stroboscope, and the * is the value of the W state at these times. On the right, the three dimensional trajectory of the system is shown.

oscillator performed as expected in learning the external forcing frequency. At other parameter combinations, the pendulum adaptive frequency oscillator behaved chaotically. As the pendulum adaptive frequency oscillator has been proposed as a vibratory energy harvester, it is important to avoid this chaotic behavior, since the system would use energy to adapt the rod length of the pendulum.

Bifurcation diagrams were constructed for both the numerical simulations and the experiment. It should be noted that the bifurcation diagrams for the simulations and experiments were very similar, although they are not identical. Since this is a chaotic system, it is difficult to match the bifurcation diagrams of a model with an experiment, as chaotic systems have sensitive dependence on system parameters. In other words, it would be very difficult to tune the experiment's parameters to exactly match those used in the model. Strange attractors for both the simulations and experiment were also reported. Period-3 motion was found, which implies that the system is indeed chaotic.

CHAPTER

6

A HOPF ADAPTIVE OSCILLATOR ANALOG CIRCUIT AS A MUSICAL INSTRUMENT

Although they have not previously been used as musical instruments, analog adaptive oscillator circuits could be used as the building block of musical instruments. Previously, many different circuit designs were employed for guitar effect pedals and vocal modulation devices. In this chapter, an adaptive oscillator is implemented as an analog circuit, and it is then employed as a musical instrument to demonstrate its ability as a musical instrument. This circuit could easily be implemented into a guitar effect pedal or other similar instrument.

6.1 Circuit Implementation

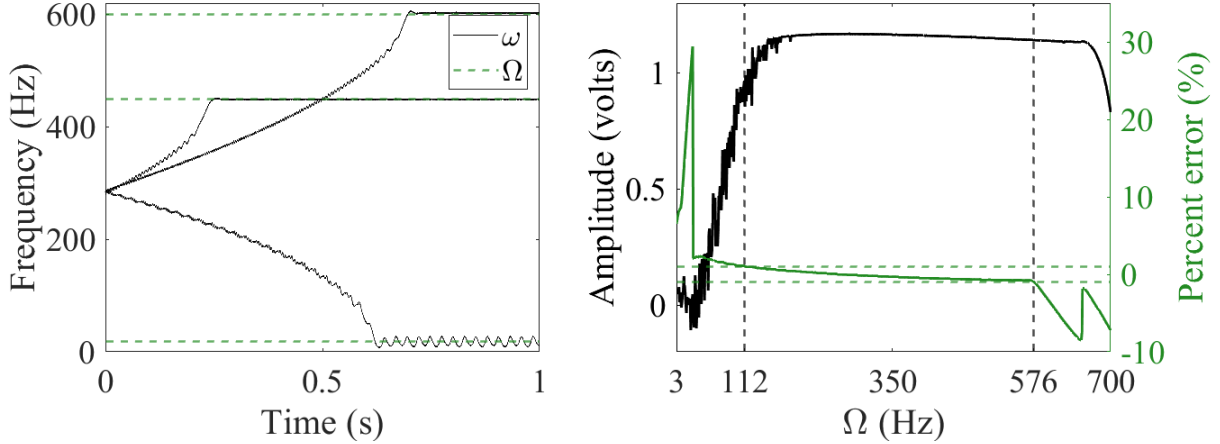


Figure 6.1: **Frequency response.** Aspects of the frequency learning capability of the bread-board circuit are shown here, where k_x , k_ω , and μ are equal to 1.2 V, 0.8 V, and 1 V, respectively. Left: The grey dashed lines denote the external forcing frequency, Ω . Three cases are shown, which are driving frequencies of 19 Hz, 450 Hz, and 600 Hz. The black solid lines depict the time evolution of the ω state. Right/Top: The frequency-amplitude relationship for the x state of the circuit is plotted with a black solid line. The vertical dashed lines correspond to the frequencies that fall within $\pm 1\%$ error. Right/Bottom: The percent error for the ω state is plotted with a black solid line. The horizontal dashed lines correspond to $\pm 1\%$ error, while the vertical dashed lines correspond to the frequencies that fall within $\pm 1\%$ error.

The equations for a Hopf adaptive frequency oscillator are as follows [1]:

$$\begin{aligned}
 \dot{x} &= (\mu - (x^2 + y^2))x - \omega y + k_x f(t) \\
 \dot{y} &= (\mu - (x^2 + y^2))y + \omega x \\
 \dot{\omega} &= -k_\omega f(t)y
 \end{aligned} \tag{6.1}$$

In this set of ordinary differential equations, x and y represent a regular Hopf oscillator [140] that is driven by an external force, $f(t)$. However, ω in the first two equations is typically a constant. Here, ω is a time-dependent state that evolves based on the third

equation. μ is a constant that controls the radius of the limit cycle, which is the oscillation amplitude of the x and y states. k_x and k_ω are coupling constants.

The system in eq. 6.1 was then mapped to eq. 6.2, by using Kirchhoff's laws to create a standard, voltage-mode operational amplifier integrator configuration with voltage multipliers:

$$\begin{aligned}\dot{V}_x &= -\frac{1}{R_2 C_1} (V_\mu - (V_x^2 + V_y^2)) V_x + \frac{1}{R_3 C_1} V_\omega V_y - \frac{1}{R_1 C_1} f(t) \\ \dot{V}_y &= -\frac{1}{R_4 C_2} (V_\mu - (V_x^2 + V_y^2)) V_y - \frac{1}{R_5 C_2} V_\omega V_x \\ \dot{V}_\omega &= \frac{1}{R_6 C_3} f(t) V_y\end{aligned}\tag{6.2}$$

The states V_x , V_y , and V_ω correspond to the voltage outputs of the operational amplifier integrators. An analog circuit equivalent to the dynamical system of the Hopf adaptive frequency oscillator described in eq. 6.1 was designed and implemented on a breadboard.

Several tests were performed to verify the frequency learning capability of this circuit. The dynamic response of the ω state to several forcing frequencies is shown in the left portion of Fig. 6.1, for Ω values of 19 Hz, 450 Hz, and 600 Hz. A forcing frequency sweep was performed from 3 Hz to 700 Hz (i.e., Ω was quasi-statically varied from 3 Hz to 700 Hz). It should be noted that the frequency-amplitude response of an underdamped, linear oscillator has a definitive peak. Since the adaptive oscillator can adapt to the external frequency, the frequency-amplitude response of this nonlinear system, unlike its linear counterpart, has a broadband frequency range with a relatively flat response with a large amplitude. The percent error is calculated as $\frac{\Omega - \langle \omega \rangle}{\Omega} \times 100$, where $\langle \omega \rangle$ is the mean of the ω state at steady state. The error is less than 1% when the forcing frequency is between 112 Hz and 576 Hz.

A circuit schematic is shown in Fig. 6.2. Here, two resistors, annotated as R_1 and R_6 , are set as 27 k Ω and 12.5 k Ω , respectively. These two resistors are used to control the coupling constants, k_x and k_ω . In addition, four other resistors, annotated as R_2 , R_3 , R_4 , and R_5 , are

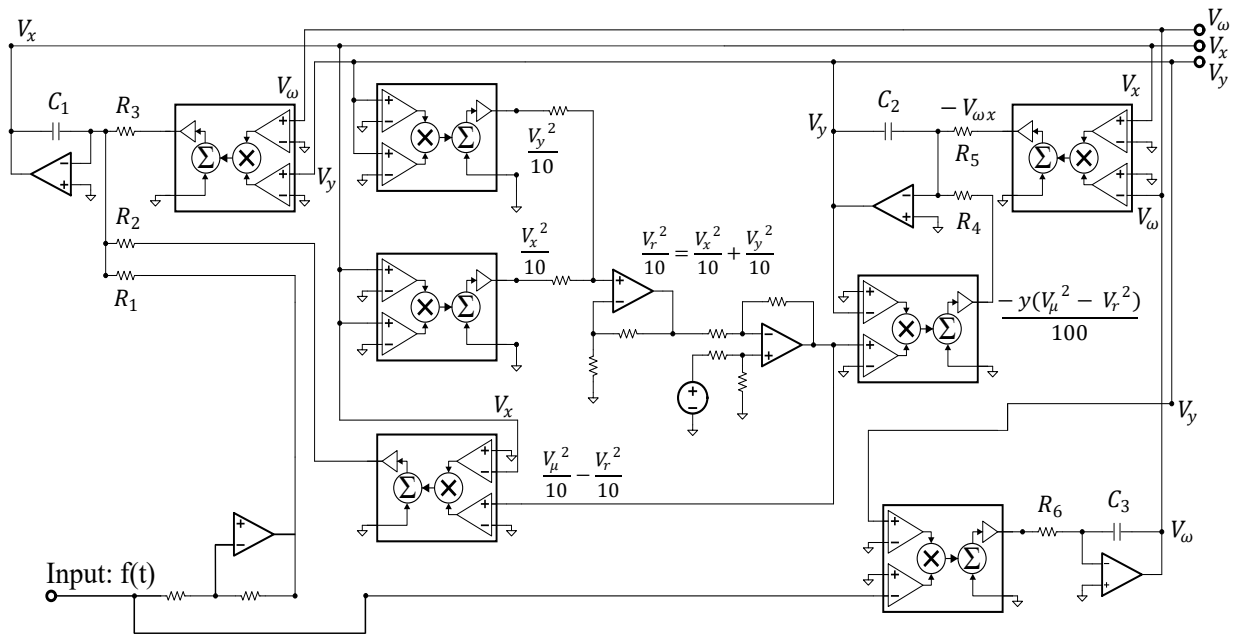


Figure 6.2: **Circuit schematic for the Hopf adaptive frequency oscillator.** This circuit has states V_x , V_y , V_ω , where TL082 operational amplifiers and AD633 multipliers are powered by a 15 V DC component.

set as 1 k Ω , 10 k Ω , 1 k Ω , 10 k Ω , respectively. All unlabeled resistors are 1 k Ω . The capacitors, annotated as C_1 , C_2 , and C_3 , have a capacitance of 33 nF, and μ is powered with a 1 V DC component. The circuit implementation was realized using TL082 operational amplifiers and AD633 multipliers in standard configurations. All passive components have a 1% error tolerance for resistors and a 2% error tolerance for capacitors.

6.2 Musical Process

To use this Hopf adaptive frequency oscillator as an instrument, the circuit is “played” by sending a desired time series as an input voltage, $f(t)$. The dynamics of the Hopf adaptive frequency oscillator are then recorded. The time series, $f(t)$, was sent to the circuit using a National Instrument (NI) cDAQ-9174 controlled by MATLAB, which was also used to record the x , y , and ω states of the circuit. It should be noted that no filters were used for this work, and the sampling frequency used for data acquisition was 44100 samples/second, which is the most common sampling rate for audio recordings.

In the next section, an AI-based vocal track remover [181] was used to isolate the vocal track, which will be denoted as f_{vocals} , from a sound file containing vocals and instrument accompaniment. If the external force is near zero, the circuit acts as a voltage controlled oscillator. When this happens, the circuit’s ω state will converge to an arbitrary pitch, which depends on the circuit components and the DC power voltage. In general, this arbitrary pitch is not in the same key as the song. To rectify this mistuning, an additional signal is added to the vocals, which is expressed as:

$$F_{pedal} = a(\sin(\omega_1 t) + \sin(\omega_2 t) + \sin(\omega_3 t)) \quad (6.3)$$

where a is a small, positive number, and ω_1 , ω_2 , and ω_3 are three frequencies corresponding

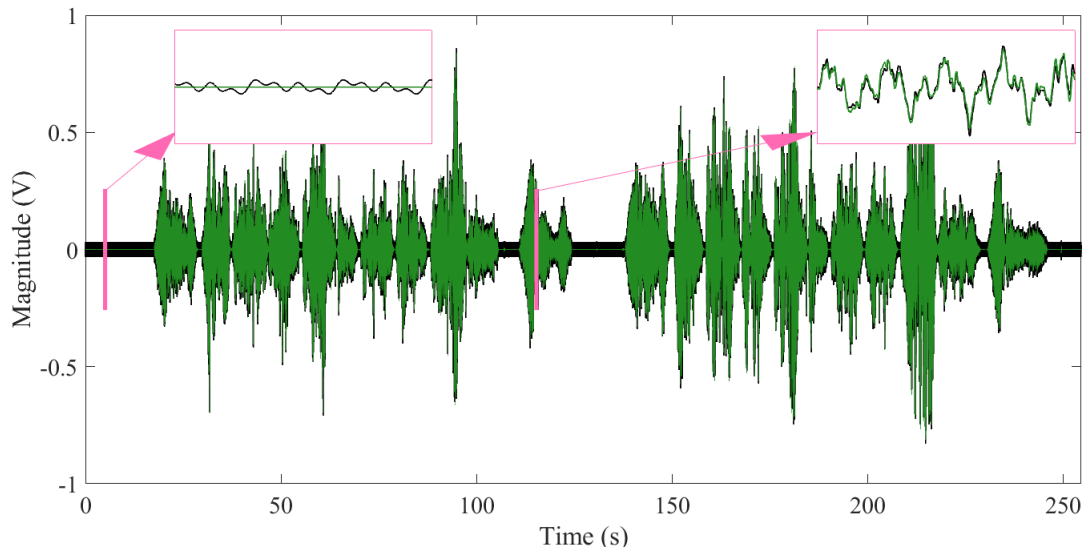


Figure 6.3: **Comparison of original vocals to response of circuit.** A comparison of the original vocals, f_{vocals} , (denoted as grey dash-dotted line) and the vocals with the pedal points, $f_{vocals} + f_{pedal}$ (denoted as black solid line). The inset windows show zoomed portions for visualization purposes. The left inset shows an example when the vocals are not present; in this inset, the vocals are approximately equal to zero, while the pedal points cause small sinusoidal fluctuations. The right inset shows an example when the vocals are present. It should be noted that f_{vocals} and $f_{vocals} + f_{pedal}$ are very similar in the right inset.

to the tonic of the musical piece. Thus, the input of the circuit is expressed as $f(t) = F_{pedal} + f_{vocals}$. This additional signal, f_{pedal} , acts as a set of *pedal points*. Pedal points are notes that are sustained for long amounts of time, while other musical progression is occurring. The amplitude of f_{pedal} is chosen to be small enough that it does not interfere with the circuit learning f_{vocal} , but it influences the ω state to converge to the tonic when no vocals are present. As an example, the time series comparison of the original vocals, f_{vocals} , and vocals added with pedal point signal, f_{pedal} , is shown in Fig. 6.3.

6.3 Example: *Ave Maria*

In this section, *Ave Maria* [182] will be used as a benchmark task. A sound file for this example may be found on Dryad (link removed to preserve anonymity, but example is included as supplementary material) For the example in this section, a vocal and piano version was used [183]. Since this version of the song is in the key of *D*, f_{pedal} was chosen such that $a = 0.165$ V, $\omega_1 = 922.58$ rad/s (D_3), $\omega_2 = 1845.15$ rad/s (D_4), and $\omega_3 = 3690.30$ rad/s (D_5). The external force, $f(t)$, used for this example is depicted in black in Fig. 6.3.

Fast Fourier Transform (FFT) results are shown in Fig. 6.4. In the top of Fig. 6.4, the FFT of $f_{vocals} + f_{pedal}$ is shown; in the bottom of Fig. 6.4, the FFT of the experimental y state is shown. Both of these FFTs were normalized to aid in comparison. The pedal points have a large amplitude in the frequency domain, since they are always present. It can be seen from the FFTs that the y state has a narrower range of frequencies present in the response. This is expected, since the operating range of the circuit is between approximately 112 Hz and 576 Hz.

This Hopf adaptive frequency oscillator has three states. A portion of the response of the x and y states is shown in Fig. 6.5. Since the x state appears to have additional higher frequency components, the y state was used as the “voice” of the instrument. These

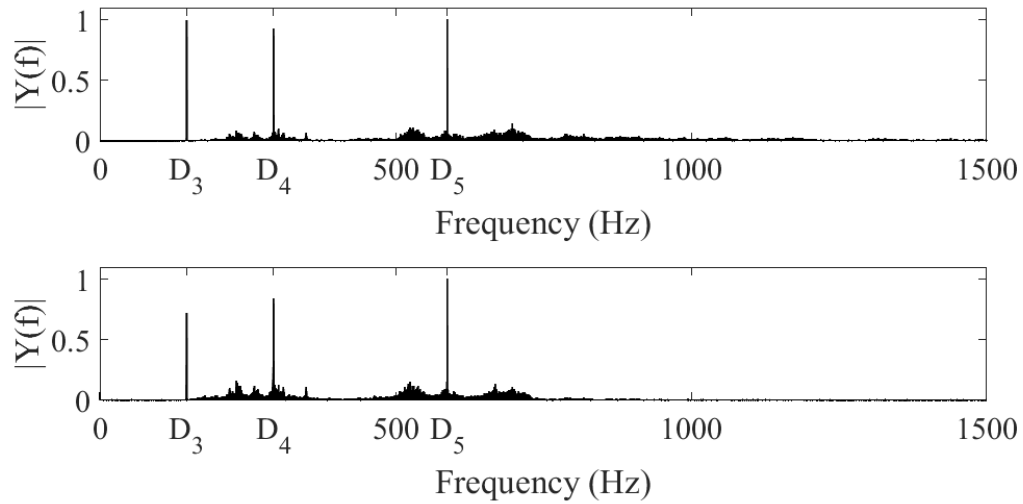


Figure 6.4: **A comparison of the single-sided amplitude spectrum between $f_{vocals} + f_{pedal}$ (top) and the experimental results of the y state (bottom).** The pedal points have a large amplitude in the FFT because they are always present in the external forcing, $f(t)$. Both FFTs were normalized for comparison purposes.

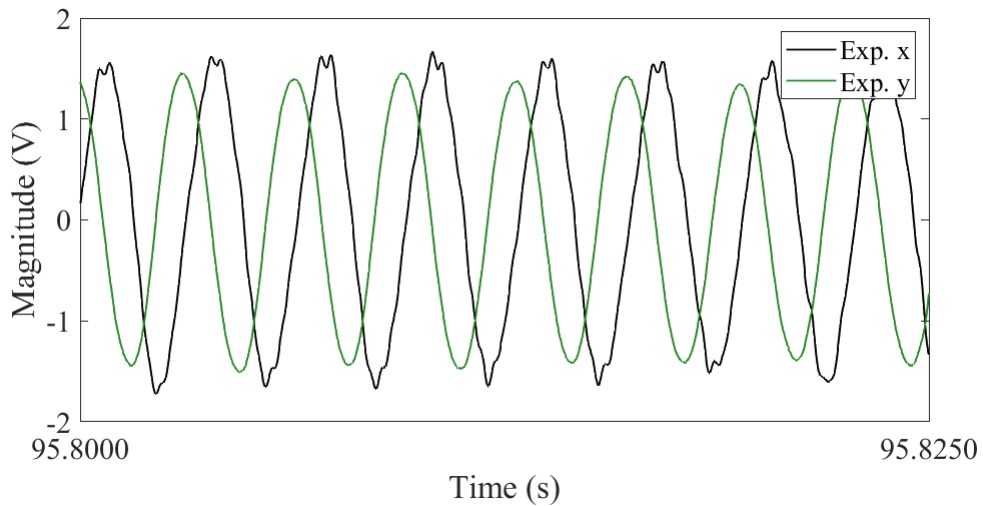


Figure 6.5: **A portion of the response of the x (solid) and y (dashed) states from the circuit.** Since the x state has higher frequency components, the y state was chosen for the “voice” of the instrument.

higher frequency components may be seen from the superimposed fluctuations on the sinusoidal oscillations in the x state. In addition, time series data of the experimental ω state is shown in Fig. 6.6. This third state converges to the pedal point components when the amplitude of the vocals is too small. Whenever the vocals are present, the ω state tends to converge to one of the main frequency components of the vocal input. The probability that the ω state converges to the fundamental of the vocals or an overtone is affected by the amplitudes of the fundamental and overtones, as well as the previous value of the ω state. This complex behavior provides a rendition of the vocals that are dissimilar to the original melody, without being unduly dissonant.

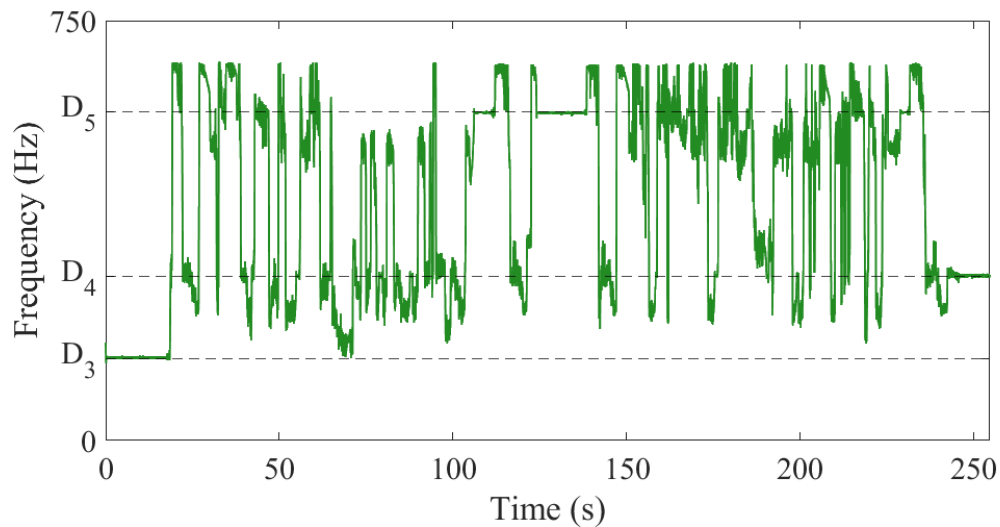


Figure 6.6: **Time response of the experimentally collected ω state.** The pedal points, annotated as D_3 , D_4 and D_5 , are plotted as dashed black lines for comparison. One of these pedal point frequencies is learned by the circuit when the amplitude of the vocals is too small.

6.4 Conclusion

There has been a long history of creating musical instruments and musical instrument components from analog circuits. In this paper, a Hopf adaptive frequency oscillator circuit was described, constructed, and tested, which could learn frequencies of an external signal. Based on a quasi-static frequency sweep, this circuit operated from approximately 112 Hz to 576 Hz with less than 1% error. By changing the capacitance used in the operational amplifier-based integrator networks, this operating range could be shifted to create different musical effects.

Using *Ave Maria* as a test case, the vocals were isolated from the piano accompaniment using an AI. Since the circuit acts as a voltage-controlled oscillator when there is no external input, a method of creating pedal points was used to avoid long periods of dissonance. These pedal point frequencies can be modified based on the key of the music. The y state was chosen as the instrument's "voice", since it often has less higher frequency components than the x state. This is likely because the external force, $f(t)$, is injected directly into the x state. The y state from the circuit was then added back to the piano accompaniment.

Although adaptive oscillators were previously suggested to be used for automatic music transcription, these nonlinear oscillators can themselves be employed as musical instruments or analog nonlinear distortion source. The circuit described in this paper is analog, which provides rich and complex dynamics. By mitigating undue dissonance caused by voltage-controlled oscillations through the addition of pedal points, this circuit adapts to different overtones of the original vocals. In this way, the Hopf adaptive frequency oscillator produces a time series that is aesthetically pleasing and musically compelling.

CHAPTER

7

CONCLUSIONS & FUTURE WORK

7.1 Summary of Results

In Chapter 2, a 4-state Hopf adaptive oscillator was presented, which was capable of learning both frequency and amplitude of an external signal. This was demonstrated in both numerical simulations and a novel prototype analog circuit. In addition, the local stability of the system was studied using Floquet analysis. This circuit's operating range could be easily scaled up or down by varying the electrical components. This adaptive oscillator was verified as an analog frequency analyzer by sending various signals to the circuit.

In Chapter 3, the stochastic dynamics of a 3-state Hopf adaptive frequency oscillator

were studied. Euler-Maruyama numerical simulations, the cumulant neglect equations from the Fokker-Planck equation, and experimental results were all compared. It was found that noise causes the limit cycle motion to collapse in one dimension, which subsequently degrades the learning process.

In Chapter 4, the pendulum adaptive frequency oscillator was proposed. Numerical simulations of this system were shown, and a physical implementation was designed, fabricated, and constructed. The method of multiple scales was used to approximate the dynamics of this system, which was then used to statistically calculate parameters of the experiment. This pendulum adaptive frequency oscillator could be used as a smart energy harvester, which tracks non-stationary vibrations in the environment.

In Chapter 5, the pendulum adaptive frequency oscillator was further studied. In this chapter, a field-programmable analog array was used as an experiment, since the mechanical experiment could not be actuated at a high enough speed. To the author's knowledge, this was the first time that chaos was demonstrated in an adaptive oscillator.

In Chapter 6, a Hopf adaptive frequency oscillator was proposed as a musical instrument component. The adaptive oscillator has previously been used as an automatic music transcription device. To the author's knowledge, it has not previously been used to make music. By sending the vocal signal of a song to this circuit, the adaptive oscillator provided a novel musical effect. This could be implemented as a guitar effect pedal.

7.2 Future Work

In this dissertation, the local stability of the Hopf adaptive oscillator was considered. However, it is likely that nonlinear effects play a significant role in the global stability of this system. Numerically finding the basins of attraction of adaptive oscillators could provide a better understanding of the global stability of these systems. In addition, other types of

analysis, such as the method of multiple scales or center manifold reduction techniques, could be used to gain additional insights into robust regions.

Adaptive oscillators could be used as smart energy harvesters, which track and exploit moving periodic sources of energy. However, the cost of adaptation in terms of energy has not been completed. To use these adaptive oscillators as energy harvesters, efficient adaptation procedures would need to be explored. Further, the energy expended through adaptation should be compared with the additional energy gained from adaptation.

In previous work, simplifying the Fokker-Planck equation resulted in significantly different dynamics from the results presented in this dissertation. The role of noise on other types of adaptive oscillators is, however, rather unclear and unexplored.

In closing, adaptive oscillators could be used in many applications, including analog signal processing, robotic gait control, smart energy harvesting, musical instruments, and advanced phase-lock loop applications. It is likely that adaptive oscillators can be constructed from most nonlinear oscillators, so there are many adaptive oscillators that have not been studied in detail. This dissertation provides a basis for some of these key technologies and provides some insights into their dynamics.

REFERENCES

- [1] Ludovic Righetti, Jonas Buchli, and Auke Jan Ijspeert. Dynamic hebbian learning in adaptive frequency oscillators. *Physica D: Nonlinear Phenomena*, 216(2):269–281, 2006.
- [2] Edmon Perkins. Effects of noise on the frequency response of the monostable duffing oscillator. *Physics Letters A*, 381(11):1009–1013, 2017.
- [3] Jun Nishii. A learning model for oscillatory networks. *Neural networks*, 11(2):249–257, 1998.
- [4] Timo Nachstedt, Christian Tetzlaff, and Poramate Manoonpong. Fast dynamical coupling enhances frequency adaptation of oscillators for robotic locomotion control. *Frontiers in neurorobotics*, 11:14, 2017.
- [5] Richard Kempter, Wulfram Gerstner, and J Leo Van Hemmen. Hebbian learning and spiking neurons. *Physical Review E*, 59(4):4498, 1999.
- [6] Shinya Watanabe and Steven H Strogatz. Constants of motion for superconducting josephson arrays. *Physica D: Nonlinear Phenomena*, 74(3-4):197–253, 1994.
- [7] Douglas Eck. Finding downbeats with a relaxation oscillator. *Psychological research*, 66(1):18–25, 2002.
- [8] Md Shougat, Raf E Ul, XiaoFu Li, Tushar Mollik, and Edmon Perkins. An information theoretic study of a duffing oscillator array reservoir computer. *Journal of Computational and Nonlinear Dynamics*, 16(8), 2021.
- [9] Md Raf E Ul Shougat, XiaoFu Li, Tushar Mollik, and Edmon Perkins. A hopf physical reservoir computer. *Scientific Reports*, 11(1):1–13, 2021.
- [10] Md Raf E Ul Shougat, XiaoFu Li, and Edmon Perkins. Dynamic effects on reservoir computing with a hopf oscillator. *Physical Review E*, 105(4):044212, 2022.
- [11] Arash Ahmadi, Eduardo Mangieri, Koushik Maharatna, Srinandan Dasmahapatra, and Mark Zwolinski. On the vlsi implementation of adaptive-frequency hopf oscillator. *IEEE Transactions on Circuits and Systems I: Regular Papers*, 58(5):1076–1088, 2010.
- [12] Mohammad Ali Maleki, Arash Ahmadi, Seyed Vahab Al-Din Makki, Hamid Soleimani, and Mohammad Bavandpour. Networked adaptive non-linear oscillators: a digital synthesis and application. *Circuits, Systems, and Signal Processing*, 34(2):483–512, 2015.

- [13] J Cristiano, D Puig, and MA Garcia. Efficient locomotion control of biped robots on unknown sloped surfaces with central pattern generators. *Electronics Letters*, 51(3):220–222, 2015.
- [14] Ludovic Righetti, Jonas Buchli, and Auke Jan Ijspeert. From dynamic hebbian learning for oscillators to adaptive central pattern generators. In *Proceedings of 3rd International Symposium on Adaptive Motion in Animals and Machines–AMAM 2005*, pages –. Verlag ISLE, Ilmenau, 2005.
- [15] Ludovic Righetti and Auke Jan Ijspeert. Programmable central pattern generators: an application to biped locomotion control. In *Proceedings 2006 IEEE International Conference on Robotics and Automation, 2006. ICRA 2006.*, pages 1585–1590. IEEE, 2006.
- [16] Jonas Buchli and Auke Jan Ijspeert. Self-organized adaptive legged locomotion in a compliant quadruped robot. *Autonomous Robots*, 25(4):331, 2008.
- [17] Alexander Sproewitz, Rico Moeckel, Jérôme Maye, and Auke Jan Ijspeert. Learning to move in modular robots using central pattern generators and online optimization. *The International Journal of Robotics Research*, 27(3-4):423–443, 2008.
- [18] Kentaro Takeda and Hiroyuki Torikai. A novel hardware-efficient central pattern generator model based on asynchronous cellular automaton dynamics for controlling hexapod robot. *IEEE Access*, 2020.
- [19] Jose Hugo Barron-Zambrano and Cesar Torres-Huitzil. Fpga implementation of a configurable neuromorphic cpg-based locomotion controller. *Neural Networks*, 45:50–61, 2013.
- [20] Xiaofeng Xiong, Florentin Wörgötter, and Poramate Manoonpong. Adaptive and energy efficient walking in a hexapod robot under neuromechanical control and sensorimotor learning. *IEEE transactions on cybernetics*, 46(11):2521–2534, 2015.
- [21] Mathias Thor and Poramate Manoonpong. A fast online frequency adaptation mechanism for cpg-based robot motion control. *IEEE Robotics and Automation Letters*, 4(4):3324–3331, 2019.
- [22] Chengju Liu, Danwei Wang, and Qijun Chen. Central pattern generator inspired control for adaptive walking of biped robots. *IEEE Transactions on Systems, Man, and Cybernetics: Systems*, 43(5):1206–1215, 2013.
- [23] SMRS Noorani, Ahmad Ghanbari, and MA Jafarizadeh. Efficiency on legged locomotion pattern using adaptive frequency hopf oscillator. In *2013 First RSI/ISM International Conference on Robotics and Mechatronics (ICRoM)*, pages 307–312. IEEE, 2013.

- [24] Jonas Buchli, Fumiya Iida, and Auke Jan Ijspeert. Finding resonance: Adaptive frequency oscillators for dynamic legged locomotion. In *2006 IEEE/RSJ International Conference on Intelligent Robots and Systems*, pages 3903–3909. IEEE, 2006.
- [25] Hyundo Choi, Keehong Seo, Seungyong Hyung, Youngbo Shim, and Soo-Chul Lim. Compact hip-force sensor for a gait-assistance exoskeleton system. *Sensors*, 18(2):566, 2018.
- [26] Keehong Seo, SeungYong Hyung, Byung Kwon Choi, Younbaek Lee, and Youngbo Shim. A new adaptive frequency oscillator for gait assistance. In *2015 IEEE International Conference on Robotics and Automation (ICRA)*, pages 5565–5571. IEEE, 2015.
- [27] Renaud Ronsse, Nicola Vitiello, Tommaso Lenzi, Jesse Van Den Kieboom, Maria Chiara Carrozza, and Auke Jan Ijspeert. Human–robot synchrony: flexible assistance using adaptive oscillators. *IEEE Transactions on Biomedical Engineering*, 58(4):1001–1012, 2010.
- [28] Koushik Maharatna, Arash Ahmadi, and Eduardo Magieri. Biologically inspired analogue signal processing: Some results towards developing next generation signal analyzers. In *Proceedings of the 2009 12th International Symposium on Integrated Circuits*, pages 542–545. IEEE, 2009.
- [29] Jonas Buchli, Ludovic Righetti, and Auke Jan Ijspeert. Frequency analysis with coupled nonlinear oscillators. *Physica D: Nonlinear Phenomena*, 237(13):1705–1718, 2008.
- [30] Benjamin K Rhea, Edmon Perkins, and Robert N Dean. High frequency realization of non-autonomous nonlinear transistor circuit. *AIP Advances*, 9(6):065112, 2019.
- [31] Benjamin K Rhea, R Chase Harrison, Frank T Werner, Edmon Perkins, and Robert N Dean. Approximating an exactly solvable chaotic oscillator using a colpitts oscillator circuit. *IEEE Transactions on Circuits and Systems II: Express Briefs*, 68(3):1028–1032, 2020.
- [32] M Rahmani and I Nodozi. Phase-locked loops redesign by the lyapunov theory. *Electronics Letters*, 51(21):1664–1666, 2015.
- [33] Juan A Acebrón, Luis L Bonilla, Conrad J Pérez Vicente, Félix Ritort, and Renato Spigler. The kuramoto model: A simple paradigm for synchronization phenomena. *Reviews of modern physics*, 77(1):137, 2005.
- [34] Jian-qing Xu and Guojun Jin. Synchronization of parallel-connected spin-transfer oscillators via magnetic feedback. *Journal of Applied Physics*, 2012.
- [35] David Métivier, Lucas Wetzel, and Shamik Gupta. Onset of synchronization in networks of second-order kuramoto oscillators with delayed coupling: Exact results and application to phase-locked loops. *Physical Review Research*, 2(2):023183, 2020.

- [36] U Dürig, HR Steinauer, and N Blanc. Dynamic force microscopy by means of the phase-controlled oscillator method. *Journal of applied physics*, 82(8):3641–3651, 1997.
- [37] Sara Moradi, Johan Anderson, and Ozgür D Gürçan. Predator-prey model for the self-organization of stochastic oscillators in dual populations. *Physical Review E*, 92(6):062930, 2015.
- [38] Lior Ben Arosh, MC Cross, and Ron Lifshitz. Quantum limit cycles and the rayleigh and van der pol oscillators. *Physical Review Research*, 3(1):013130, 2021.
- [39] Yuzuru Kato and Hiroya Nakao. Instantaneous phase synchronization of two decoupled quantum limit-cycle oscillators induced by conditional photon detection. *Physical Review Research*, 3(1):013085, 2021.
- [40] Jiahua Li, Chunling Ding, and Ying Wu. Highly nonclassical phonon emission statistics through two-phonon loss of van der pol oscillator. *Journal of Applied Physics*, 128(23):234302, 2020.
- [41] Alexander A Mitrofanov, Ansar R Safin, Nikolay N Udalov, and Mikhail V Kapranov. Theory of spin torque nano-oscillator-based phase-locked loop. *Journal of applied physics*, 122(12):123903, 2017.
- [42] Henry W Ott and Henry W Ott. *Noise reduction techniques in electronic systems*, volume 442. Wiley New York, 1988.
- [43] Peter Hänggi. Stochastic resonance in biology how noise can enhance detection of weak signals and help improve biological information processing. *ChemPhysChem*, 3(3):285–290, 2002.
- [44] Jacob E Levin and John P Miller. Broadband neural encoding in the cricket cereal sensory system enhanced by stochastic resonance. *Nature*, 380(6570):165–168, 1996.
- [45] A Guderian, G Dechert, K-P Zeyer, and FW Schneider. Stochastic resonance in chemistry. 1. the belousov- zhabotinsky reaction. *The Journal of Physical Chemistry*, 100(11):4437–4441, 1996.
- [46] A Perez-Madrid and JM Rubi. Stochastic resonance in a system of ferromagnetic particles. *Physical Review E*, 51(5):4159, 1995.
- [47] Edmon Perkins, Masayuki Kimura, Takashi Hikihara, and Balakumar Balachandran. Effects of noise on symmetric intrinsic localized modes. *Nonlinear Dynamics*, 85(1):333–341, 2016.
- [48] Balakumar Balachandran, Edmon Perkins, and Timothy Fitzgerald. Response localization in micro-scale oscillator arrays: influence of cubic coupling nonlinearities. *International Journal of Dynamics and Control*, 3(2):183–188, 2015.

- [49] Edmon Perkins. Restricted normal mode analysis and chaotic response of p-mode intrinsic localized mode. *Nonlinear Dynamics*, 97(2):955–966, 2019.
- [50] Roberto Benzi, Alfonso Sutera, and Angelo Vulpiani. The mechanism of stochastic resonance. *Journal of Physics A: mathematical and general*, 14(11):L453, 1981.
- [51] Luca Gammaitoni, Peter Hänggi, Peter Jung, and Fabio Marchesoni. Stochastic resonance: a remarkable idea that changed our perception of noise. *The European Physical Journal B*, 69(1):1–3, 2009.
- [52] Emmett Redd, Steven Senger, and Tayo Obafemi-Ajayi. Noise optimizes super-turing computation in recurrent neural networks. *Physical Review Research*, 3(1):013120, 2021.
- [53] V Sh Aliev, SG Bortnikov, and IA Badmaeva. Investigations of stochastic resonance in two-terminal device with vanadium dioxide film. *Journal of Applied Physics*, 115(20):204511, 2014.
- [54] M d’Aquino, C Serpico, R Bonin, G Bertotti, and ID Mayergoyz. Thermally induced synchronization and stochastic resonance between magnetization regimes in spin-transfer nano-oscillators. *Journal of Applied Physics*, 111(7):07C915, 2012.
- [55] K Nakada, S Yakata, and T Kimura. Noise-induced synchronization in spin torque nano oscillators. *Journal of Applied Physics*, 111(7):07C920, 2012.
- [56] Yong Xu, Rencai Gu, Huiqing Zhang, Wei Xu, and Jinqiao Duan. Stochastic bifurcations in a bistable duffing–van der pol oscillator with colored noise. *Physical Review E*, 83(5):056215, 2011.
- [57] Anna Zakharova, Tatjana Vadivasova, Vadim Anishchenko, Aneta Koseska, and Jürgen Kurths. Stochastic bifurcations and coherencelike resonance in a self-sustained bistable noisy oscillator. *Physical Review E*, 81(1):011106, 2010.
- [58] AR Bulsara and G Schmerla. Stochastic resonance in globally coupled nonlinear oscillators. *Physical Review E*, 47(5):3734, 1993.
- [59] Dáibhid Ó Maoiléidigh. Multiple mechanisms for stochastic resonance are inherent to sinusoidally driven noisy hopf oscillators. *Physical Review E*, 97(2):022226, 2018.
- [60] OV Ushakov, H-J Wünsche, F Henneberger, IA Khovanov, Lutz Schimansky-Geier, and MA Zaks. Coherence resonance near a hopf bifurcation. *Physical review letters*, 95(12):123903, 2005.
- [61] Anna Zakharova, Alexey Feoktistov, Tatyana Vadivasova, and Eckehard Schöll. Coherence resonance and stochastic synchronization in a nonlinear circuit near a subcritical hopf bifurcation. *The European Physical Journal Special Topics*, 222(10):2481–2495, 2013.

- [62] Sebastian Wieczorek. Stochastic bifurcation in noise-driven lasers and hopf oscillators. *Physical Review E*, 79(3):036209, 2009.
- [63] C Sun and VJMS Jahangiri. Bi-directional vibration control of offshore wind turbines using a 3d pendulum tuned mass damper. *Mechanical Systems and Signal Processing*, 105:338–360, 2018.
- [64] Nalin A Chaturvedi, Taeyoung Lee, Melvin Leok, and N Harris McClamroch. Nonlinear dynamics of the 3d pendulum. *Journal of Nonlinear Science*, 21(1):3–32, 2011.
- [65] António M Lopes and JA Tenreiro Machado. Dynamics of the n-link pendulum: a fractional perspective. *International Journal of Control*, 90(6):1192–1200, 2017.
- [66] Christopher J Richards, Thomas J Smart, Philip H Jones, and David Cubero. A microscopic kapitza pendulum. *Scientific reports*, 8(1):1–10, 2018.
- [67] Richard E Berg and Todd S Marshall. Wilberforce pendulum oscillations and normal modes. *American Journal of Physics*, 59(1):32–38, 1991.
- [68] Ákos Odry, Robert Fuller, Imre J Rudas, and Péter Odry. Kalman filter for mobile-robot attitude estimation: Novel optimized and adaptive solutions. *Mechanical systems and signal processing*, 110:569–589, 2018.
- [69] Taku Komura, Akinori Nagano, Howard Leung, and Yoshihisa Shinagawa. Simulating pathological gait using the enhanced linear inverted pendulum model. *IEEE Transactions on biomedical engineering*, 52(9):1502–1513, 2005.
- [70] Jian Li and Weidong Chen. Energy-efficient gait generation for biped robot based on the passive inverted pendulum model. *Robotica*, 29(4):595–605, 2011.
- [71] Dianelys Vega Ruiz, Carlos Magluta, and Ney Roitman. Experimental verification of biomechanical model of bipedal walking to simulate vertical loads induced by humans. *Mechanical Systems and Signal Processing*, 167:108513, 2022.
- [72] Arthur D Kuo. The six determinants of gait and the inverted pendulum analogy: A dynamic walking perspective. *Human movement science*, 26(4):617–656, 2007.
- [73] Werner Schiehlen. On the historical development of human walking dynamics. In *The History of Theoretical, Material and Computational Mechanics-Mathematics Meets Mechanics and Engineering*, pages 101–116. Springer, 2014.
- [74] Jacob Larson, Edmon Perkins, Taylor Oldfather, and Michael Zabala. Local dynamic stability of the lower-limb as a means of post-hoc injury classification. *Plos one*, 16(6):e0252839, 2021.
- [75] RM Brisilla and V Sankaranarayanan. Nonlinear control of mobile inverted pendulum. *Robotics and Autonomous Systems*, 70:145–155, 2015.

- [76] Olfa Boubaker. The inverted pendulum benchmark in nonlinear control theory: a survey. *International Journal of Advanced Robotic Systems*, 10(5):233, 2013.
- [77] Rahul Kumar, Sayan Gupta, and Shaikh Faruque Ali. Energy harvesting from chaos in base excited double pendulum. *Mechanical Systems and Signal Processing*, 124:49–64, 2019.
- [78] Troy Shinbrot, Celso Grebogi, Jack Wisdom, and James A Yorke. Chaos in a double pendulum. *American Journal of Physics*, 60(6):491–499, 1992.
- [79] RB Levien and SM Tan. Double pendulum: An experiment in chaos. *American Journal of Physics*, 61(11):1038–1044, 1993.
- [80] Tomasz Stachowiak and Toshio Okada. A numerical analysis of chaos in the double pendulum. *Chaos, Solitons & Fractals*, 29(2):417–422, 2006.
- [81] Daniil Yurchenko, Panagiotis Alevras, Shengxi Zhou, Junlei Wang, Grzegorz Litak, Oleg Gaidai, and Renchuan Ye. Nonlinear vibration mitigation of a crane’s payload using pendulum absorber. *Mechanical Systems and Signal Processing*, 156:107558, 2021.
- [82] Darryl Tchokogoué, Ming Mu, Brian F Feeny, Bruce K Geist, and Steven W Shaw. The effects of gravity on the response of centrifugal pendulum vibration absorbers. *Journal of Vibration and Acoustics*, 143(6):061011, 2021.
- [83] Chengzhi Shi and Robert G Parker. Vibration modes and natural frequency veering in three-dimensional, cyclically symmetric centrifugal pendulum vibration absorber systems. *Journal of Vibration and Acoustics*, 136(1), 2014.
- [84] Ryan J Monroe and Steven W Shaw. Nonlinear transient dynamics of pendulum torsional vibration absorbers—part ii: Experimental results. *Journal of Vibration and Acoustics*, 135(1):011018, 2013.
- [85] Ryan J Monroe and Steven W Shaw. Nonlinear transient dynamics of pendulum torsional vibration absorbers—part i: theory. *Journal of Vibration and Acoustics*, 135(1), 2013.
- [86] Keiyu Kadoi, Tsuyoshi Inoue, Junichi Kawano, and Masahiko Kondo. Nonlinear analysis of a torsional vibration of a multidegrees-of-freedom system with centrifugal pendulum vibration absorbers and its suppression. *Journal of Vibration and Acoustics*, 140(6), 2018.
- [87] Michał Marszał, Błażej Witkowski, Krzysztof Jankowski, Przemysław Perlikowski, and Tomasz Kapitaniak. Energy harvesting from pendulum oscillations. *International Journal of Non-Linear Mechanics*, 94:251–256, 2017.

- [88] Changwei Liang, You Wu, and Lei Zuo. Broadband pendulum energy harvester. *Smart Materials and Structures*, 25(9):095042, 2016.
- [89] Daniil Yurchenko and Panagiotis Alevras. Parametric pendulum based wave energy converter. *Mechanical Systems and Signal Processing*, 99:504–515, 2018.
- [90] Yipeng Wu, Jinhao Qiu, Shengpeng Zhou, Hongli Ji, Yang Chen, and Sen Li. A piezoelectric spring pendulum oscillator used for multi-directional and ultra-low frequency vibration energy harvesting. *Applied energy*, 231:600–614, 2018.
- [91] Iman Izadgoshasb, Yee Yan Lim, Lihua Tang, Ricardo Vasquez Padilla, Zi Sheng Tang, and Mohammadreza Sedighi. Improving efficiency of piezoelectric based energy harvesting from human motions using double pendulum system. *Energy Conversion and Management*, 184:559–570, 2019.
- [92] J Xu and J Tang. Multi-directional energy harvesting by piezoelectric cantilever-pendulum with internal resonance. *Applied Physics Letters*, 107(21):213902, 2015.
- [93] Takehiko Asai, Yoshikazu Araki, and Kohju Ikago. Energy harvesting potential of tuned inertial mass electromagnetic transducers. *Mechanical Systems and Signal Processing*, 84:659–672, 2017.
- [94] Cevat Volkan Karadag and Nezih Topaloglu. A self-sufficient and frequency tunable piezoelectric vibration energy harvester. *Journal of Vibration and Acoustics*, 139(1), 2017.
- [95] D Hoffmann, A Willmann, T Hehn, B Folkmer, and Y Manoli. A self-adaptive energy harvesting system. *Smart Materials and Structures*, 25(3):035013, 2016.
- [96] Tamir Perl, Ronen Maimon, Slava Krylov, and Nahum Shimkin. Control of vibratory mems gyroscope with the drive mode excited through parametric resonance. *Journal of Vibration and Acoustics*, 143(5):051013, 2021.
- [97] Martial Defoort, Parsa Taheri-Tehrani, Sarah H Nitzan, and David A Horsley. Impact of synchronization in micromechanical gyroscopes. *Journal of Vibration and Acoustics*, 139(4), 2017.
- [98] Solomon Davis, Shachar Tresser, Netanel Ariel, Alex Ferdinkoif, and Izhak Bucher. In situ identification of natural frequency branches in gyroscopic systems via autoresonance and phase-locked loop. *Journal of Vibration and Acoustics*, 142(1), 2020.
- [99] Chunbo Lan, Zhenning Chen, Guobiao Hu, Yabin Liao, and Weiyang Qin. Achieve frequency-self-tracking energy harvesting using a passively adaptive cantilever beam. *Mechanical Systems and Signal Processing*, 156:107672, 2021.

- [100] XiaoFu Li, Md Raf E Ul Shougat, Scott Kennedy, Casey Fendley, Robert N Dean, Aubrey N Beal, and Edmon Perkins. A four-state adaptive hopf oscillator. *Plos one*, 16(3):e0249131, 2021.
- [101] XiaoFu Li, Md Raf E Ul Shougat, Tushar Mollik, Aubrey N Beal, Robert N Dean, and Edmon Perkins. Stochastic effects on a hopf adaptive frequency oscillator. *Journal of Applied Physics*, 129(22):224901, 2021.
- [102] Ned J Corron. Complex waveform estimation using adaptive frequency oscillators. *Chaos, Solitons & Fractals*, 158:111991, 2022.
- [103] Ludovic Righetti, Jonas Buchli, and Auke Jan Ijspeert. Adaptive frequency oscillators and applications. *The Open Cybernetics & Systemics Journal*, 3(1), 2009.
- [104] VV Makarov, AA Koronovskii, VA Maksimenko, AE Hramov, OI Moskalenko, Javier Martin Buldu, and S Boccaletti. Emergence of a multilayer structure in adaptive networks of phase oscillators. *Chaos, Solitons & Fractals*, 84:23–30, 2016.
- [105] Christian Bick, Mark J Panaggio, and Erik A Martens. Chaos in kuramoto oscillator networks. *Chaos: An Interdisciplinary Journal of Nonlinear Science*, 28(7):071102, 2018.
- [106] CC Olson, JM Nichols, JV Michalowicz, and F Bucholtz. Signal design using nonlinear oscillators and evolutionary algorithms: Application to phase-locked loop disruption. *Chaos: An Interdisciplinary Journal of Nonlinear Science*, 21(2):023136, 2011.
- [107] Tanmoy Banerjee, Bishwajit Paul, and BC Sarkar. Spatiotemporal dynamics of a digital phase-locked loop based coupled map lattice system. *Chaos: An Interdisciplinary Journal of Nonlinear Science*, 24(1):013116, 2014.
- [108] Bishwajit Paul and Tanmoy Banerjee. Chimeras in digital phase-locked loops. *Chaos: An Interdisciplinary Journal of Nonlinear Science*, 29(1):013102, 2019.
- [109] S Chakraborty, M Dandapathak, and BC Sarkar. Oscillation quenching in third order phase locked loop coupled by mean field diffusive coupling. *Chaos: An Interdisciplinary Journal of Nonlinear Science*, 26(11):113106, 2016.
- [110] Yi-Bo Zhao, Du-Qu Wei, and Xiao-Shu Luo. Study on chaos control of second-order non-autonomous phase-locked loop based on state observer. *Chaos, Solitons & Fractals*, 39(4):1817–1822, 2009.
- [111] Bassam A Harb and Ahmad M Harb. Chaos and bifurcation in a third-order phase locked loop. *Chaos, Solitons & Fractals*, 19(3):667–672, 2004.
- [112] D d’Humieres, MR Beasley, BA Huberman, and A Libchaber. Chaotic states and routes to chaos in the forced pendulum. *Physical Review A*, 26(6):3483, 1982.

- [113] Xu Xu, Marian Wiercigroch, and MP Cartmell. Rotating orbits of a parametrically-excited pendulum. *Chaos, Solitons & Fractals*, 23(5):1537–1548, 2005.
- [114] SR Bishop, A Sofroniou, and P Shi. Symmetry-breaking in the response of the parametrically excited pendulum model. *Chaos, Solitons & Fractals*, 25(2):257–264, 2005.
- [115] Sang-Yoon Kim and Bambi Hu. Bifurcations and transitions to chaos in an inverted pendulum. *Physical Review E*, 58(3):3028, 1998.
- [116] HN Nunez-Yepe, AL Salas-Brito, CA Vargas, and L Vicente. Onset of chaos in an extensible pendulum. *Physics Letters A*, 145(2-3):101–105, 1990.
- [117] Aline Souza de Paula, Marcelo Amorim Savi, and Francisco Heitor Iunes Pereira-Pinto. Chaos and transient chaos in an experimental nonlinear pendulum. *Journal of sound and vibration*, 294(3):585–595, 2006.
- [118] Congcong Miao, Wu Luo, Yaqi Ma, Weiqing Liu, and Jinghua Xiao. A simple method to improve a torsion pendulum for studying chaos. *European Journal of Physics*, 35(5):055012, 2014.
- [119] Vyacheslav O Munyaev, Dmitry S Khorkin, Maxim I Bolotov, Lev A Smirnov, and Grigory V Osipov. Appearance of chaos and hyperchaos in evolving pendulum network. *Chaos: An Interdisciplinary Journal of Nonlinear Science*, 31(6):063106, 2021.
- [120] Francisco Heitor I Pereira-Pinto, Armando M Ferreira, and Marcelo A Savi. Chaos control in a nonlinear pendulum using a semi-continuous method. *Chaos, Solitons & Fractals*, 22(3):653–668, 2004.
- [121] Ruiqi Wang and Zhujun Jing. Chaos control of chaotic pendulum system. *Chaos, Solitons & Fractals*, 21(1):201–207, 2004.
- [122] Harry F Olson and Herbert Belar. Electronic music synthesizer. *The journal of the Acoustical Society of America*, 27(3):595–612, 1955.
- [123] Leon S Theremin and Oleg Petrishev. The design of a musical instrument based on cathode relays. *Leonardo Music Journal*, 6(1):49–50, 1996.
- [124] Xavier Rodet. Sound and music from chua’s circuit. In *Chua’s Circuit: A Paradigm For Chaos*, pages 434–446. World Scientific, 1993.
- [125] Victor Lazzarini and Joseph Timoney. New perspectives on distortion synthesis for virtual analog oscillators. *Computer Music Journal*, 34(1):28–40, 2010.
- [126] Julius O Smith. Physical modeling synthesis update. *Computer Music Journal*, 20(2):44–56, 1996.

- [127] Qubais Reed Ghazala. The folk music of chance electronics: Circuit-bending the modern coconut. *Leonardo Music Journal*, 14:97–104, 2004.
- [128] Joseph A Paradiso and Neil Gershenfeld. Musical applications of electric field sensing. *Computer music journal*, 21(2):69–89, 1997.
- [129] David T Yeh, Jonathan S Abel, Andrei Vladimirescu, and Julius O Smith. Numerical methods for simulation of guitar distortion circuits. *Computer Music Journal*, 32(2):23–42, 2008.
- [130] Jyri Pakarinen and David T Yeh. A review of digital techniques for modeling vacuum-tube guitar amplifiers. *Computer Music Journal*, 33(2):85–100, 2009.
- [131] Katsuyoshi Tsujita, Kazuo Tsuchiya, and Ahmet Onat. Adaptive gait pattern control of a quadruped locomotion robot. In *Proceedings 2001 IEEE/RSJ International Conference on Intelligent Robots and Systems. Expanding the Societal Role of Robotics in the the Next Millennium (Cat. No. 01CH37180)*, volume 4, pages 2318–2325. IEEE, 2001.
- [132] Matija Marolt. Adaptive oscillator networks for partial tracking and piano music transcription. In *ICMC*, 2000.
- [133] Matija Marolt. Networks of adaptive oscillators for partial tracking and transcription of music recordings. *Journal of New Music Research*, 33(1):49–59, 2004.
- [134] Matija Marolt. A connectionist approach to automatic transcription of polyphonic piano music. *IEEE Transactions on Multimedia*, 6(3):439–449, 2004.
- [135] Fabien Gouyon and Simon Dixon. A review of automatic rhythm description systems. *Computer music journal*, 29(1):34–54, 2005.
- [136] XiaoFu Li, Pawan Kallepalli, Tushar Mollik, Md. Raf E Ul Shougat, Scott Kennedy, Sean Frabitore, and Edmon Perkins. The pendulum adaptive frequency oscillator. *Mechanical Systems and Signal Processing*, submitted.
- [137] XiaoFu Li, Aubrey N. Beal, Robert N. Dean, and Edmon Perkins. Chaos in a pendulum adaptive frequency oscillator. *Chaos, Solitons, and Fractals*, submitted.
- [138] Alex Tucker and Edmon Perkins. Asphaltophones: Modeling, analysis, and experiment. *The Journal of the Acoustical Society of America*, 148(1):236–242, 2020.
- [139] XiaoFu Li and Edmon Perkins. A hopf adaptive oscillator analog circuit as a musical instrument. *Computer Music Journal*, submitted.
- [140] Ali H Nayfeh and Balakumar Balachandran. *Applied nonlinear dynamics: analytical, computational, and experimental methods*. John Wiley & Sons, 2008.

- [141] Edmon Perkins and Tim Fitzgerald. Continuation method on cumulant neglect equations. *Journal of Computational and Nonlinear Dynamics*, 13(9), 2018.
- [142] Chunni Wang, Jun Tang, and Jun Ma. Minireview on signal exchange between nonlinear circuits and neurons via field coupling. *The European Physical Journal Special Topics*, 228(10):1907–1924, 2019.
- [143] Li Xiong, Yan-Jun Lu, Yong-Fang Zhang, Xin-Guo Zhang, and Parag Gupta. Design and hardware implementation of a new chaotic secure communication technique. *PloS one*, 11(8):e0158348, 2016.
- [144] Mickaël Lallart, Steven R Anton, and Daniel J Inman. Frequency self-tuning scheme for broadband vibration energy harvesting. *Journal of Intelligent Material Systems and Structures*, 21(9):897–906, 2010.
- [145] Alejandro Silva-Juárez, Esteban Tlelo-Cuautle, Luis Gerardo de la Fraga, and Rui Li. Fpaa-based implementation of fractional-order chaotic oscillators using first-order active filter blocks. *Journal of advanced research*, 2020.
- [146] Desmond J Higham. An algorithmic introduction to numerical simulation of stochastic differential equations. *SIAM review*, 43(3):525–546, 2001.
- [147] Leslaw Socha. *Linearization methods for stochastic dynamic systems*, volume 730. Springer Science & Business Media, 2007.
- [148] Alexandre J Chorin and Ole H Hald. Brownian motion. In *Stochastic Tools in Mathematics and Science*, pages 47–81. Springer, 2009.
- [149] William Coffey and Yu P Kalmykov. *The Langevin equation: with applications to stochastic problems in physics, chemistry and electrical engineering*, volume 27. World Scientific, 2012.
- [150] Rouslan L Stratonovich. *Topics in the theory of random noise*, volume 2. CRC Press, 1967.
- [151] Crispin W Gardiner et al. *Handbook of stochastic methods*, volume 3. springer Berlin, 1985.
- [152] Hannes Risken. Fokker-planck equation. In *The Fokker-Planck Equation*, pages 63–95. Springer, 1996.
- [153] Wen-An Jiang and Li-Qun Chen. Stochastic averaging of energy harvesting systems. *International Journal of Non-Linear Mechanics*, 85:174–187, 2016.
- [154] JB Roberts and PD Spanos. Stochastic averaging: an approximate method of solving random vibration problems. *International Journal of Non-Linear Mechanics*, 21(2):111–134, 1986.

- [155] BF Spencer and LA Bergman. On the numerical solution of the fokker-planck equation for nonlinear stochastic systems. *Nonlinear Dynamics*, 4(4):357–372, 1993.
- [156] Pankaj Kumar, S Narayanan, and Sayan Gupta. Finite element solution of fokker-planck equation of nonlinear oscillators subjected to colored non-gaussian noise. *Probabilistic Engineering Mechanics*, 38:143–155, 2014.
- [157] Mohammed F Daqaq. On intentional introduction of stiffness nonlinearities for energy harvesting under white gaussian excitations. *Nonlinear Dynamics*, 69(3):1063–1079, 2012.
- [158] Edmon Perkins and Balakumar Balachandran. Effects of phase lag on the information rate of a bistable duffing oscillator. *Physics Letters A*, 379(4):308–313, 2015.
- [159] SF Wojtkiewicz, BF Spencer Jr, and LA Bergman. On the cumulant-neglect closure method in stochastic dynamics. *International journal of non-linear mechanics*, 31(5):657–684, 1996.
- [160] Christian Kuehn. Moment closure—a brief review. *Control of self-organizing nonlinear systems*, pages 253–271, 2016.
- [161] Xu Xu and Marian Wiercigroch. Approximate analytical solutions for oscillatory and rotational motion of a parametric pendulum. *Nonlinear Dynamics*, 47(1):311–320, 2007.
- [162] Rodrigo Augusto Ricco, Anny Verly, and Gleison Fransoares Vasconcelos Amaral. A circuit for automatic measurement of bifurcation diagram in nonlinear electronic oscillators. *IEEE Latin America Transactions*, 14(7):3042–3047, 2016.
- [163] Debabrata Biswas and Tanmoy Banerjee. A simple chaotic and hyperchaotic time-delay system: design and electronic circuit implementation. *Nonlinear Dynamics*, 83(4):2331–2347, 2016.
- [164] Emilson R Viana Jr, Rero M Rubinger, Holokx A Albuquerque, Alfredo G de Oliveira, and Geraldo M Ribeiro. High-resolution parameter space of an experimental chaotic circuit. *Chaos: An Interdisciplinary Journal of Nonlinear Science*, 20(2):023110, 2010.
- [165] Hadi Jahanshahi, Onofre Orozco-López, Jesus M Munoz-Pacheco, Naif D Alotaibi, Christos Volos, Zhen Wang, R Sevilla-Escoboza, and Yu-Ming Chu. Simulation and experimental validation of a non-equilibrium chaotic system. *Chaos, Solitons & Fractals*, 143:110539, 2021.
- [166] Tien-Yien Li and James A Yorke. Period three implies chaos. In *The theory of chaotic attractors*, pages 77–84. Springer, 2004.

- [167] Viet-Thanh Pham, Sajad Jafari, Christos Volos, and Luigi Fortuna. Simulation and experimental implementation of a line–equilibrium system without linear term. *Chaos, Solitons & Fractals*, 120:213–221, 2019.
- [168] GD Leutcho, J Kengne, and L Kamdjeu Kengne. Dynamical analysis of a novel autonomous 4-d hyperjerk circuit with hyperbolic sine nonlinearity: chaos, antimonicity and a plethora of coexisting attractors. *Chaos, Solitons & Fractals*, 107:67–87, 2018.
- [169] Adel Ouannas, Zaid Odibat, and Tasawar Hayat. Fractional analysis of co-existence of some types of chaos synchronization. *Chaos, Solitons & Fractals*, 105:215–223, 2017.
- [170] Christian Nwachiona and J Humberto Pérez-Cruz. Analysis of a new chaotic system, electronic realization and use in navigation of differential drive mobile robot. *Chaos, Solitons & Fractals*, 144:110684, 2021.
- [171] Gervais Dolvis Leutcho and Jacques Kengne. A unique chaotic snap system with a smoothly adjustable symmetry and nonlinearity: Chaos, offset-boosting, antimonicity, and coexisting multiple attractors. *Chaos, Solitons & Fractals*, 113:275–293, 2018.
- [172] Haydar Kutuk and Sung-Mo Kang. A field-programmable analog array (fpaa) using switched-capacitor techniques. In *1996 IEEE International Symposium on Circuits and Systems. Circuits and Systems Connecting the World. ISCAS 96*, volume 4, pages 41–44. IEEE, 1996.
- [173] Recai Kilic and Fatma Yildirim Dalkiran. Reconfigurable implementations of chua's circuit. *International Journal of Bifurcation and Chaos*, 19(04):1339–1350, 2009.
- [174] Esteban Tlelo-Cuautle, Ana Dalia Pano-Azucena, Omar Guillén-Fernández, and Alejandro Silva-Juárez. *Analog/digital implementation of fractional order chaotic circuits and applications*. Springer, 2020.
- [175] Enis Günay and Kenan Altun. Lorenz-like system design using cellular neural networks. *Turkish Journal of Electrical Engineering & Computer Sciences*, 26(4):1812–1819, 2018.
- [176] Chunbiao Li, Wesley Joo-Chen Thio, Julien Clinton Sprott, Herbert Ho-Ching Iu, and Yujie Xu. Constructing infinitely many attractors in a programmable chaotic circuit. *IEEE Access*, 6:29003–29012, 2018.
- [177] Serdar Çiçek. Fpaa based design and implementation of sprott n chaotic system. In *International Scientific and Vocational Studies Congress*, pages 476–482. BILMES 2019 Ankara, 2019.

- [178] Hamsa A Abdullah and Hikmat N Abdullah. Design and fpa implementation of novel chaotic system. *Univ Politehnica Bucharest Scient Bull Ser C-Electrical Eng Comput Sci*, 81(2):153–164, 2019.
- [179] Fatma Yildirim Dalkiran and Julien Clinton Sprott. Simple chaotic hyperjerk system. *International Journal of Bifurcation and Chaos*, 26(11):1650189, 2016.
- [180] Nimet Dahasert, İsmail Öztürk, and Recai Kiliç. Experimental realizations of the hr neuron model with programmable hardware and synchronization applications. *Nonlinear Dynamics*, 70(4):2343–2358, 2012.
- [181] Melnik Dmitry. Vocal remover and isolation. <https://vocalremover.org/>, accessed: 04.19.2021.
- [182] Franz Schubert. Ellens dritter gesang. *D. 839, Op. 52, No. 6*, 1825.
- [183] Bradley Chapman. Ave maria, d. 839. <https://musopen.org/music/1673-ave-maria-d-839>, accessed: 04.19.2021.